

האוניברסיטה העברית בירושלים
הפקולטה למתמטיקה ולמדעי הטבע
המכון למדעי כדור הארץ
החוג לגיאולוגיה

A Semi-Automated Tool for Generating Satellite Derived Bathymetry in The Shallow Sea

**כלי אוטומטי למחצה לאומדן בתימטריה באמצעות הדמאות
לוויין בים הרדוד**

עבודת גמר לתואר מוסמך במדעי הטבע

מוגשת על ידי:

Shahar Levenson

שחר לוינסון

בהדרכת:

פרופסור אמוץ עגנון

18/12/2019

כ' כסלו התש"פ

A Personal Note

This had been a long journey.

The research started as a side project initiated by Dr. John Hall. He had the vision to understand that using remote sensing for the rapid mapping of the shallow ocean floor is a promising tool. He encouraged and supported me and without his enthusiasm this study would had never existed.

I owe a great deal to my supervisor, Prof. Amotz Agnon, a fountain of knowledge and ideas. His teaching went beyond the academic as from him I learned about remaining calm, being humble, taking the time to brew the best coffee and always aiming to be the MVP.

I would like to thank Profs. Hezi Gildor and Adi Torfstein, the members of my advisory committee, for the time they have invested and their understanding of my schedule constraints.

Finally, and most importantly, I thank my loving wife, Dr. Yael Levenson. She is the sole reason for me completing this study. Her patience, her drive, her believing in me when I was certain that I will not be able to finish in time made the difference between a master's degree and a "what could have been". Working two jobs and still finding the time and strength for taking care of our three wonderful children, so that I had the free time to concentrate on this work is nothing less than admirable. I am forever in her debt.

תקציר

על אף החשיבות הרבה שיש לאוקיינוסים של כדור הארץ בתחומי הכלכלה, התיירות והמחקר, הם ברובם אינם ממופים. ההערכות הן שכ-9% מהים בלבד ממופה בעזרת כלים מהימנים ואילו 71% מקרקעית הים רדוד – עד 200 מטר עומק – אינם ממופים כלל. אומנם יש בידינו נתונים אודות המבנה הכללי של קרקעית הים בכיסוי גלובאלי, אולם הנתונים הללו מגיעים מלווייני אלטימטריה שמוגבלים למיפוי אופקי בקנה מידה מירבי של 1 ק"מ. בעוד שקנה מידה זה מספיק לצורך מיפוי מבנים גדולים כגון רכסים מרכז אוקייניים, אין הדבר מספק לתחומי ידע כגון גיאומורפולוגיה וביולוגיה. הכלים המאפשרים מיפוי מדויק יותר, כלים המתבססים על אמצעים אקוסטיים בסירות מחקר, יקרים ודורשים השקעת זמן מרובה.

בשנים האחרונות חלה התקדמות רבה בתחום המיפוי הממוחשב. תמונות לוויין שזמינות לציבור הרחב בשילוב יכולות מחשוב מתקדמות הביאו לעלייה בשימוש הדמאות לוויין למיפוי, בכלל זה מיפוי קרקעית הים. יחד עם זאת, הכלים למיפוי ימי נותרו ברובם כלים ידניים הדורשים השקעת זמן מרובה ולא מאפשרים מיפוי של שטחים נרחבים.

בעבודה זו התמקדתי באחת משיטות המיפוי של קרקעית הים הרדוד – עד עומק של כ-30 מטר. שיטה זו מסתמכת על ההבדלים בין היכולת של אורכי גל שונים לחדור את המים. מאחר והאור באורך הגל הכחול (450-515 nm) נבלע פחות יחסית לאור באורך הגל הירוק (525-600 nm) בהתאם למרחק שאותו האור עובר במים, ניתן למצוא פונקציה הקושרת בין עומק המים לבין היחס של האור המוחזר מהקרקעית בשני אורכי גל אלו. הקשר בין יחס אורכי הגל והעומק מתקיים כל עוד המים צלולים וללא מערבוליות וכן כל עוד העומק איננו עולה על עומק ההכחד שממנו ואילך האור לא מחוזר מהקרקעית אלא מגוף המים. השיטה מצריכה נתונים אודות כמות האור המוחזר באורכי הגל השונים וכן נתוני עומק מדודים (נתוני אמת) כדי לכייל ולבדוק את התוצאות. השתמשתי בהדמאות של הלוויין Landsat 8 הזמינות לציבור הרחב כמקור לנתוני האור ובשני מקורות עבור נתוני העומק המדודים: נתונים שנאספו במכון הבין-אוניברסיטאי באילת בעזרת שיטות אקוסטיות וכן בנתונים שיצר ד"ר ג'ון הול מתוך דיגיטציה של מפות ימיות ממגוון מקורות.

המחקר התחלק לשני שלבים עיקריים. בשלב הראשון כתבתי קוד מחשב המבוסס על שפת פייתון שעבור כל אזור מחקר מוריד את הדמאות הלוויין באורכי הגל הרלבנטיים מהשרתים של אמזון, מריץ סדרה של עיבודי תמונה על כל הדמאה, מפריד בין ים ליבשה, מחשב את יחס אורכי הגל ומכייל את התוצאות מול נתוני העומק המדודים. בכך יצרתי כלי אוטומטי שמקצר משמעותית את הזמן הנדרש ליצירת בתימטריה בים הרדוד. במקביל שיפרתי את הדיוק של השלבים השונים, למשל על ידי הפרדה בין ים ליבשה על בסיס כלים סטטיסטיים כתחליף להחלטה ויזואלית או בחירה אוטומטית

מתוך חישובי מרווח טעות של ההדמאה הטובה ביותר לאזור המחקר במקום בחירה ויזואלית של הדמאה ספציפית.

השלב השני של המחקר כלל חלק שבו השתמשתי בקוד המחשב ליצירת בתימטריה בארבעה אזורי מחקר שונים – מפרץ אילת, ארכיפלג דחלק שלייד אריתריאה, מיצרי באב אל-מנדב בפתח הים האדום והים שבין בחריין וצפון קטאר.

השלב השני כלל חלק נוסף שבו פיתחתי שיטה חדשה לכיול הבתימטריה באזורים שבהם אין לנו כלל נתוני עומק מדודים. לשם כך הסתמכתי על ההבדלים בין הגאות והשפל הנוגעים למיקום קו החוף ולהפרשי הגובה כדי לייצר נתונים לכיול. השתמשתי בשיטה זו ליצירת בתימטריה רדודה בשני אזורי מחקר שבהם הפרשים גדולים בין הגאות והשפל: מפרץ פונדי שבמזרח קנדה והחוף שלייד העיר ברומי במערב אוסטרליה.

Table of Contents

A Personal Note	i
תקציר	iii
Table of Contents	v
Background	1
Research Objectives	3
Methods	7
The SDB Algorithm	7
Satellites Images used in the Study	8
Tools used in the study	10
Sources for depth data.....	11
Calibration techniques	11
The Traditional Method: Calibrating against measured data	11
Novel: Tides.....	13
The Work Process	16
Image Acquisition	16
Land-water separation	16
Image processing	19
Applying the SDB algorithm.....	20
Sampling.....	20
Calibrating	21
Saving the results	22
Results and Discussion	23
Stage 1: Automating the work process	23
Stage 2, part A: Generating SDB layers	25
The Gulf of Eilat.....	26
The Dahlak Archipelago	35
Bab el-Mandab	43
Qatar.....	51
Stage 2, part B: Calibrating by Tidal Data	59
The Bay of Fundy, Canada.....	59

Broome, Australia	69
Testing Different Fitting Methods	77
Future Studies.....	79
Summary.....	80
Bibliography	81

Background

Despite the fundamental role that the oceans of Earth play in marine life, climate control, commerce and so forth, they remain poorly mapped. Although large-scale mapping tools, mainly satellite altimetry, are being used to generate global bathymetry, they have limited spatial resolution on the order of 1 km at best and therefore cannot identify smaller structures and features. The finer detailed bathymetry, which is vital, for example, to the study of active faults, glacial landforms and benthic habitats is very lacking. It is estimated that less than 18% of the oceans floor had been measured with small-scale tools such as echo sounding and Lidar, while about half of that area was mapped by extrapolation based on few measurements points, questioning its reliability (Mayer et al., 2018).

This situation describes both the deep and the shallow areas of the large bodies of water of Earth, each with its unique challenges for mapping and measuring their depths. The estimations for the current state of ocean floor mapping puts the areas shallower than 200 m depth at 71% uncharted and the deeper areas at 66-85% uncharted. Of these two areas, the shallows present the heavier investment in terms of survey effort required due to the limitations of the sounding tools near the shore (Mayer et al., 2018).

The improvement in computational power in recent years combined with a rise in the availability of publicly open satellite imagery facilitate the implementation of various research tools such as Satellite Derived Bathymetry (SDB). This tool offers the possibility of generating shallow-water bathymetry with lower costs and risks as compared to classical, direct measurement methods (Pe'eri et al., 2014).

Additionally, SDB has the potential of generating navigation quality charts as its accuracy can reach the standards of the IHO (IHO, 2014; Pe'eri et al., 2014; Chénier et al., 2018).

Relying mainly on optic remote sensing technology, SDB is limited to the photic zone, i.e., maximum depths of 200 m, which roughly represents 7% of Earth's oceans area. (Mayer et al., 2018). This depth is considered a theoretical maximum, while in practice the depths are typically limited to optically shallow waters, approximatively one Secchi depth (Jegat et al., 2016). This suggests an average maximum of about 30 m depth (Pe'eri et al., 2014; Chénier et al., 2018; Kabiri, 2017;

Caballero & Stumpf, 2019) in non-turbid, oligotrophic waters, representing roughly 2% of Earth’s oceans area (Fig. 1). In practice this percentage will be lower since large areas of the oceans tend towards the eutrophic state (Morel et al., 2010), thus limiting the potential penetration of light. Nevertheless, the shallows represent a highly dynamic environment (Chénier et al., 2018) whose research can benefit from satellite monitoring methods.

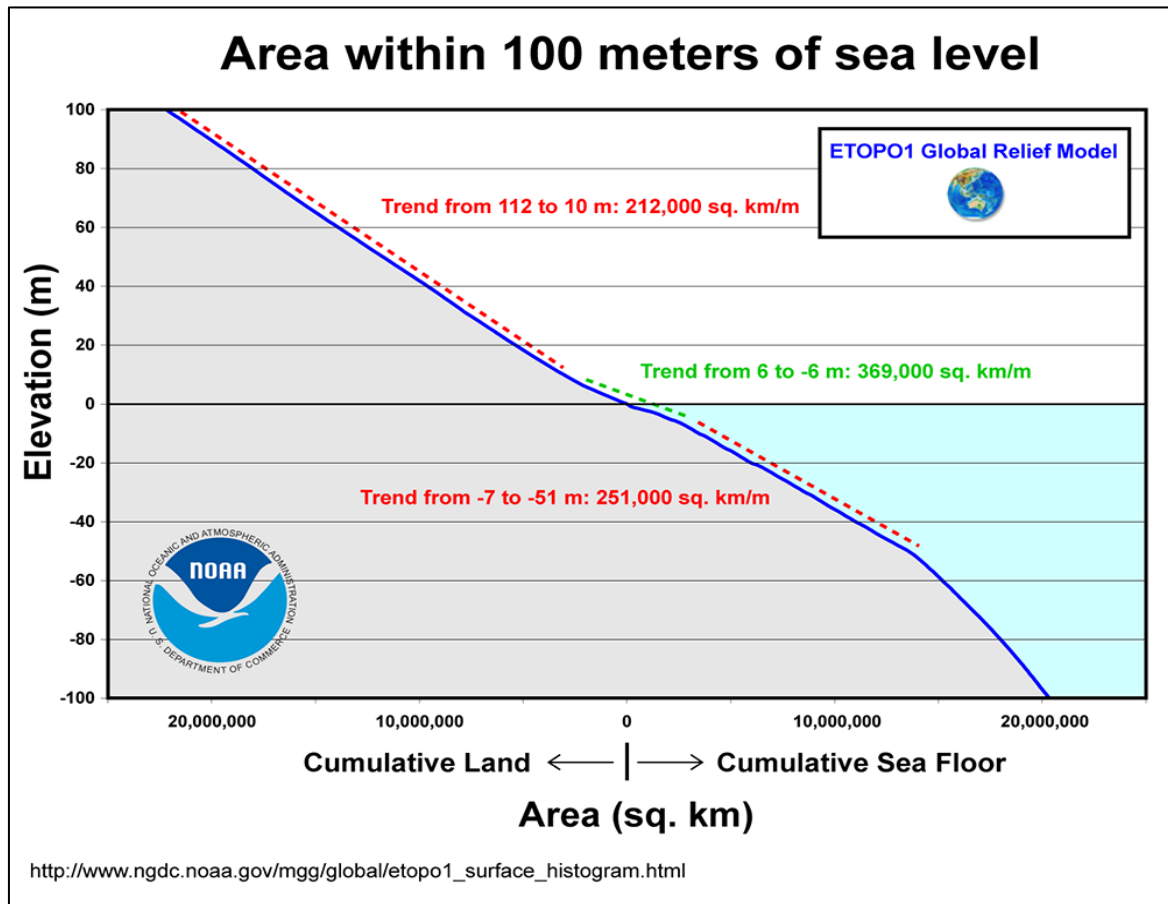


Figure 1 : A general model of the shallow areas of Earth oceans. The depths reaching 30 m occupy about 8,000,000 km², being roughly 2% of the surface area of the oceans – about 360,000,000 km² (Mayer et al., 2018; Eakings & Sharman, 2012)

The SDB method which I set to improve within this study is mainly a slow, manual process that relies on in-situ measurements for calibration. I automated the process in a script-based way while also exploring a new calibration technique derived from near-shore tidal amplitudes. This automated process may facilitate the generation of SDB for the purposes of area monitoring and future survey planning.

Research Objectives

While Satellite Derived Bathymetry (SDB) has been implemented in several studies and over several areas in recent years (Caballero & Stumpf, 2019), it remains mainly a slow and manual process (IHO-IOC GEBCO Cook Book, 2015), not suitable for large scale mapping. In this study I improved the SDB method by turning it into an automatic tool and used it to generate a bathymetry layer (a geographic dataset used in GIS software) for the shallows in the various research areas. These bathymetry layers were calibrated, i.e., transformed into meaningful depth data, using two different methods: by using direct, in-situ measurements of depth or by using estimations that are derived from tidal amplitudes and difference in the location of the shorelines.

This study was divided into two stages:

Stage 1:

Automating the SDB process by scripting the existing manual work process. I found alternative solutions to parts of the process which could not be directly automated, such as visually detecting a threshold value to distinguish between land and water, as well as choosing the best satellite scene by applying error estimations during the process and not relying on visually pre-selecting the best scene.

Stage 2:

Part A: The automated process was used for generating a bathymetry layer for four study areas in the Red Sea & the Persian Gulf (Fig. 2) for which I had reliable in-situ depth measurements. These bathymetry layers were generated while testing several calibration methods.



Figure2 : The study areas used in part A of Stage 2 for testing several SDB calibration methods.

Part B: I introduced a novel, tidal-based method for calibrating SDB without relying on in-situ data. This method was tested in the Bay of Fundy in Canada and near Broome, Australia (Fig. 3) – areas which offer a large differential tidal amplitude.

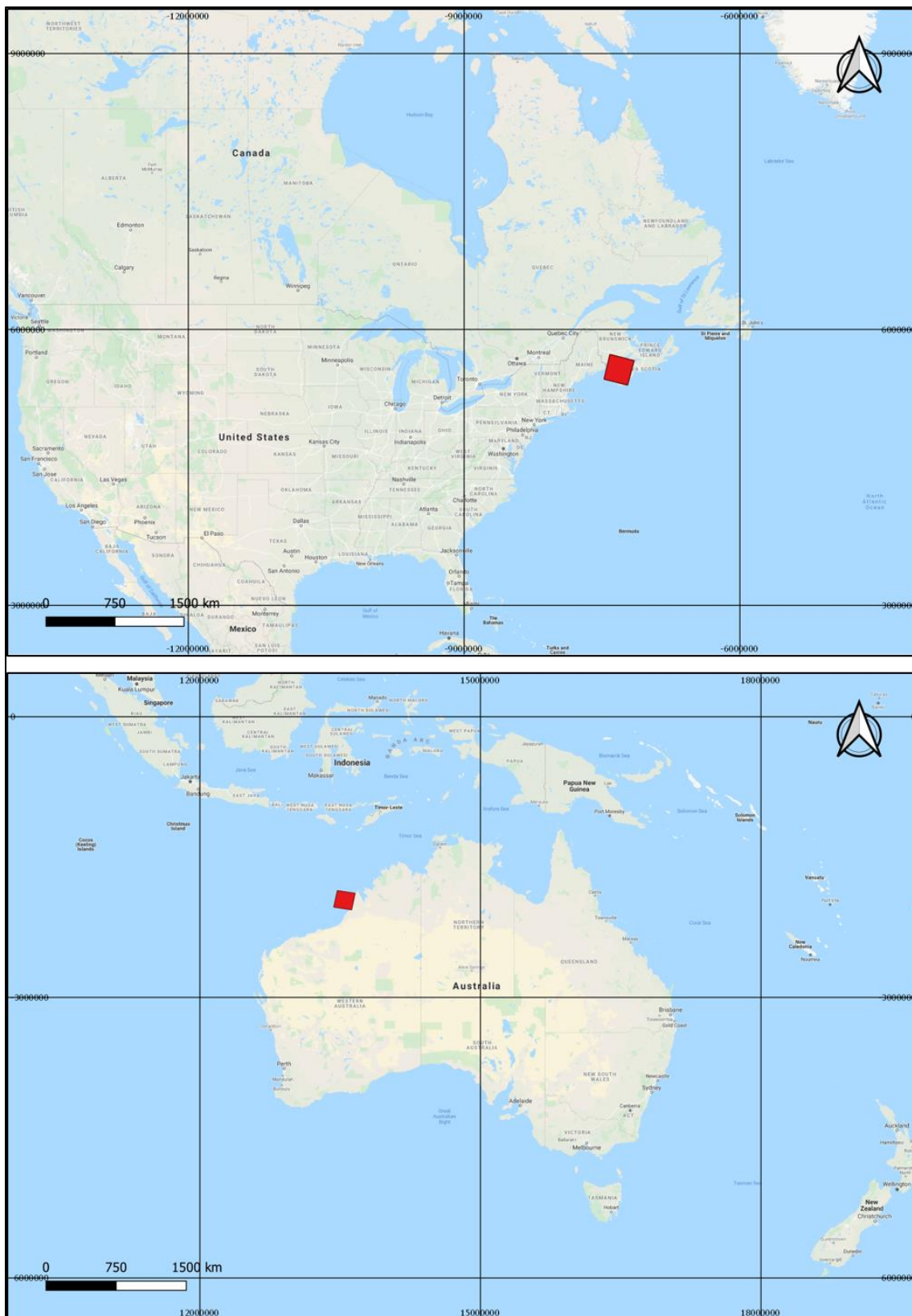


Figure3 : The study areas (mark as a red rectangle) used in part B of Stage 2 for testing a novel tidal-based calibration method: The Bay of Fundy (above) and Broome, Australia (below).

Methods

The SDB Algorithm

The radiance observed by a remote detector over any shallow-water location can be generally described with a simple model (Lyzenga, 1978; Philpot, 1989):

$$(1) L_{obs} = L_b e^{-kz} + L_w$$

Where L_{obs} is the observed reflectance, z is the depth, L_w is the reflectance over deep water ($z \rightarrow \infty$), k is an attenuation coefficient and L_b is the radiance term which is sensitive to bottom reflectance. The last two variables represent the effect of several environmental conditions, such as atmospheric transmittance, solar irradiance and bottom albedo.

The correlation between the depth and the observed reflectance can be calculated using two SDB approaches: The physical approach and the empirical approach. In the physical approach the different environmental conditions are measured or estimated and are used as parameters in a series of equations that correlate the depth to the observed reflectance (Dekker et al., 2011). In the empirical approach, which was used in this study, the observed reflectance is calibrated with depth measurements from the study area. To minimize the effects of the environmental conditions, a log-ratio model was used. This model assumes that in a uniformly mixed water column the ratio of two bands will have a near-constant attenuation value since both bands will be affected by the same environmental factors (Stumpf et al., 2003; Pe'eri et al., 2014), thus the log-ratio (R) of the light observed within the two bands (λ_i, λ_j) is proportional to the depth:

$$(2) R = \frac{\ln(L_{obs}(\lambda_i))}{\ln(L_{obs}(\lambda_j))}$$

$$(3) z = f(R)$$

The model shows a linear relationship (the function f) between in-situ depth measurements and the log-ratio. Both of the linear parameters – the gain (m_1) and the offset (m_0) – can be empirically determined by (Pe’eri et al., 2014):

$$(4) z = m_1 R + m_0$$

This linear relationship occurs only in optically clear shallow water. In deeper water the observed radiance originates from light scattering within the water column with a minimal-to-non-existing contribution from the bottom reflectance. Thus, a depth of extinction should be determined which will represent the maximum valid depth observable within the model for each specific sensor scene.

In this research I used the log-ratio between the blue (450-510 nm) and green wavelengths (530-590 nm) as suggested by Stumpf et al. (2003) for the minimization of the environmental effects (Pe’eri et al., 2014).

Satellites Images used in the Study

The input imagery used as a source for the SDB was the Blue, Green and Shortwave-Infrared (SWIR) bands from the OLI sensor in the USGS Landsat 8 platform (bands 2,3 and 6, respectively – see Table 1). Each of these bands has a spatial resolution of 30m and is referenced to the Universal Transverse Mercator projection using the WGS84 datum.

Band	Spectral Range [μm]	Spatial Resolution
2 – Blue	0.452-0.512	30 m
3 – Green	0.533-0.590	30 m
6 – Shortwave Infrared (SWIR)	1.566-1.651	30 m

Table1 : Spectral bands used in this study

The Landsat 8 mission follows the coordinate system of the World Reference System 2 (WRS-2) that divides the globes into a sequence of paths and rows so that every image is assigned to a path/row couple, with some overlapping areas. The satellite revisits each path/row every 16 days, adding to an increasing archive of images. This large, publicly available, archive of Landsat 8 images enabled me to

focus on scenes with higher quality by using exclusively the Tier-1 data products. This data tier ensures a maximum of 3% in absolute radiometric uncertainty, an average of 0.09% in temporal uncertainty and an absolute geodetic accuracy better than 12m circular error at 90% confidence (USGS, 2019). Moreover, in each study area I selected only the images with less than 0.1% cloud coverage in order to minimize the need for cloud correction steps in the process. While this reduced the number of available scenes for each study area by 90-95%, the large Landsat 8 archive offered nonetheless a seemingly sufficient number of images.

The pixel values in the Landsat 8 bands used in this study represent the amount of light reaching the sensor (Top-of-Atmosphere, or ToA, reflectance). In order to reduce the bandwidth and amount of storage required for saving this data, the ToA reflectance in the Landsat 8 mission is converted and saved in the final product as integers of dimensionless, 16-bit digital numbers (DN), with a range between 0 and 65,536. These DN have a linear correlation to the ToA reflectance, by which pixels of higher values represent areas that reflect more light back at the sensor compared to areas with low pixel values (Fig. 4).

Each Landsat 8 image is contained within a rectangle with dimensions of 7581 pixels wide by 7731 pixels high, representing an area of 227 X 232 km. The actual data that is acquired by the sensor has an area of 190 X 180 km. The containing rectangle has a constant pixel value of 0 DN that should be taken into consideration in the image processing.

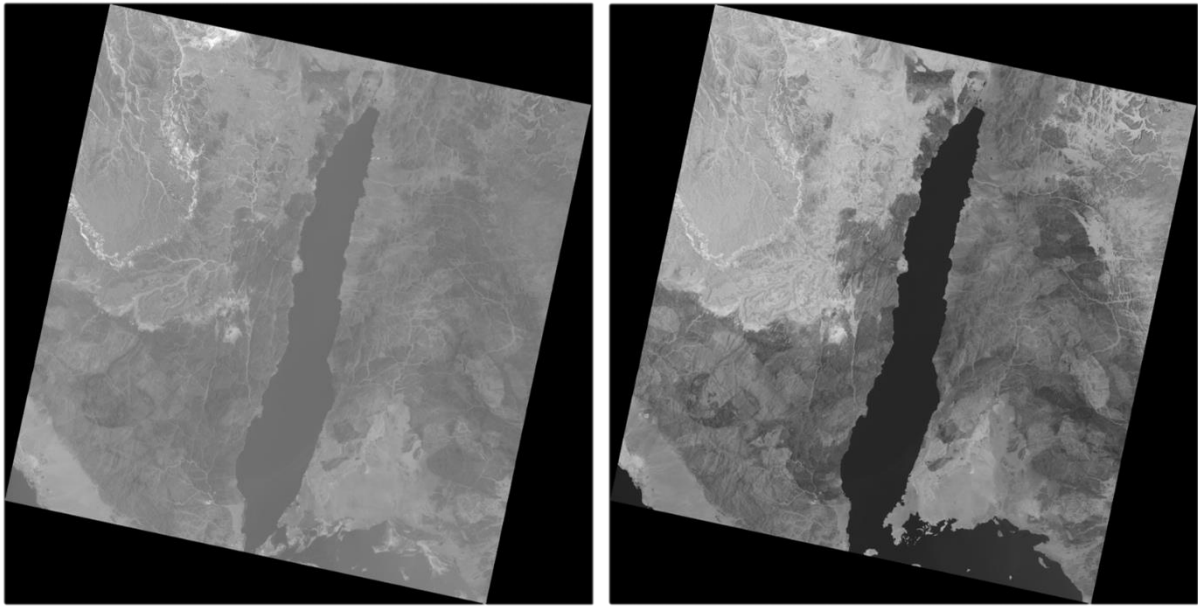


Figure4 : Comparison of the Blue band (left) and Shortwave Infrared (SWIR) band (right) of Landsat 8, around the Gulf of Eilat (the Gulf of Aqaba). The bounding box is clearly visible (black color = pixel value of 0 DN) as well as the difference in the amount of light absorbed by the water. Since darker pixels mean less light reaching the sensor, we can clearly see how in the SWIR band the sea absorbs significantly more light than the same area in the blue wavelengths.

Tools used in the study

An effort was made throughout the study to ensure that I used only open sourced, cross platformed, publicly available software and data. This should facilitate others to use our techniques without having to adjust or re-write parts of the code.

Python 3.x was chosen as the main scripting language, coupled with several external Python modules for specific tasks. These include Requests (© Kenneth Reitz 2019) for HTTP communication, Numpy (Van der Walt, 2011) for numerical computation, Scipy (Millman & Aivazis, 2011) for image filtering and simple linear regression, Pandas (McKinney, 2010) for structuring data, scikit-image (Van der Walt, 2014) for image processing, scikit-learn (Pedregosa, 2011) for calibrations and linear regression, Matplotlib (Hunter, 2007) for plotting, Rasterio (©MapBox 2016) for GeoTIFF processing, tqdm (da Costa-Luis, 2019) for progress monitoring and pyproj (© Jeffrey Whitaker 2019) for handling reprojections of geographic datasets.

The GIS software used early in the study were ArcGIS Pro 2.x and Global Mapper 14. In the later stages of the study I switched to QGIS 3.x, an open source GIS.

Sources for depth data

The ground truth data on which the calibrations were based was taken from the work of Dr. Hall (Hall, 2017). Dr. Hall manually digitized hundreds of nautical charts from various sources while solving the contradictions that arise from using different sources at different scales, accuracy and projections. This research used the relevant digitized nautical charts for the four study areas around the Arabian Peninsula.

Calibration techniques

After applying the SDB algorithm, a 2-dimensional array (hence: the uncalibrated array) is generated whose elements represent the quotient of the natural logarithm of the post-processed Blue and Green pixels. This array contains elements with NULL (or NoData) values which represent pixels in areas of dry land or in the bounding box, while the elements which have numeric values represent areas covered in water. These numeric values are unitless and they typically range between 0.9-1.03, when values smaller than 1.0 represent shallower areas as they indicate pixels where the Green wavelength was more absorbed compared to the Blue wavelength.

In order to transform this array into a meaningful bathymetry layer whose elements have units of depth, I applied a calibration process based on two different methods.

The Traditional Method: Calibrating against measured data

This method, which is well documented in the literature (IHO-IOC GEBCO Cook Book, 2015; Pe'eri et al., 2014), has a standard work protocol for achieving the calibration. This protocol consists of sampling the uncalibrated array against existing in-situ depth measurements, plotting a mean value of the sampling results, visually detecting a depth of extinction, using a simple linear regression for extracting the gain and offset parameters and using those values as coefficients for the calibration of each pixel. In this study I followed the main steps of the protocol while testing new methods for improving its accuracy. The final protocol that was implemented in this study had the following steps:

1. The in-situ depth measurements were loaded into the script as a Pandas data frame, which included the depth and the coordinates of each measurement. This data frame was 'cleaned' by removing entries such as non-number or NULL values as well as making sure that the data has only positive numbers.
2. The elements of the data frame were re-projected into the same projection as the original Landsat 8 scenes which were the source of the uncalibrated array. The re-projection was implemented by using the transform function of the pyproj module which takes as inputs both relevant projections.
3. Each element of the uncalibrated array which had a congruent data frame element was sampled against it, resulting in a new array (hence: the sampling array) comprising of coupling of uncalibrated values and depth measurements.
4. A mean function was used on the sampling array, resulting in a series of discrete depth measurements with a corresponding mean uncalibrated value.
5. The series of mean values was then used as the bases for the linear regression calculations. In a ten permutations repeat process, it was divided into a training set and a testing test (following the rule-of-thumb of 70%-30% respectively) and a linear regression model was used to find the scene which best fits the data in the study area (i.e., the scene that maximized the R^2 score).
6. Two other linear regression methods were tested on the best scene: Theil–Sen estimator (Dang et al., 2009), a method that for reducing that effects of outliers in the X direction (the in-situ depths) and Huber regression (Huber, 1964), a method for reducing the weight of the outliers. These methods were implemented using the scikit-learn module and were compared against the simple linear regression of ordinary least squares – the regression most often used in the literature (Pe'eri et al., 2014; Chénier et al., 2018; Kabiri, 2017).
7. The gain and offset parameters were extracted from the linear regression. These were used as the coefficients for calibrating each pixel of the uncalibrated array.
8. The resulting calibrated array was exported into a GeoTIFF as well as a feature class of linear contours.

Novel: Tides

In this study I tested a novel method for calibrating SDB in areas for which there were no in-situ measurements, using data derived from tides.

Tides are generated when there are differential gravitational forces between the Earth, the Moon and the Sun. These differential forces can be defined as (Hicks, 2006):

$$(5) D_m = \pm G \left(\frac{2ME\rho}{r^3} \right)$$

Where D_m is the differential forces between the Earth and the Moon, G is the gravitational constant, M is the mass of the Moon, E is the mass of Earth, ρ is the equatorial radius of Earth and r is the distance between the centers of mass of the Earth and the Moon. Similarly, for the tides generated due to differential forces between the Earth and the Sun:

$$(6) D_s = \pm G \left(\frac{2SE\rho}{r^3} \right)$$

Where D_s is the differential forces between the Earth and the Sun, S is the mass of the Sun and r is the distance between the centers of mass of the Earth, and the Sun. The sign of the equation depends on whether this is the side of the Earth facing towards the Moon or Sun or is it the side facing away. The actual movement of the bodies of water due to these forces are described as deep ocean wave motion, where the speed of the propagating wave is given by:

$$(7) C = \frac{L}{T}$$

Where C is the speed of the wave, L is its length and T is the period, i.e., the time interval between two successive wave crests. In shallow waters, as the wave propagated towards the shore or into a bay or estuary, its speed is reduced:

$$(8) C = \sqrt{gh}$$

Where g is the acceleration of gravity and h is the depth. This depth decreases as the wave approaches the shore, thus reducing C . Since the period of the wave is constant, the reduction in speed means also a decrease in the wavelength (Eq. 7), which has an effect of increasing the wave's amplitude. As tidal waves move into a bay, they are reflected upon themselves and form a standing wave whose form does not progress. The characteristics of this standing wave depends mainly on the characteristics of the estuary as its length determines the wavelength (L , Eq. 7) and thus the speed and height of the wave. Furthermore, the shape of the estuary also determines the location of the standing wave's nodes. i.e., the locations between the wave's maximum and minimum. If these nodes are located near the entrance to the estuary, the near-shore tide will be greatly amplified. While it is possible to predict the moment and amplitude of an oceanic tidal wave by using Eq. 5 and 6, it is harder to estimate when the signal of this wave will reach the shore. As stated above, the speed of the wave changes when it approaches the shore as well as the amplitude. Moreover, in some bays the furthest shores are separated from the ocean by straits which slows the wave and affects the location of the nodes. This can be seen, for example, in the Gulf of Eilat in which the tidal wave traverses over 2,000 km and passes both Bab el-Mandeb and the Tiran straits before reaching the shore.

The tidal-based calibration process required finding satellite images captured during high and low tides at the research areas. Since the complicated prediction of nearshore tidal waves was beyond the scope of this study, I used past tidal measurements from the governmental agencies of Canada and Australia to find the parameters required for the calibration.

My aim was to generate an SDB layer describing the depths during mean tide (Z_m), i.e., the depth between high tide (Z_t) and low tide (Z_e). This was achieved by finding

the function (f) that correlates the water depth during high tide at each pixel in the research area with the log-band ratio calculated for that scene. This function was assumed to be linear, similar to the model used in the traditional calibration:

$$(9) f(R) = Z_0 + aR$$

Where Z_0 is the depth at the shoreline and R is the log-band ratio.

The linear regression was calculated on the log-band ratio during high tide (R_t) and it was based on two data points. The first point was the log-band ratio during high tide sampled at the specific location used for measuring the water depths, as published by the governmental agencies. The mean water depth at these locations is given by:

$$(10) Z_m = Z_t - Z_e$$

The second data point was manually sampled by examining the difference in the shoreline between high and low tides. Since during high tide the shoreline advances towards the land, there exists some areas that are above water during low tide but will be covered by water at high tide. The pixels of these areas can be identified in a scripted method by subtracting the below-water pixels at low tide from their high tide equivalents, thus generating a raster whose pixels have data only in the high tide shoreline and NULL values everywhere else. The value of those pixels – the quotient of the log-band at high tide – were sampled and became the second point for the linear regression. I then calculated the parameters of this linear regression and used them as linear coefficients for the calibration of the high tide SDB. From this layer I subtracted the depth at low tide (Eq. 10) in order to generate an SDB layer corresponding to the mean tide.

The study areas that were chosen for testing this method have a large tidal amplitude of 6-10 m, which was assumed to reduce effects of inaccurate measurements. In these areas there is also a reliable, publicly available source for tidal measurements.

The Work Process

The overall work process used for part A and B of stage 2 was divided into several logical steps, as illustrated in Fig. 7 and detailed below.

Image Acquisition

The data warehouse used in this study was Amazon's AWS Public Dataset Program, chosen for its high availability and ease of search and access. Amazon provides a continuously updated Comma-Separated-Value (CSV) file with a list of all available scenes, including searchable metadata describing cloud coverage percentage, data tier level, acquisition time and the scene's URL which points to list of downloadable GeoTIFF images representing the different bands of that scene.

In Part A of Stage 2 of the study I identified a path/row for the various study areas. For each path/row a list of all available, Tier-1 scenes with a maximum cloud coverage of 0.1% was created from Amazon's CSV scenes lists. For each scene the three respective bands were downloaded simultaneously from Amazon's servers using the Requests module and utilizing three parallel threads.

In Part B of Stage 2 of the study I selected from Amazon's CSV scenes lists the scenes with an acquisition time corresponding to the high and low tides of the study areas. Similar to part A, the three bands of each scene were downloaded simultaneously from Amazon's servers using the Requests module and utilizing three parallel threads.

Land-water separation

The amount of light absorbed by water depended greatly on its wavelength (Fig. 5). Water reflects light in the visible spectrum while absorbing infrared light. In the Landsat 8 Infrared images this is represented by pixels with low DN values over wet areas, as opposed to higher values over dry land (Fig. 4).

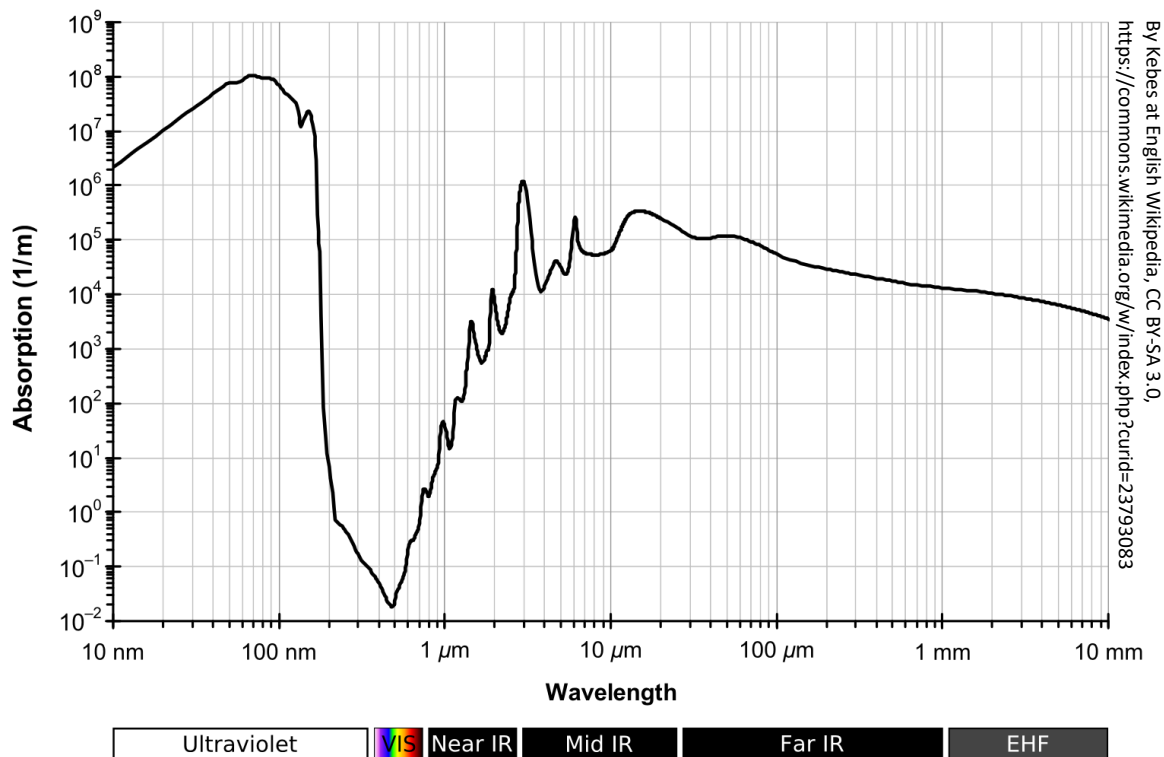


Figure5 : Absorption of light in different wavelengths by water. The minimum of absorption is at the blue and green wavelengths while the near and mid infra-red are much more absorbed.

I used this fact to perform an automatic thresholding technique for distinguishing between water and dry land by applying Otsu's thresholding method (Otsu, 1979) on band 6 (Table 1). This algorithm exhaustively searches for the threshold value that maximizes the inter-class pixel value variance of two classes (Fig. 6). Once the threshold value is found, the image can be binarily spilt, one class representing the wet areas and the other represents dry land. The pixels of the image that were found to be parts of the wet areas were used as an image mask for the following steps, so that no calculations were performed on dry land. Special care was given for the pixels with a value of 0 DN, since those represent the blocking rectangle and not the actual image.

This step was implemented using the Rasterio module for reading and writing the various GeoTIFF images while the binary thresholding and the implementation of Otsu's method was done with the scikit-image module. This process improves

previous methods for separating land from water that rely on manually searching for the threshold value, both in terms of speed and accuracy.

Lucas (CA) [CC BY-SA 4.0
 (https://creativecommons.org/licenses/by-sa/4.0)], via Wikimedia Commons

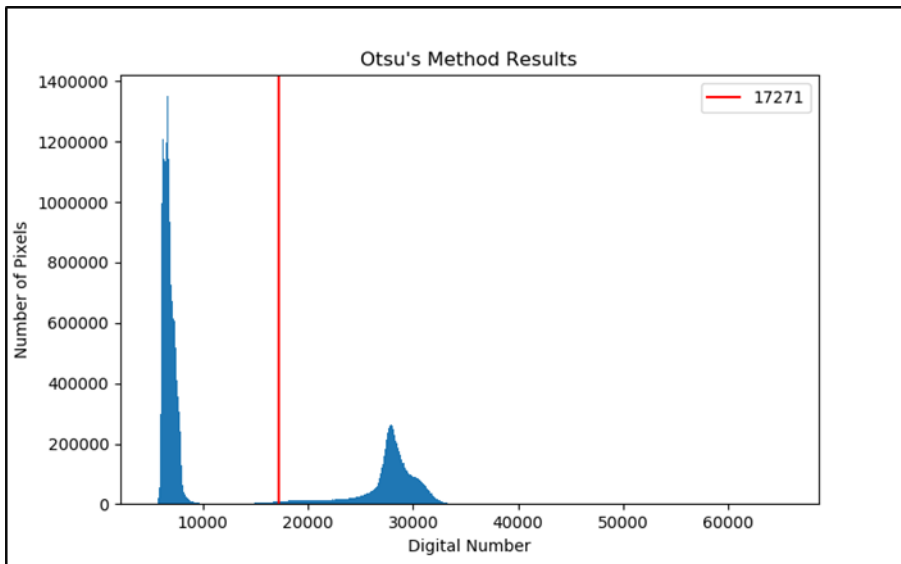
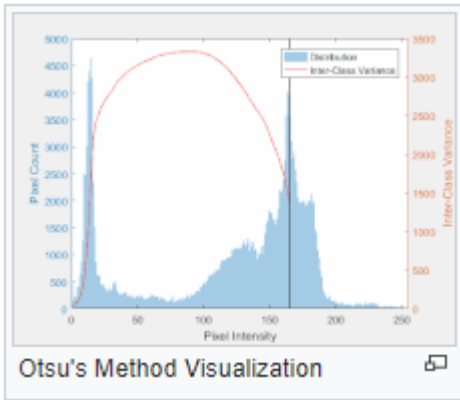


Figure6 : A visualization of Otsu's method for binary thresholding (above). The maximum value of the variance separates the image into two areas based on the pixel's values. The results of implementing this method in the study area near Qatar (below) clearly shows the separation into two distinct classes with the threshold value found at pixel value of 17,721 DN.

Image processing

The blue and green bands, which are the components of the SDB algorithm, went through a series of image processing steps designed to prepare them for the algorithm's calculation. These steps included:

- I. Changing the pixel data type from 16-bit integers (i.e., the original DN values) to 64-bit floating points to ensure minimal data loss in the following steps as well as to enable registering NULL values.
- II. Applying a low-pass filter to minimize outliers and noise in the data. This step was implemented using a median filter from the Multidimensional Image Processing package, a part of the Scipy module. This filter was calculated upon the surrounding 3x3 neighboring pixels for each pixel in the image, while a reflecting technique was used for the borders, under the assumption that the pixels immediately outside the scene's borders are very similar to their neighbors inside.
- III. Using the class representing dry areas from the land-water separation step, the corresponding dry areas in the Blue and Green images were removed (marked as NULL values with the Numpy module). The resulting images have pixel values only in areas that were found to belong to the water class.
- IV. The pixels of the containing rectangle, which had a DN value of 0, were also marked as NULL values.
- V. A natural log was calculated for each pixel using the Numpy module.

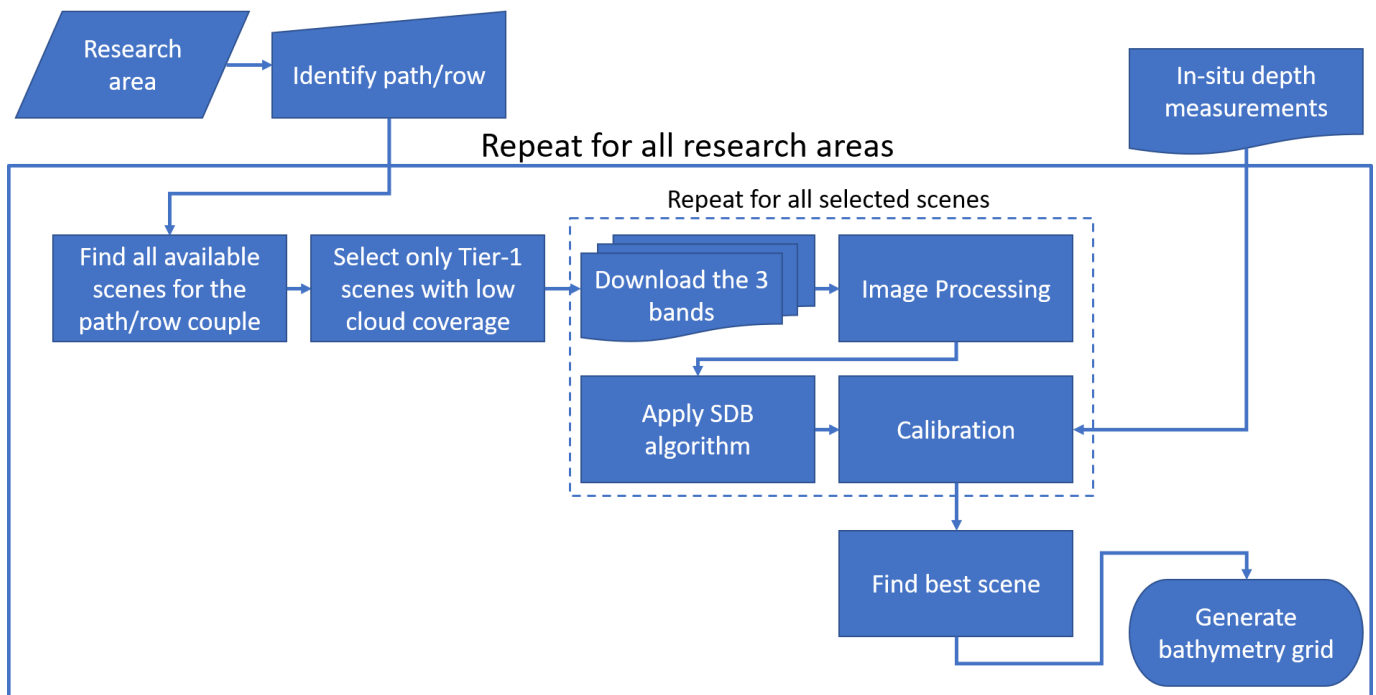


Figure7 : The overall SDB process used in this study, divided into logical steps.

Applying the SDB algorithm

Having two arrays of the water area of the scene, one for the blue wavelength and one for the green wavelength, with their pixels representing the natural log of the original DN value (post image processing), the SDB algorithm was calculated as a simple quotient of the two bands (Eq. 2.), resulting in an array whose shape is the dimensions of the original scene – 7301 rows and 7271 columns and whose values are the quotient.

Sampling

In order to sample the in-situ depth data against the results of the SDB algorithm, i.e., obtain a table consisting of the in-situ depth measurement with the SDB algorithm pixel value overlapping each specific depth data, both datasets were required to be in the same coordinate system. While each Landsat 8 scene has a known projection in the Universal Transverse Mercator projection (using the WGS84

datum), the in-situ data had different projections as it arrived from different sources. Thus, in each study area the in-situ data's projection had to be pre-known and re-projected to match the projection of the satellite image. This was achieved in two steps:

1. While opening the SWIR band for the preparation of the Otsu's thresholding the coordinate system of the specific scene was registered.
2. When the script reached the sampling part, the in-situ data was re-projected to the coordinate system from step 1. This was implemented using the pyproj module which applied an affine transformation.

Once both datasets were in the same coordinate, the sampled table was generated using the Pandas module.

Calibrating

In order to transform the SDB algorithm into a meaningful depth grid, its pixels needed to be converted from dimensionless units to units of length (meters). This transformation was achieved by applying a linear equation on each pixel, so that:

$$(11) \quad d = m_1 p + m_0$$

where d is the pixel in depth units, p is the dimensionless pixel and m_1 , m_0 are the coefficients that result from the linear regression.

All the available scenes in each study area were linearly fitted against the in-situ depth data using the ordinary least squares regression method. The scene which had a maximum R^2 score was selected as the best scene and was calibrated using the parameters calculated from the linear regression. That scene was then fitted against the in-situ data using the different linear regression methods.

Saving the results

After applying the linear transformation and obtaining an array whose elements have units of depth, a bathymetry grid was generated. This was achieved with the Rasterio module in a process whose inputs were the array, the coordinate system of the original SWIR band and the desired format. All the grids were generated as a single band GeoTIFF with 32-bit pixels whose values represent the water depth in meters. A vector GIS file of linear contours was later generated from the GeoTIFF using a GIS software.

Results and Discussion

Stage 1: Automating the work process

The manual work protocol was fully automated and replaced with a scripted protocol (Fig. 7). The difference between the two protocols is summed in Table 2:

Work protocol logical step	Manual protocol	New, automated protocol
Finding the best scene	Visually selecting the best scene from the available scenes in the archives	Working on all the available Tier-1 scenes, choosing the best scene by minimizing the model's error
Downloading the scene	Manually downloading by a web browser interface	Scripted, multithreaded downloading through GET HTTP requests
Extracting the 3 bands needed for the protocol	Un-zipping the downloaded archive, deleting the unnecessary bands	Downloading only the 3 bands
Pre-processing (changing pixel type, low-pass filtering)	Manually with a GIS software	Using the Python script
Cloud removal	With a GIS software creating polygons that spends areas with both clouds and clear sky. Sampling and applying linear regression for removing the clouded areas.	Made obsolete by selecting only scenes with minimal (less than 0.1%) cloud coverage

Work protocol logical step	Manual protocol	New, automated protocol
Separating land and water	Manually looking for a threshold value – either visually or by examining the histogram of the image	Applying Otsu’s method for automatic thresholding
Applying the SDB algorithm	Manually with a GIS software	Using the Python script
Re-projecting the in-situ depth data to the scene’s coordinates	Manually with a GIS software	Using the Python script
Sampling the SDB algorithm layer against the depth data	Manually with a GIS software	Using the Python script
Applying linear regression, finding the parameters and depth of extinction	Manually, usually with Excel or another electronic worksheet software	Using the Python script
Generating a bathymetry grid	Manually with a GIS software	Using the Python script

Table2 : The differences between the original work process and the new process used in this study.

Stage 2, part A: Generating SDB layers

I applied the scripted work protocol developed in stage 1 in four study areas: The Gulf of Eilat (Gulf of Aqaba); the Dahlak archipelago, Eritrea; Bab el-Mandab straits; Bahrain and western Qatar (Fig. 8).

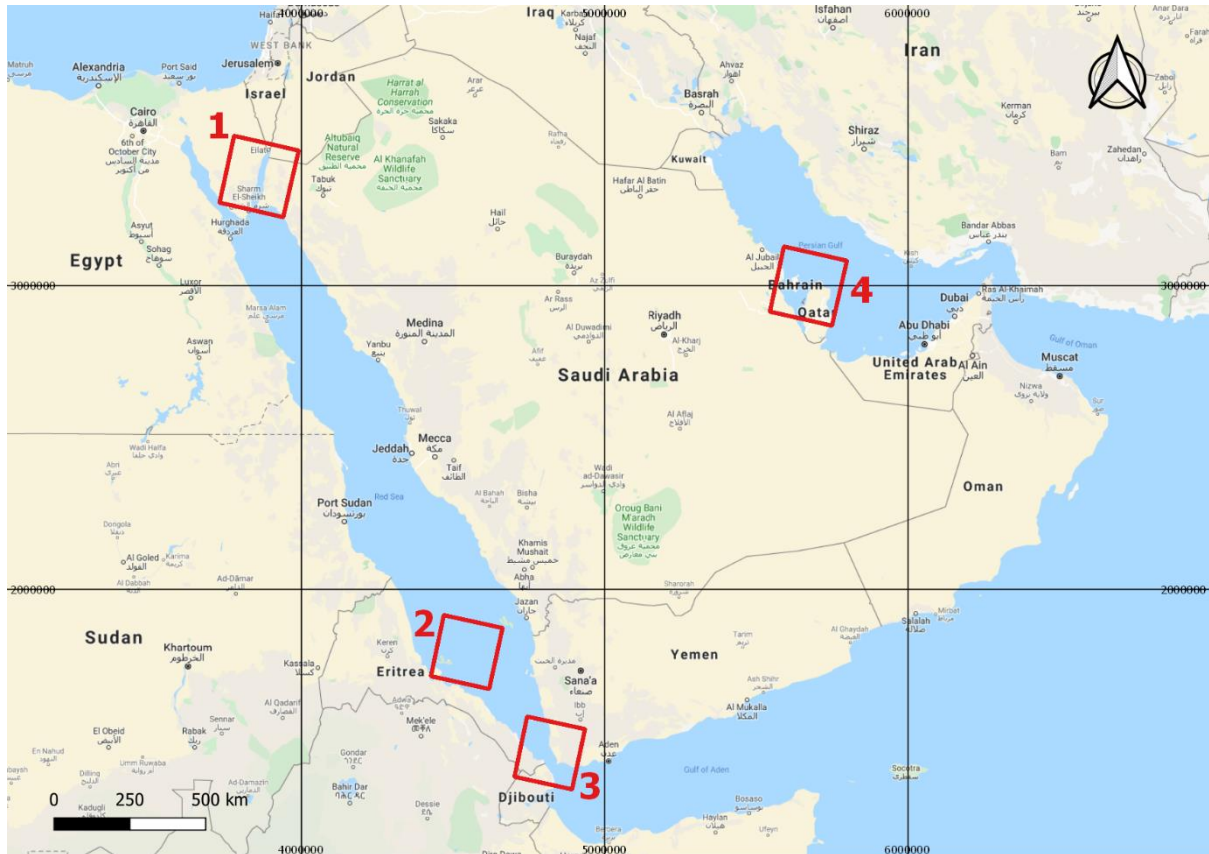
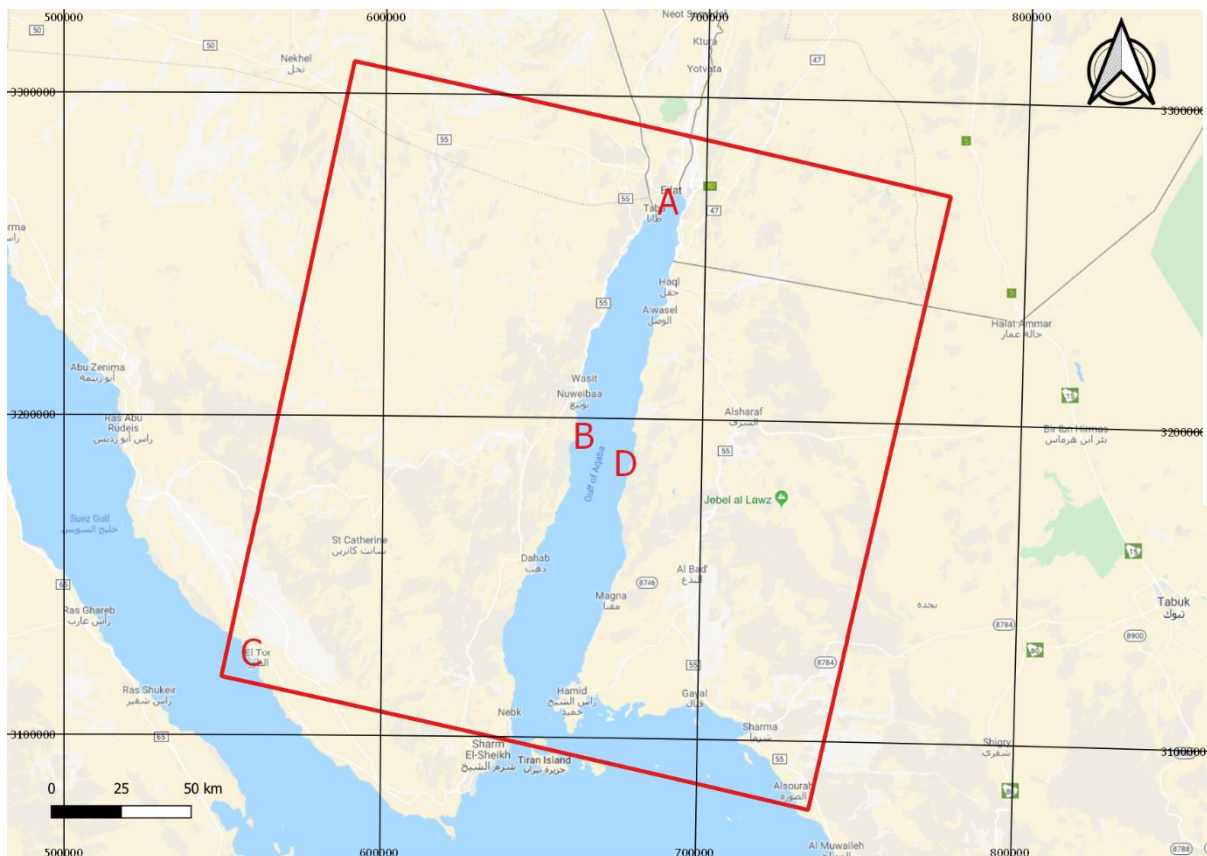


Figure 8 : The four study areas used in stage 2, part A: The Gulf of Eilat (1); the Dahlak archipelago, Eritrea (2); Bab el-Mandab straits (3); Bahrain and western Qatar (4).

The Gulf of Eilat

The Landsat 8 scene that covers the northern area of the Red Sea (path 174, row 40 in the WRS-2 coordinate system) extends over a large area of land and a smaller area of water (Fig. 9) as the water takes 14% of the total pixels. This area tends to be less covered in clouds, thus the script had over 60 available scenes with a cloud coverage of less than 1%. Out of those scenes 8 were chosen for the analysis, having a cloud coverage of 0.01%.



Basemap: © Google

Figure 9 : An overview map of the study area at the Gulf of Eilat. The red rectangle indicates the boundaries of the Landsat 8 scene used for the SDB and the letters A-D signify the locations shown in the figures 14-17 respectively.

Two separate datasets were available as the in-situ data points for the calibration (Fig. 10). One dataset with 27,000 points from the work of Dr. John Hall and another dataset with 55,000 points generated by eco-sounding sampling made at the IUI in Eilat. While the first dataset covered the entire scene, its data was inconsistent and could not be used for SDB. The second dataset was therefore used but since it was gathered only very close to Eilat it is not clear how well it describes the bathymetry of the more southern areas.

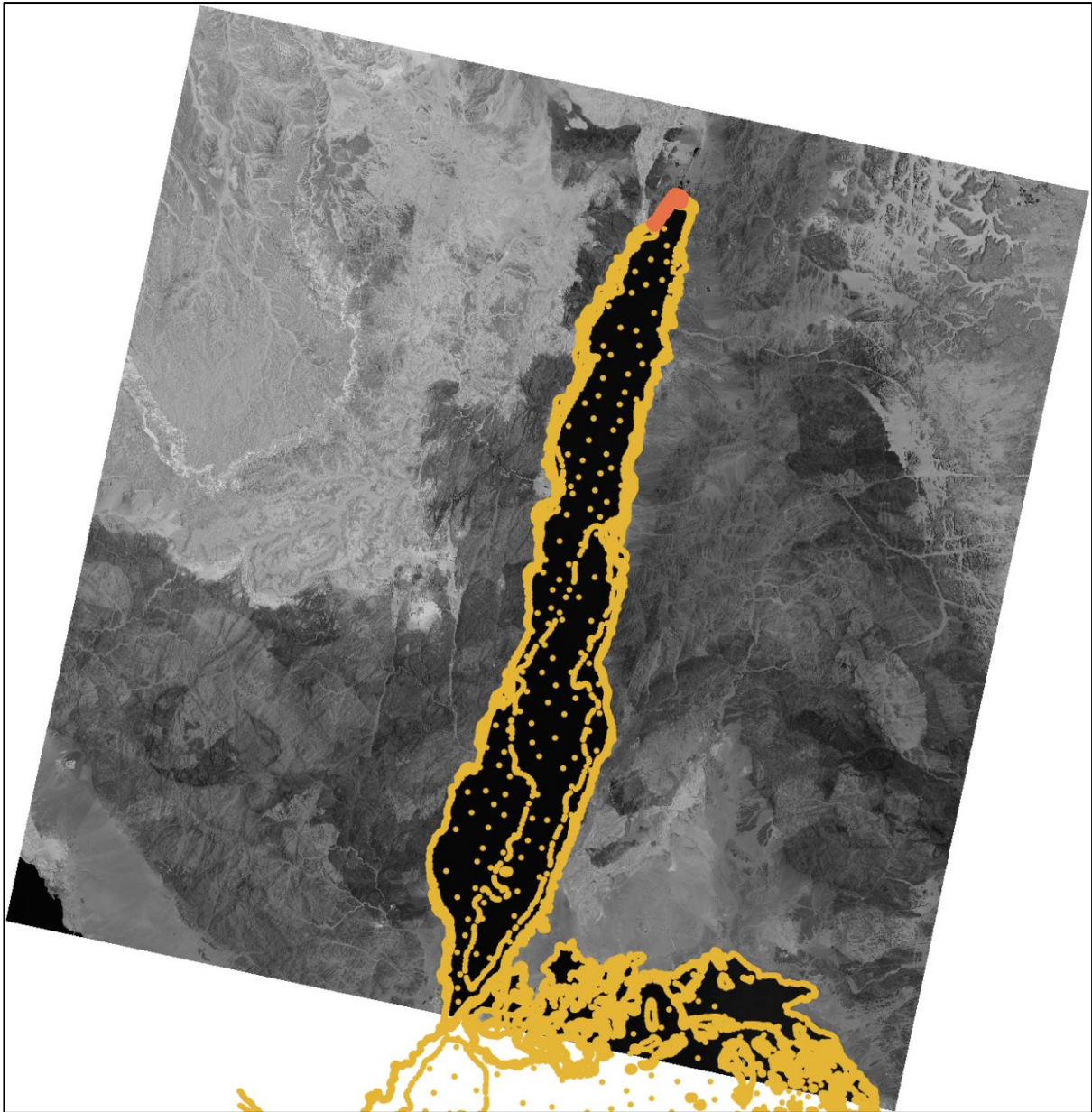


Figure10 : The datasets used as in-situ data points for the calibration. The yellow points were the results of the nautical charts digitization done by John Hall and the red points were generated at the IUI in Eilat by eco-sounding close to shore. While Hall's dataset covers the entire scene, it was inconsistent and could not be used for the calibration. On the other hand, while the data collected at IUI had better quality, it only represents the northern part of the gulf.

The relatively small amount of water pixels challenged the process of thresholding using Otsu's method. In Fig. 11 we can see that the first threshold value found by this method was at 21,757 DN, a value that does not correctly divides the image into the two classes. Therefore, a second run of the Otsu's method was executed on the resulting image. This second run had a thresholding value of 12,998 DN which better separates the land and water classes.

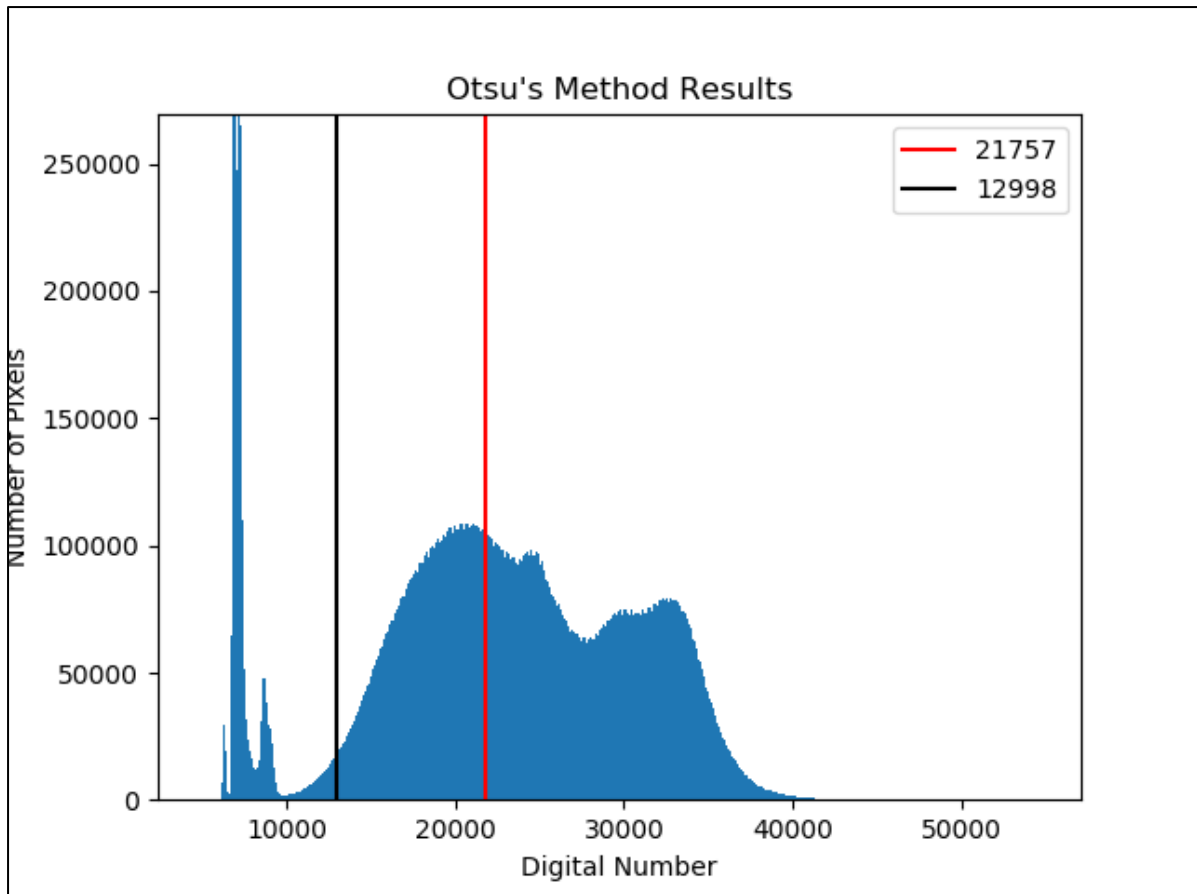


Figure 11 : The results of Otsu's method for thresholding implemented on the SWIR band at the Gulf of Eilat. Two separate script runs were needed in this scene as the first run found a threshold value that was not able to accurately divide the pixels into the two classes of land and water.

The scene which best fitted the in-situ dataset was taken on 10/06/2016. The linear regression had a R^2 score of 0.869 at a depth of 13.4 m, while similar R^2 scores can be achieved by choosing a depth of extinction of 17 m (Fig. 12).

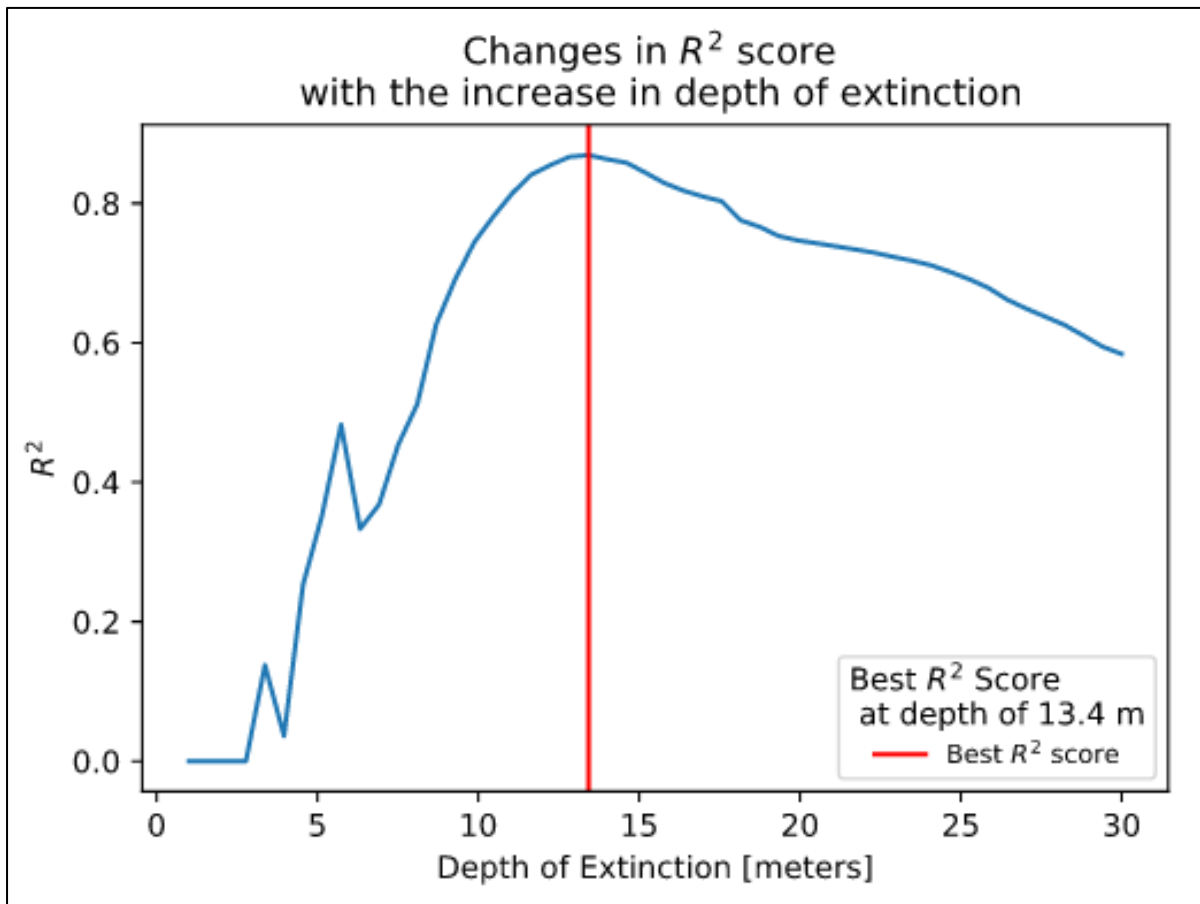


Figure 12 : An analysis of the changes in R² score with the increase of the depth of extinction. The best R² was found at 13.4 m, while higher depths can also be used as a depth of extinction with a relatively high R² score.

In Fig. 13 we can see the results of the linear regression. Out of the 55,000 in-situ data points available, 6,900 (13%) data points were below the depth of extinction and suitable for the linear regression calculation. In depths greater than the depth of extinction the model loses its ability to predict the water depth from the log-band ratio indicating that the log-band value of 1.022 signifies the light returning from the body of water and not from the bottom.

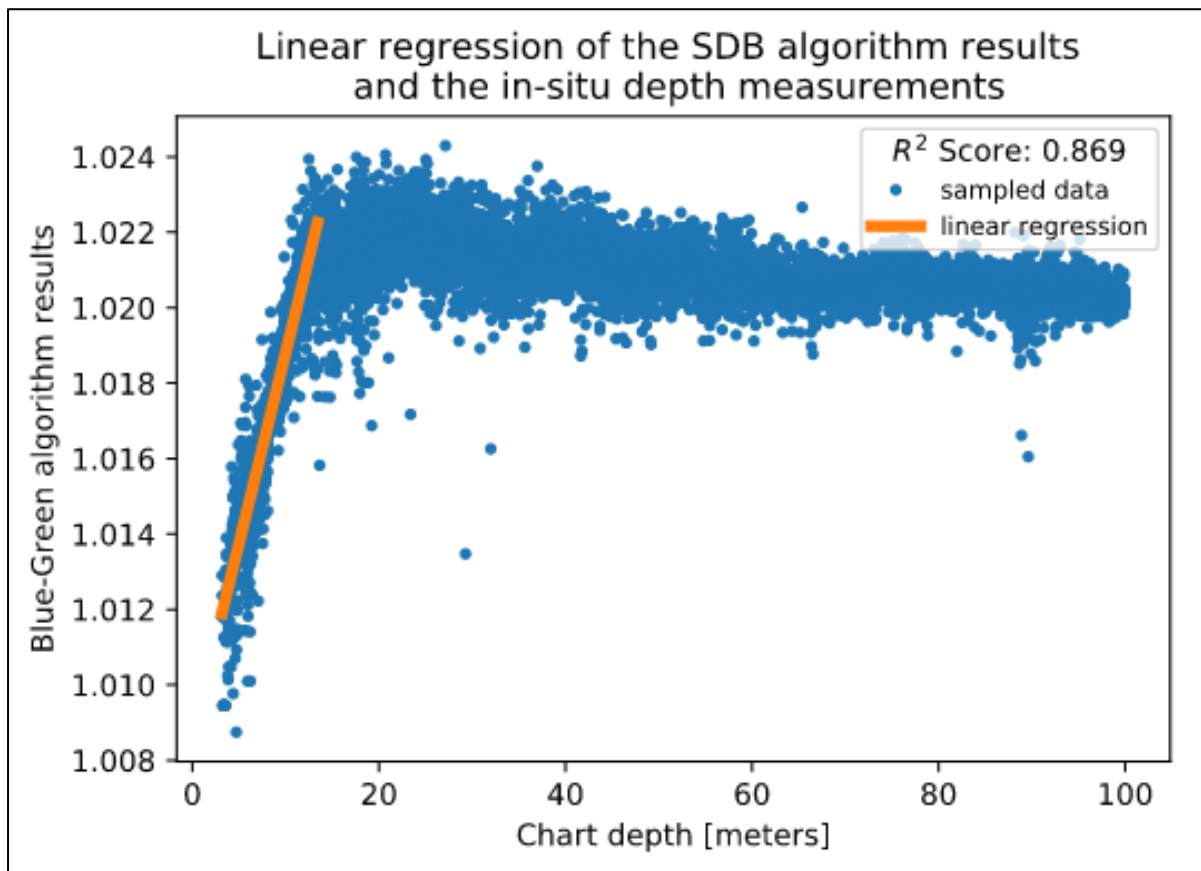


Figure13 : The linear regression used in this study area. The model suggests a linear relationship between the Blue-Green band ratio and the in-situ depth measurement up to the depth of extinction. In deeper depths the linear model loses consistency as the the light recived at the sensor comes from the body of water and not from the bottom.

In the following figures, Figs. 14-17, we can see the results of the SDB layer at the study area. The Raster was transformed into contours of 1 m steps for the visual interpretation of the results. We can see that the contours tend to describe correctly the shape of the shorelines as well as find submerged structures. In figure 17 we can see contours that were generated at the deeper water that do not follow the actual bathymetry. As these depths should be higher than the depth of extinction, the contours there may be the results of unclear water.



Figure14 : The SDB results near the IUI in Eilat, location A in the overview map. The white contours indicate the bathymetry, i.e., the depth at that location.



Figure15 : The SDB results at location B. We can see the contours at the shoreline as well as the contours around submerged structures, about 0.5 km off the shore.



Figure16 : The SDB results at location C, near El-Tor, Egypt. We can see the bathymetry at the shoreline and at the small bay. Contours lines of submerged structures are also visible.

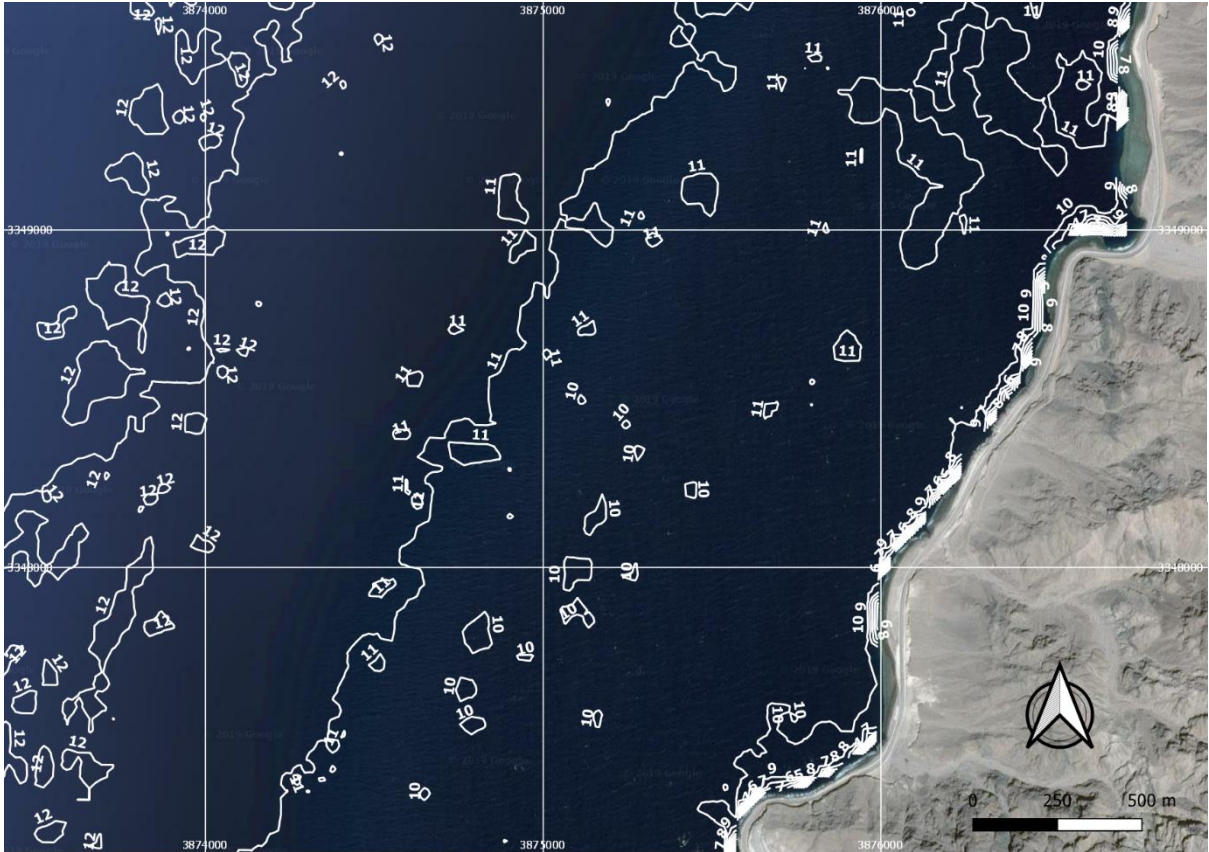


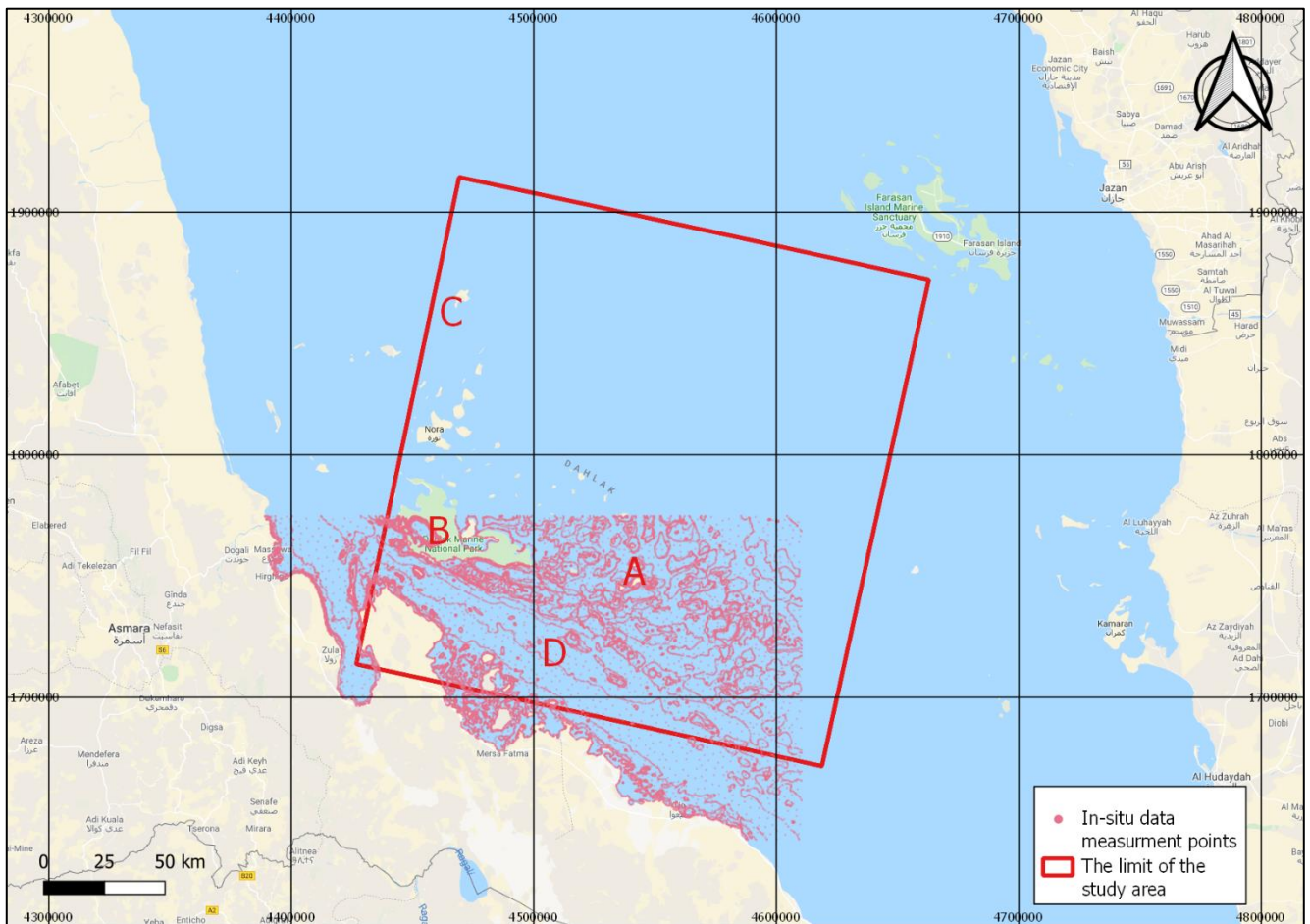
Figure17 : The SDB results at location D, at the eastern shores. We can see the bathymetry following the shoreline as well as misleading contours generated at the deeper waters. These may be the results of abstractions in the reflectance of light or indications of turbulence in the water.

The Dahlak Archipelago

The Dahlak archipelago study area at the eastern shores of Eritrea contains a very small area of land as the water takes 95% of its pixels (Fig. 18). This area has several islands of various sizes as well as a peninsula at its south-west corner.

The SDB process in this study area had a collection of nine Landsat 8 scenes for its imagery input (path 148, row 69 on the WRS-2 coordinate system), all having less than 0.1% of cloud coverage.

The in-situ dataset used for the calibration in this area was generated by John Hall and consisted of 30,000 points in total, 20,000 of them were inside the boundaries of the scenes used here.



Basemap: © Google

Figure 18 : An overview of the Dahlak archipelago near Eritrea. This study area consists mainly of water with several islands of various sizes. The pink points are the in-situ measurements that were available for the calibration and the red rectangle represents the limits of the Landsat 8 scene used here. The letters A-D are the locations of the figures 22-25, respectively.

Otsu's method for thresholding successfully divided the pixels into the two classes (Fig. 19). The threshold value was found to be at 12,916 DN.

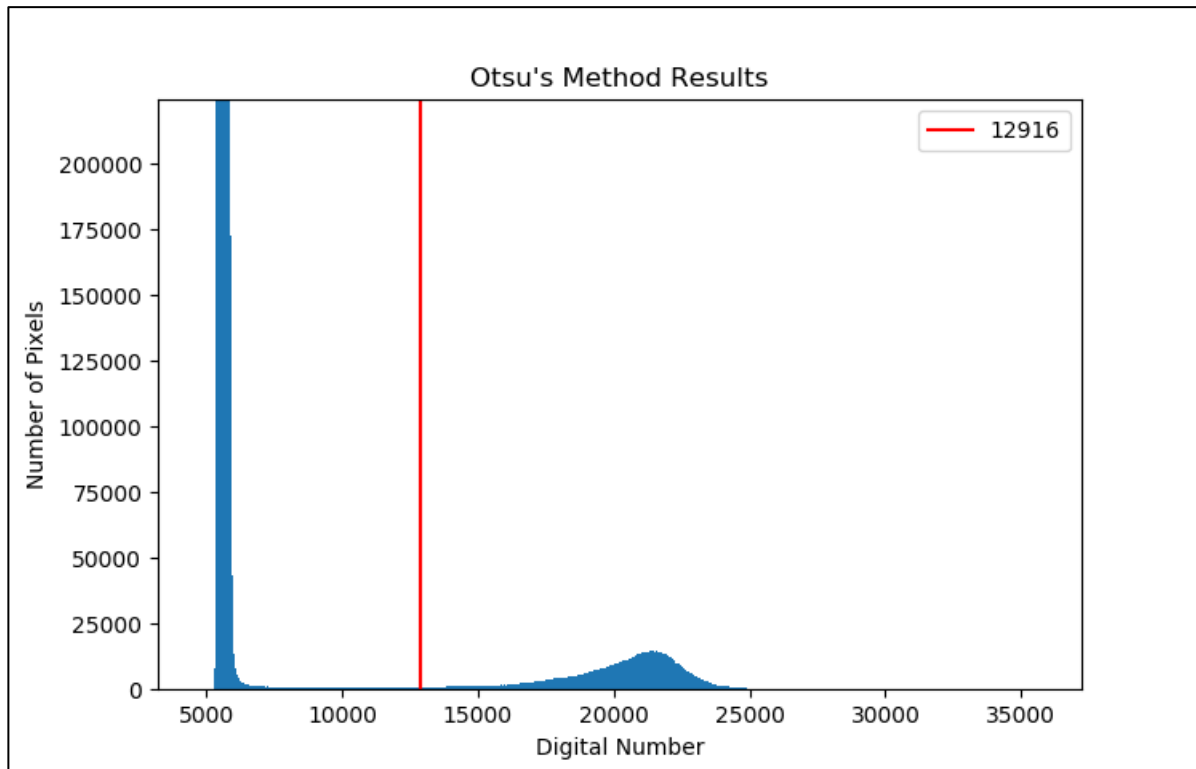


Figure 19 : The results of Otsu's method for thresholding implemented on the SWIR band at Dahlak, Eritrea. This method was successful in splitting the pixels into the two separate classes of land and water with a thresholding value of 12,916 DN. Since the water takes 95% of all the pixels in this scene, the graph had to be cut on the vertical axis for the land class to be visible.

The scene which best fitted the in-situ dataset was taken on 10/11/2017. The linear regression had a maximum R^2 score of 0.568 at a depth of 6.9 m (Fig. 20). Since similar R^2 scores are found up to depths of 11 m, this depth was chosen as the depth of extinction. Beyond the depth of extinction, the R^2 score drops, indicating that in these depths the linear model does not accurately correlate depths with the log-band ratio.

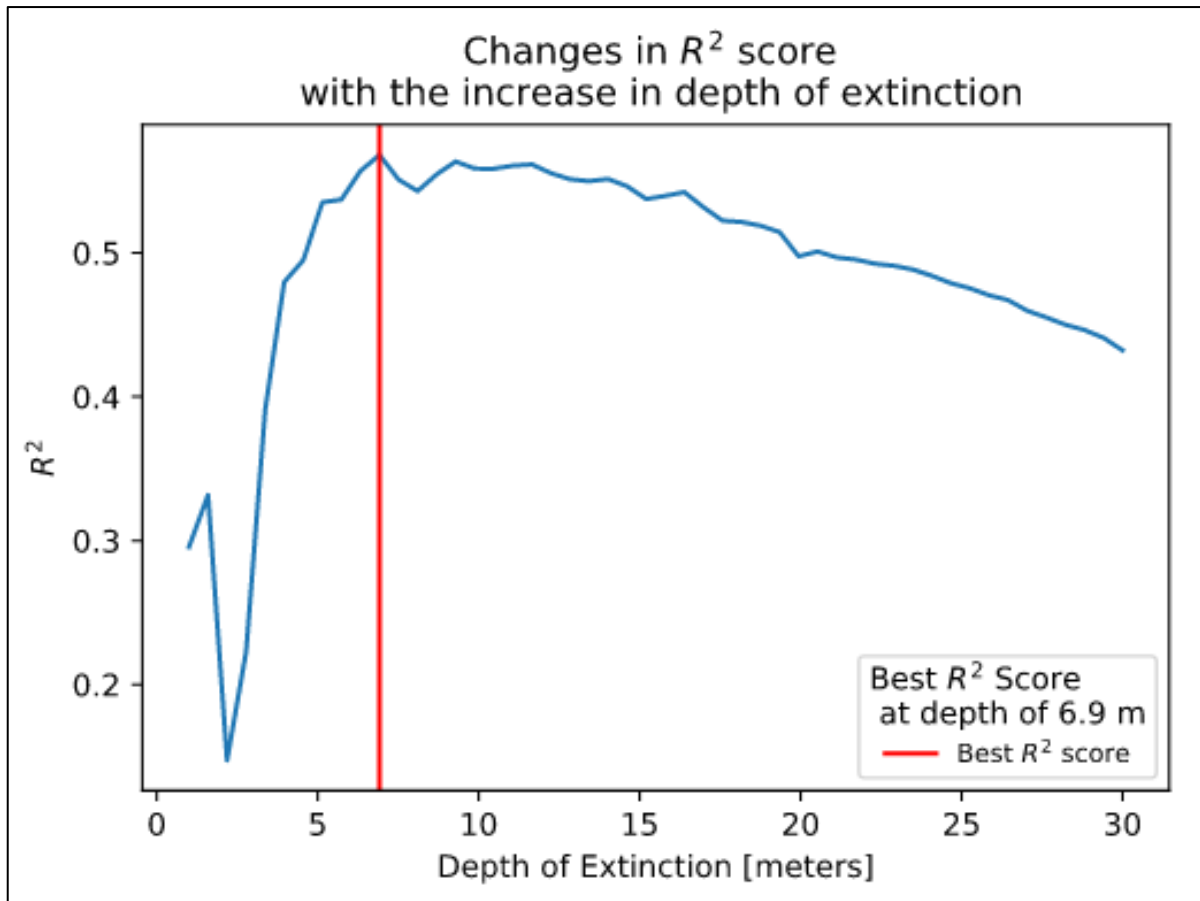


Figure20 : An analysis of the changes in R2 score with the increase of the depth of extinction. the best R2 was found at 6.9 m, while depths of up to 11 m could also be used with a similar R2 score.

In Fig. 21 we can see the results of the linear regression, both up to the depth of the best R² value and up to the depth of extinction. Out of the 20,000 in-situ data points available, roughly 9,500 (48%) data points were below the depth of extinction and suitable for the linear regression calculation. In depths greater than the depth of extinction the model loses its ability to predict the water depth as the graph flattens at the log-band ratio of 1.020, indicating that this value signifies the light returning from the body of water and not from the bottom.

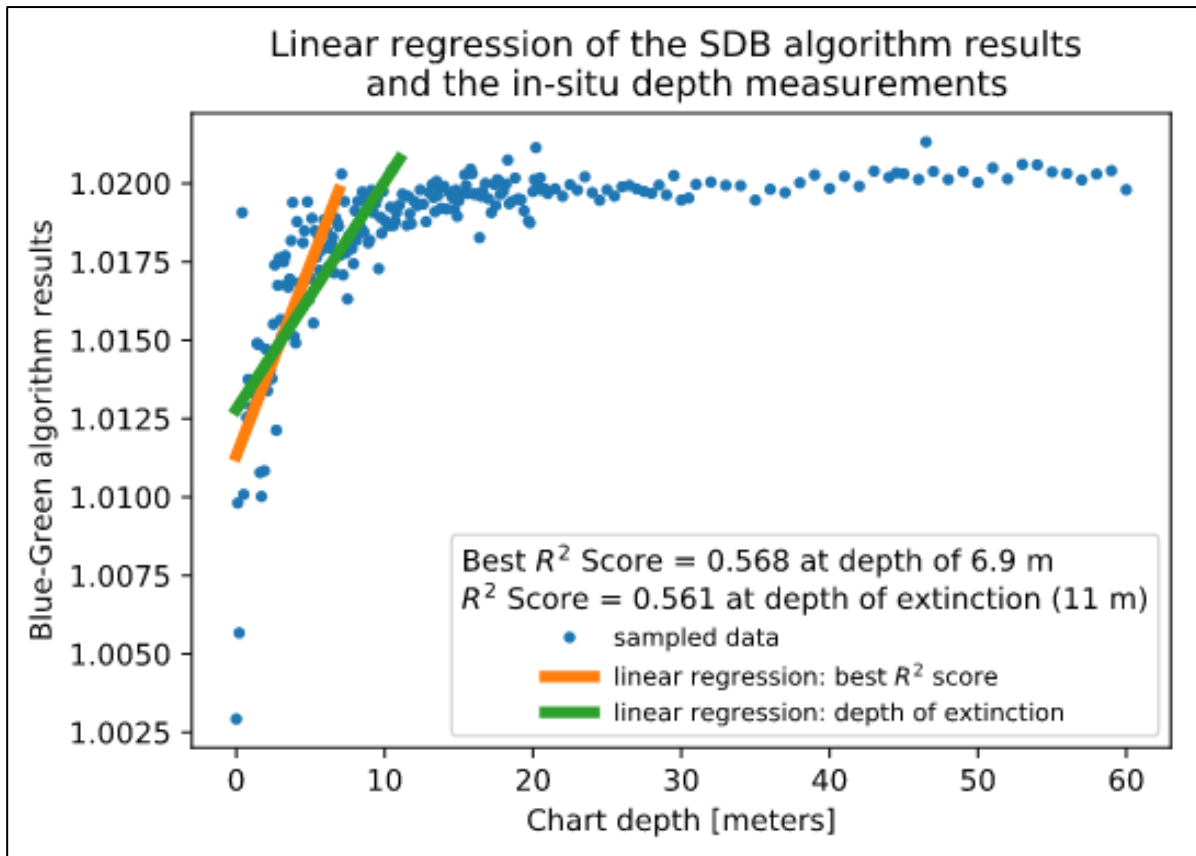


Figure21 : The linear regressions used in this study area, both up to the depth that has the highest R^2 score and up to the depth of extinction. At the Blue-Green band ratio of 1.020 the graph flattens, indicating light reflecting from the body of water and not the bottom.

In the following figures, Figs. 22-25, we can see the results of the SDB layer at the study area. The Raster was transformed into contours of 1 m steps for the visual interpretation of the results. We can see that the contours tend to describe correctly the shape of the shorelines around the many islands as well as locate submerged structures that are invisible in a standard true colored image (Fig. 23). In figure 24 we can see contours that correctly follow the islands at the north-west of the study area, over 150 km from the in-situ measurements. This would suggest some uniformity in the SDB. In Fig. 25 we can a multitude of contours around a submerged structure, possibly pointing to noise from turbulence or atmospheric sources.

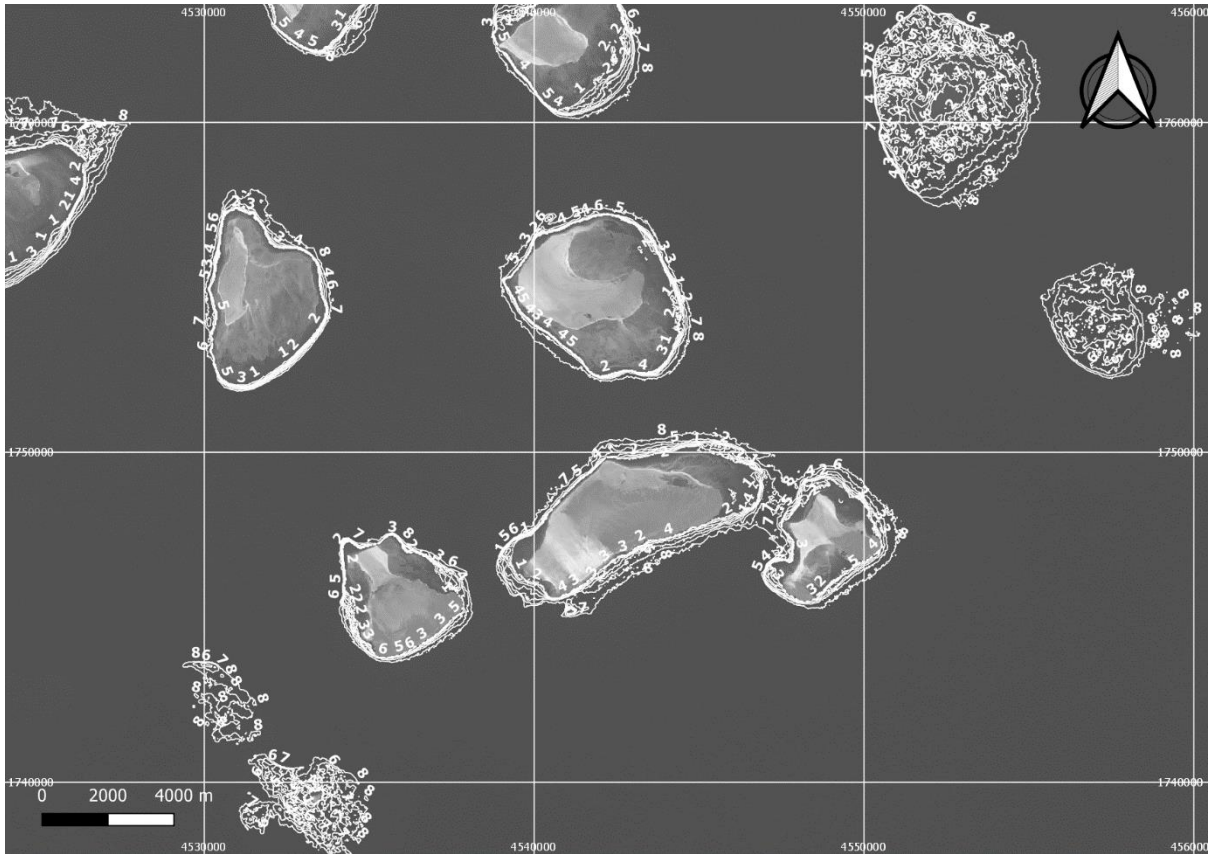


Figure22 : The SDB results around the various islands (location A in the overview map). The background image here is the panchromatic Landsat 8 image corresponding to the scene chosen for the SDB generation. We can see that the contours correctly follow the different shorelines and the SDB was also able to identify submerged islands at the north-east corner of this map.

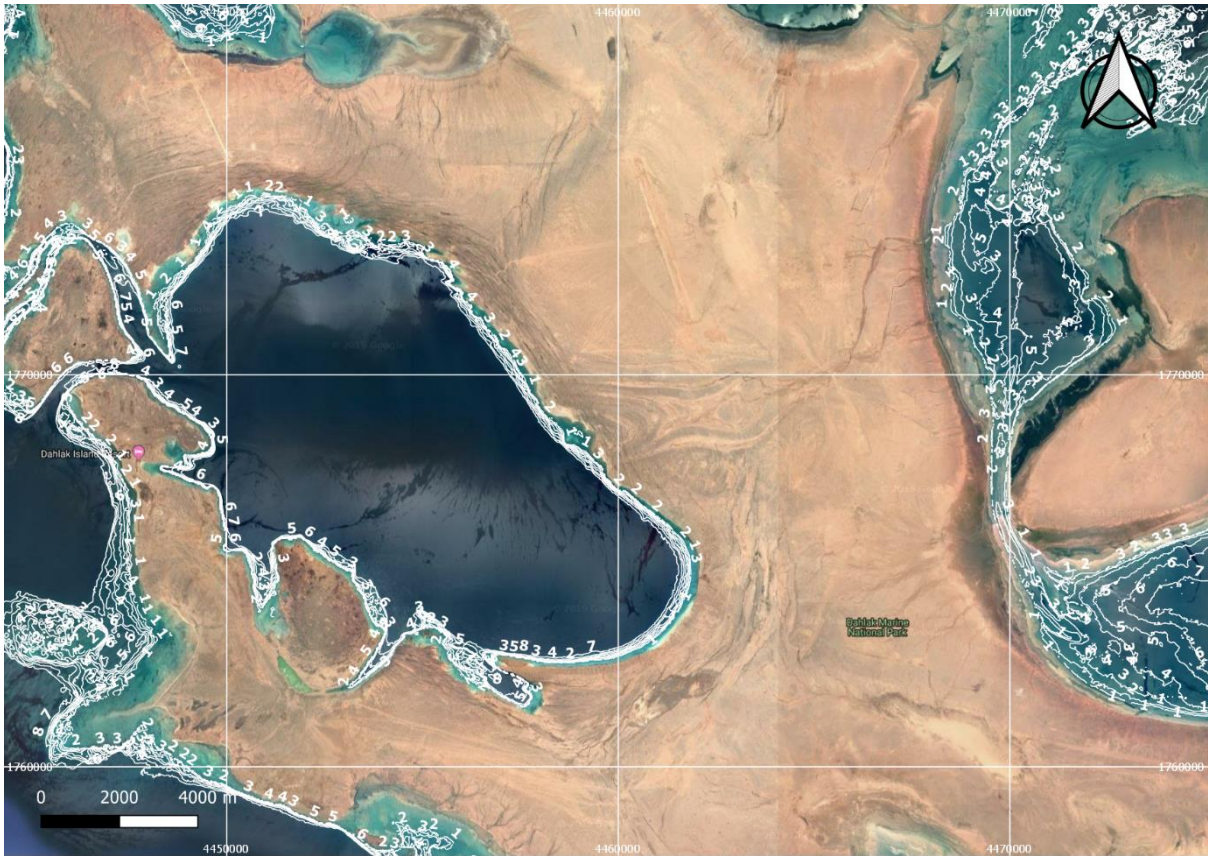


Figure23 : The SDB results at location B, set on a background of Google's global imagery. We can see the contours following the shoreline of the inlets.

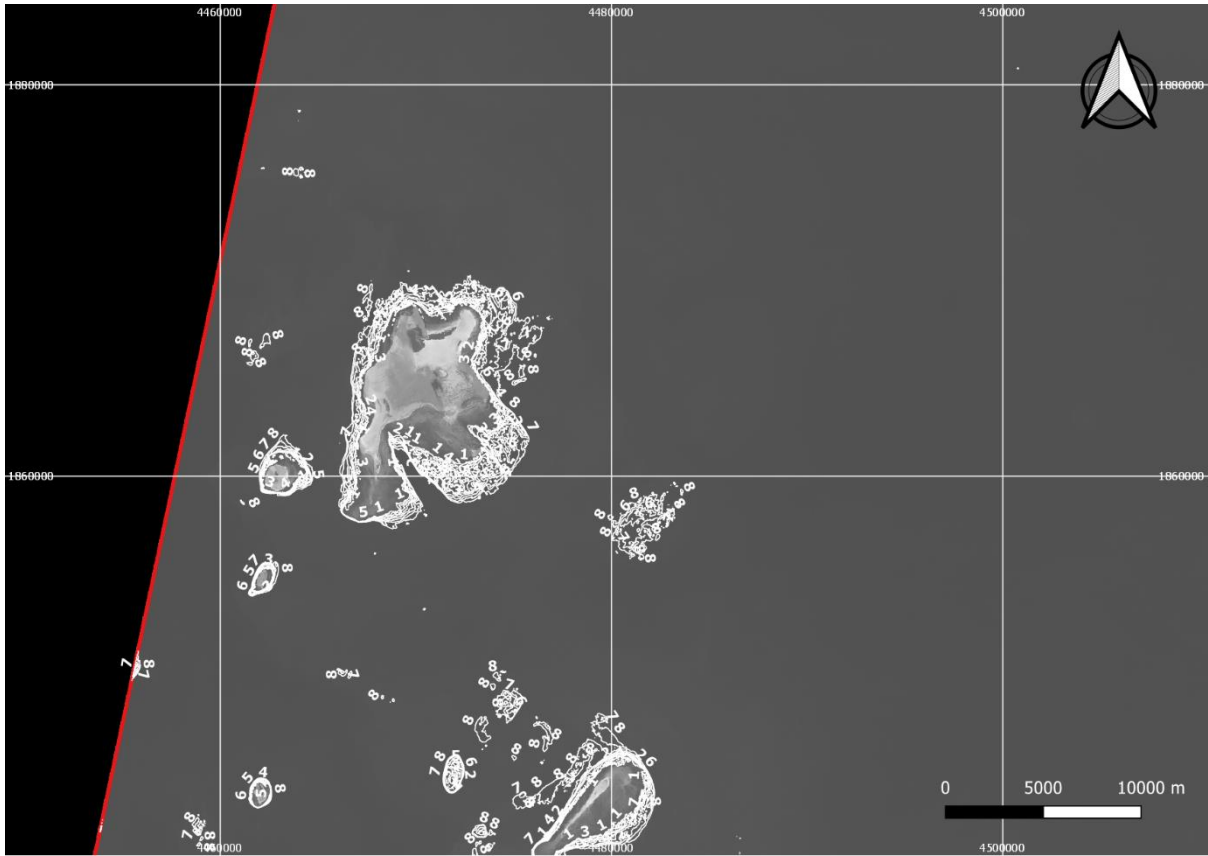
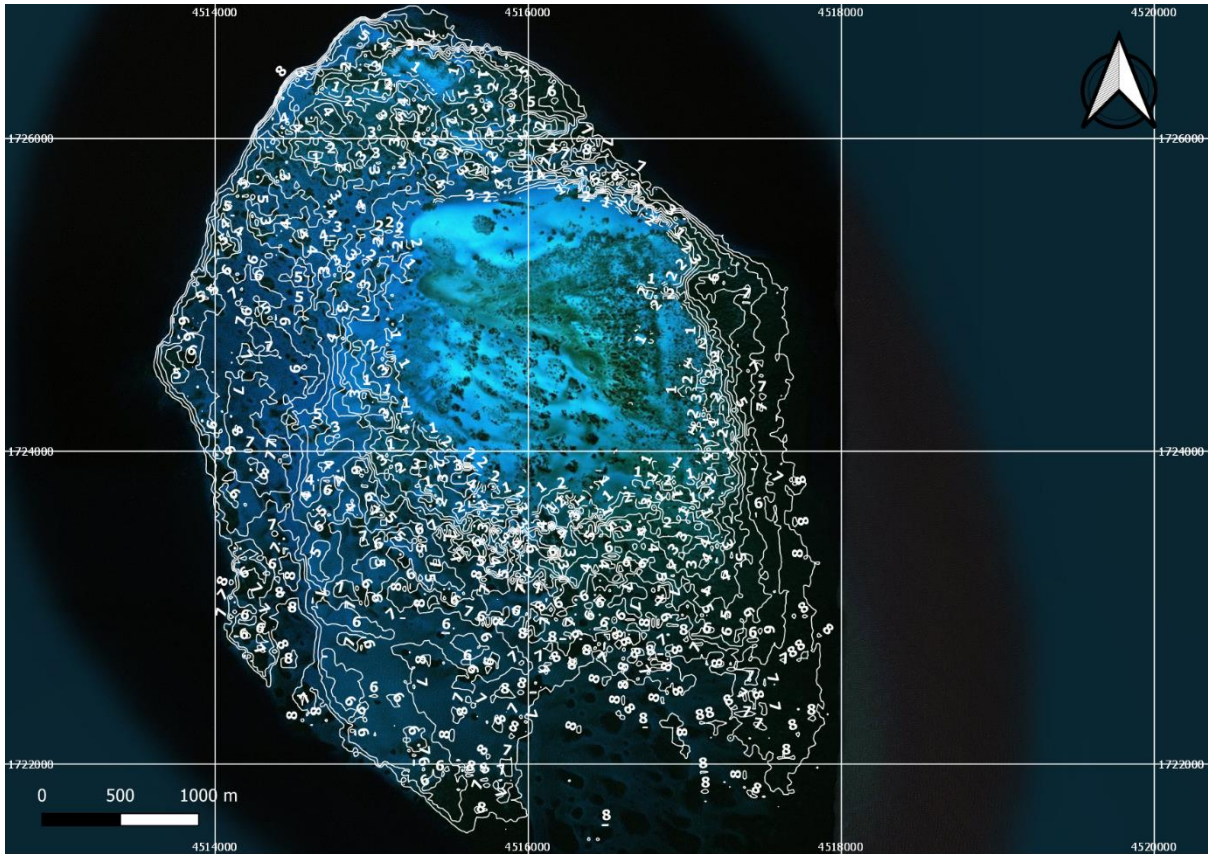


Figure24 : The SDB results at location C, set against the panchromatic Landsat 8 image. Although this location did not contain any in-situ datapoints measurements and it was close to the borders of the study area, the SDB was nonetheless able to correctly follow the shape of the islands. Several submerged structures, nearly invisible to the naked eye, were also successfully mapped.



Basemap: © ESRI

Figure25 : The SDB results at location D, around a submerged structure. The multitude of contours may indicate noise from turbulence or artifacts created by the sensor. It could also be the effects of clouds or dust particles covering this location.

Bab el-Mandab

The Bab el-Mandab straits study area at the entrance of the Red Sea has a 1:2 ratio of land to water as wet areas take about 30% of its pixels (Fig. 26). This area also contains a few islands, some at its north-west end and some close to the straits.

The SDB process in this study area had a collection of six Landsat 8 scenes for its imagery input (path 166, row 51 on the WRS-2 coordinate system), all having less than 0.1% of cloud coverage.

The in-situ dataset used for the calibration in this area was generated by John Hall and consisted of over 16,000 points, all of them inside the boundaries of the Landsat 8 scene used here.

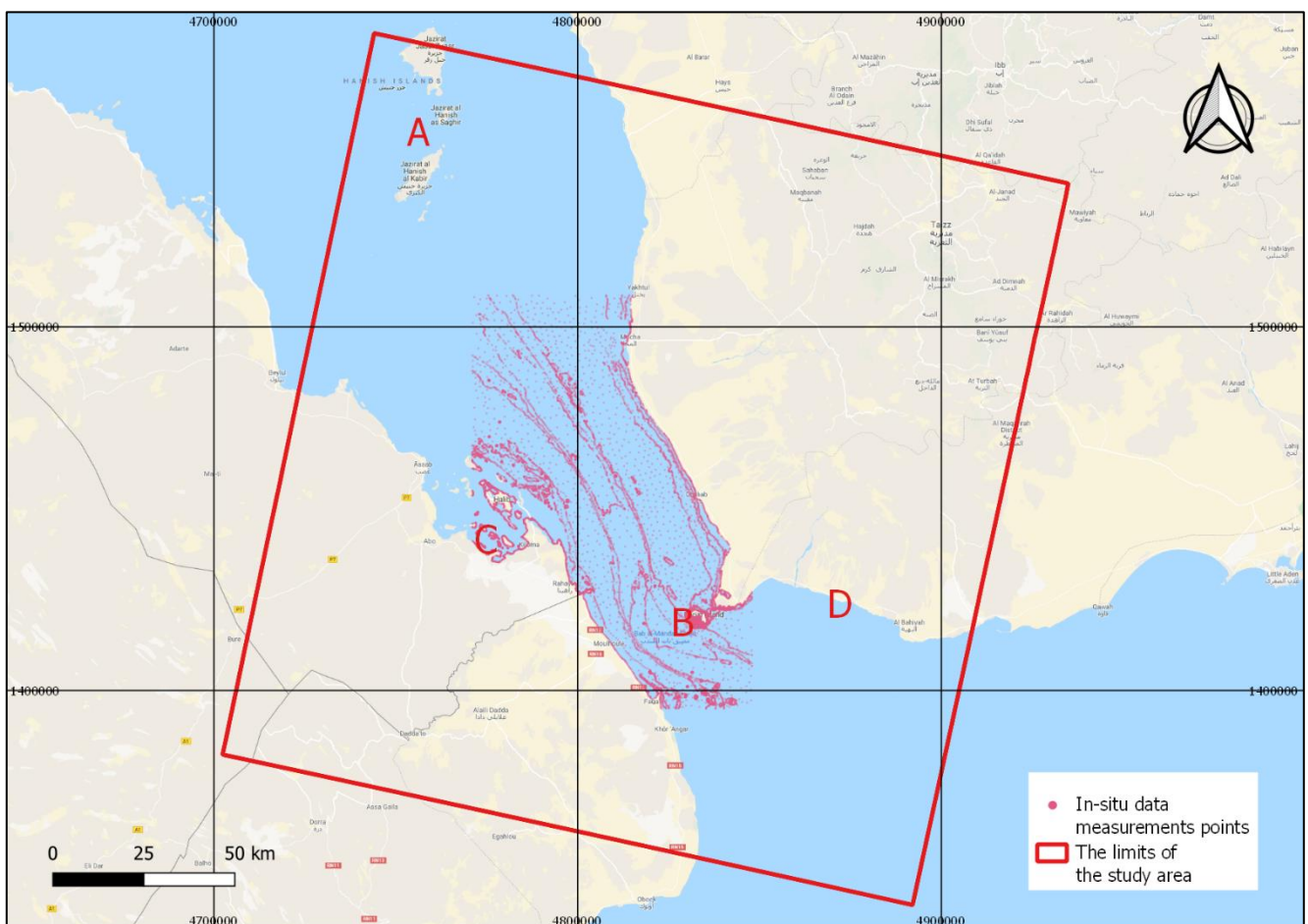


Figure 26 : An overview of the Bab el-Mandab straits at the entrance to the Red Sea. This study area has 30% water coverage with a few islands. The pink points are the in-situ measurements that were available for the calibration and the red rectangle represents the limits of the Landsat 8 scene used here. The letters A-D are the locations of the figures 30-33, respectively.

The separation of pixels into water and land classes using Otsu's method was successful. The threshold value was found to be at 10,699 DN (Fig. 27).

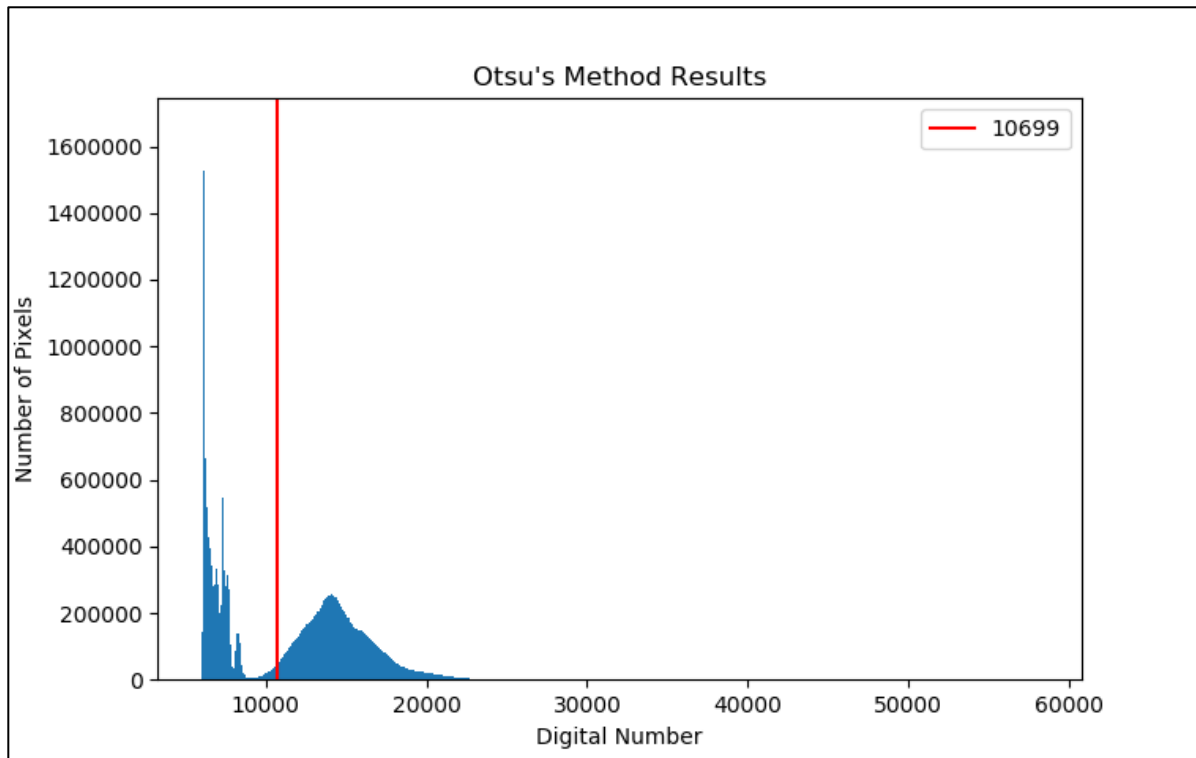


Figure 27 : The results of Otsu's method for thresholding implemented on the SWIR band at the Bab el-Mandab straits. This method was successful in splitting the pixels into the two separate classes of land and water with a thresholding value of 10,699 DN.

The scene which best fitted the in-situ dataset was taken on 17/05/2016. The linear regression had a maximum R^2 score of 0.69 at a depth of 15.8 m (Fig. 28). Similar R^2 scores are found up to depths of 20 m which was chosen as the depth of extinction with R^2 score of 0.669. Beyond the depth of extinction, the R^2 score drops, indicating that in these depths the linear model does not accurately correlate depths with the log-band ratio.

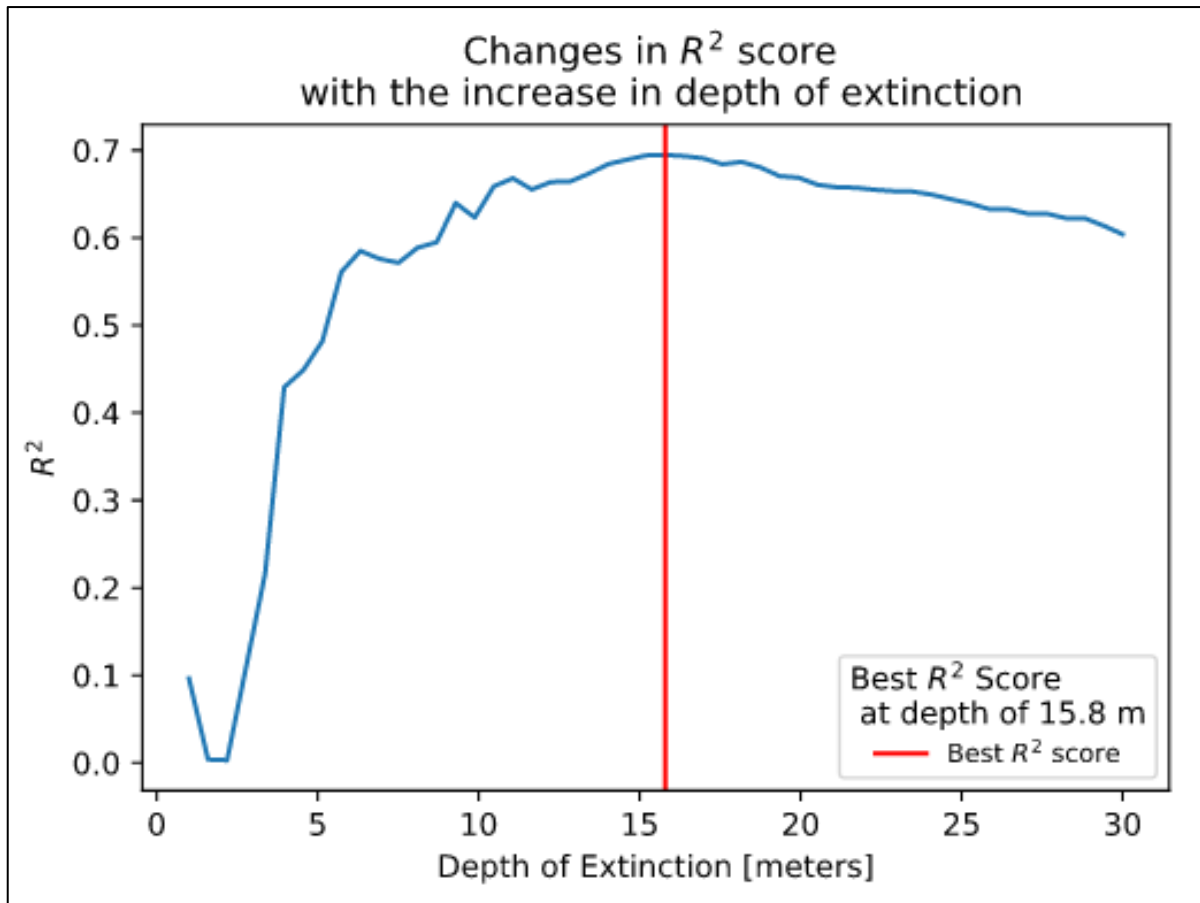


Figure 28 : An analysis of the changes in R² score with the increase of the depth of extinction. the best R² was found at 15.8 m, while depths of up to 20 m could also be used with a similar R² score.

In Fig. 29 we can see the results of the linear regression, both up to the depth of the best R² value and up to the depth of extinction. Out of the 16,000 in-situ data points available, roughly 10,600 (66%) data points were below the depth of extinction of 20 m and suitable for the linear regression calculation. In depths greater than the depth of extinction the model loses its ability to predict the water depth as the graph flattens at the log-band ratio of 1.020, indicating that this value signifies the light returning from the body of water and not from the bottom.

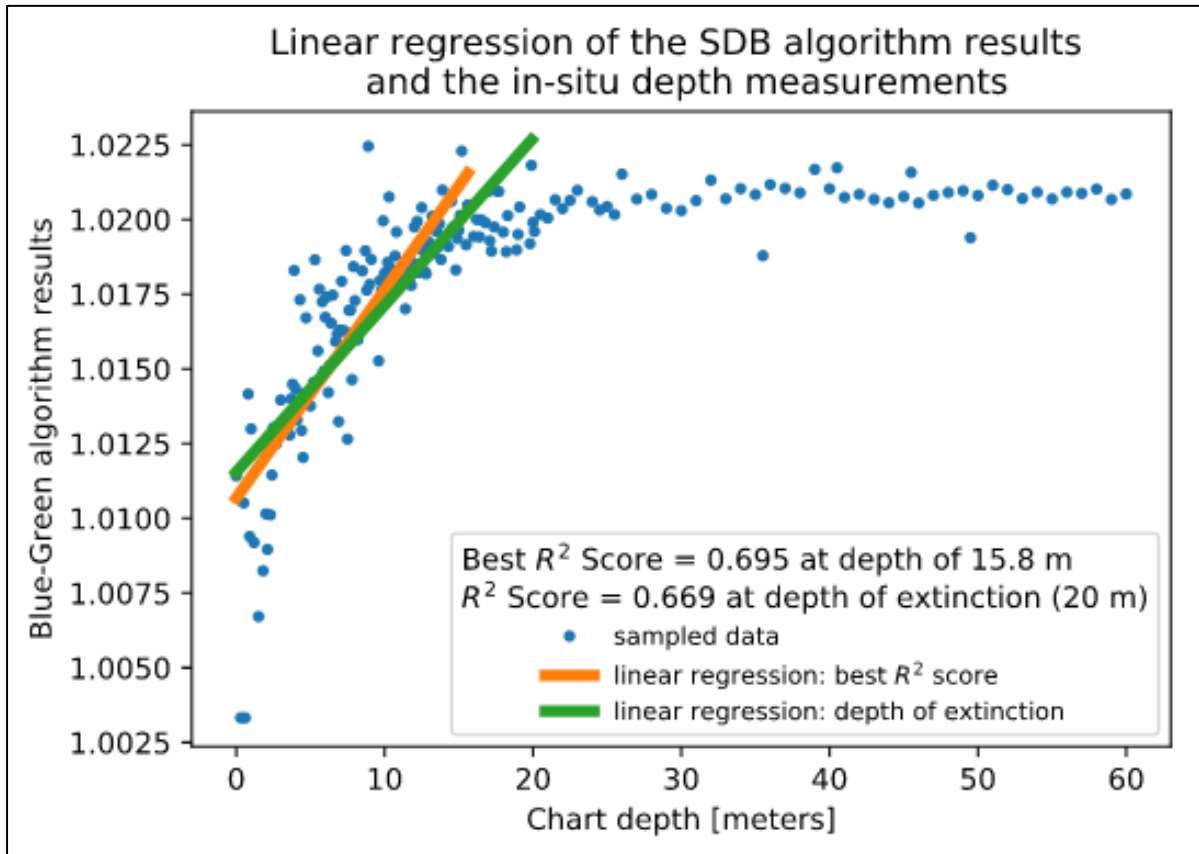
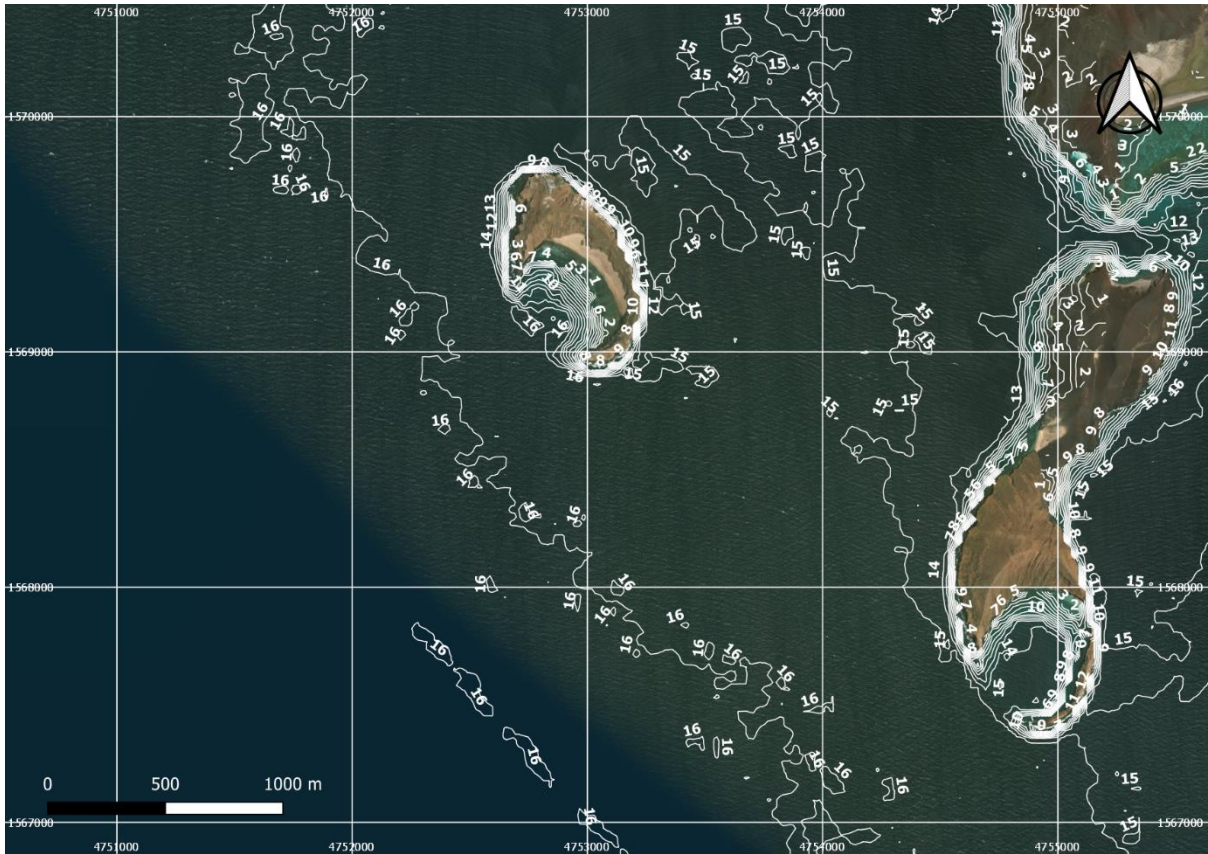


Figure29 : The linear regressions used in this study area, both up to the depth that has the highest R2 score and up to the depth of extinction. At the Blue-Green band ratio of 1.020 the graph flattens, indicating light reflecting from the body of water and not the bottom.

In the following figures, Figs. 30-33, we can see the results of the SDB layer at the study area. The Raster was transformed into contours of 1 m steps for the visual interpretation of the results. We can see that the contours tend to describe correctly the shape of the shorelines around the shoreline but there are several contours in the deeper water that seem to be inaccurate, as can be clearly seen in Figs. 32-33. These may be the results of unclear water or inconsistent in-situ measurements.



Basemap: © ESRI

Figure30 : The SDB results around the various islands at the north-west areas of the study area (location A in the overview map). We can see that the contours correctly follow the different shorelines, although it is unclear whether the contours south of islands really describe submerged structures or are artifacts from unclear waters



Basemap: © ESRI

Figure31 : The SDB results at location B, the Bab el-Mandab straits. Here the SDB contours follow the shorelines of both sides of the straits. Some contours that appear in the middle of the straits are probably an artifact from ships or clouds.



Figure32 : The SDB results at location C. The contours follow the shoreline and describe some submerged structures, although the high irregularity suggests that the SDB may be less accurate here.

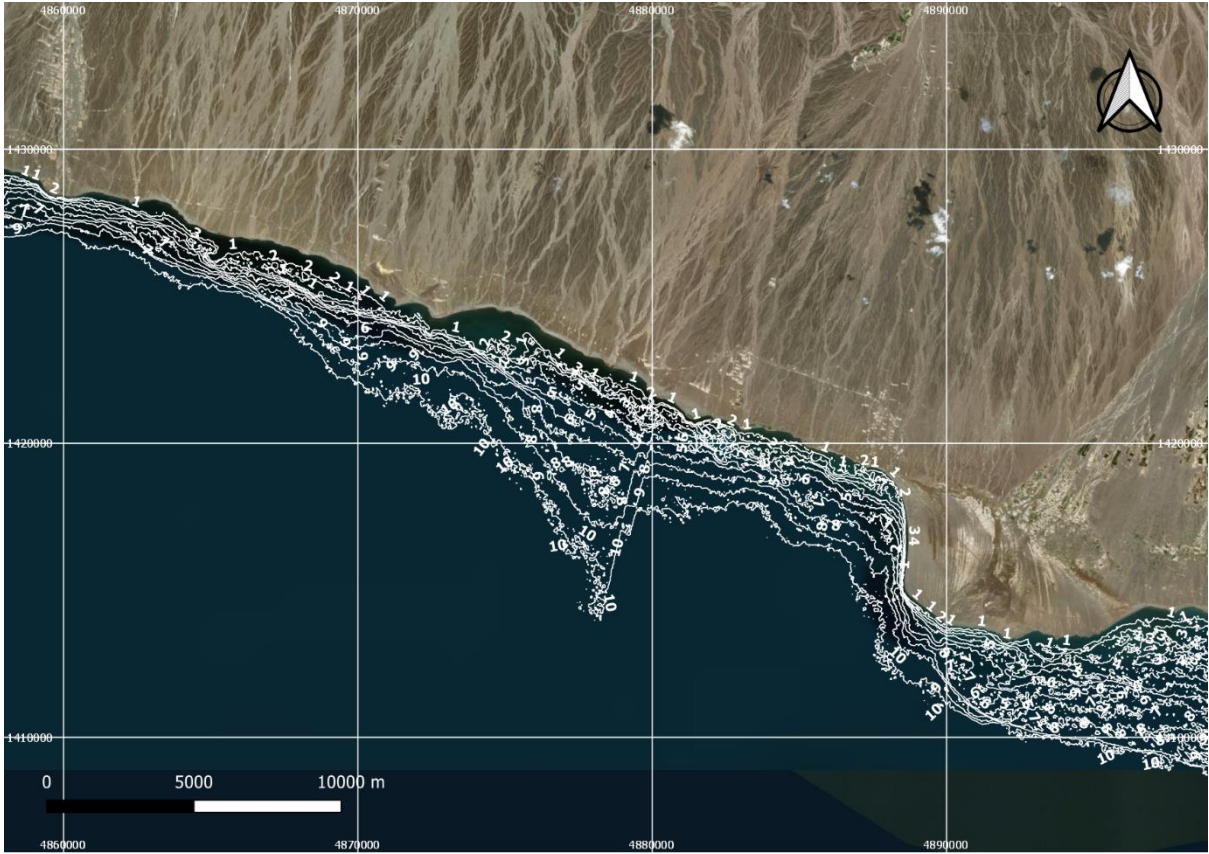


Figure33 : The SDB results at location D, following the shoreline. The contours that extrude into the water are an artifact deriving from unclear water or atmosphere.

Qatar

In the study area covering Bahrain and northern Qatar there are several submerged structures, as well as small islands and long shorelines (Fig. 34). The area covered by water takes about 65% of the total pixels.

The SDB process here had a collection of 23 Landsat 8 scenes for its imagery input (path 163, row 42 on the WRS-2 coordinate system), all having less than 0.03% of cloud coverage.

The in-situ dataset used for the calibration in this area was generated by John Hall and consisted of over 34,000 points, 33,000 of them were inside the boundaries of the Landsat 8 scene used here.

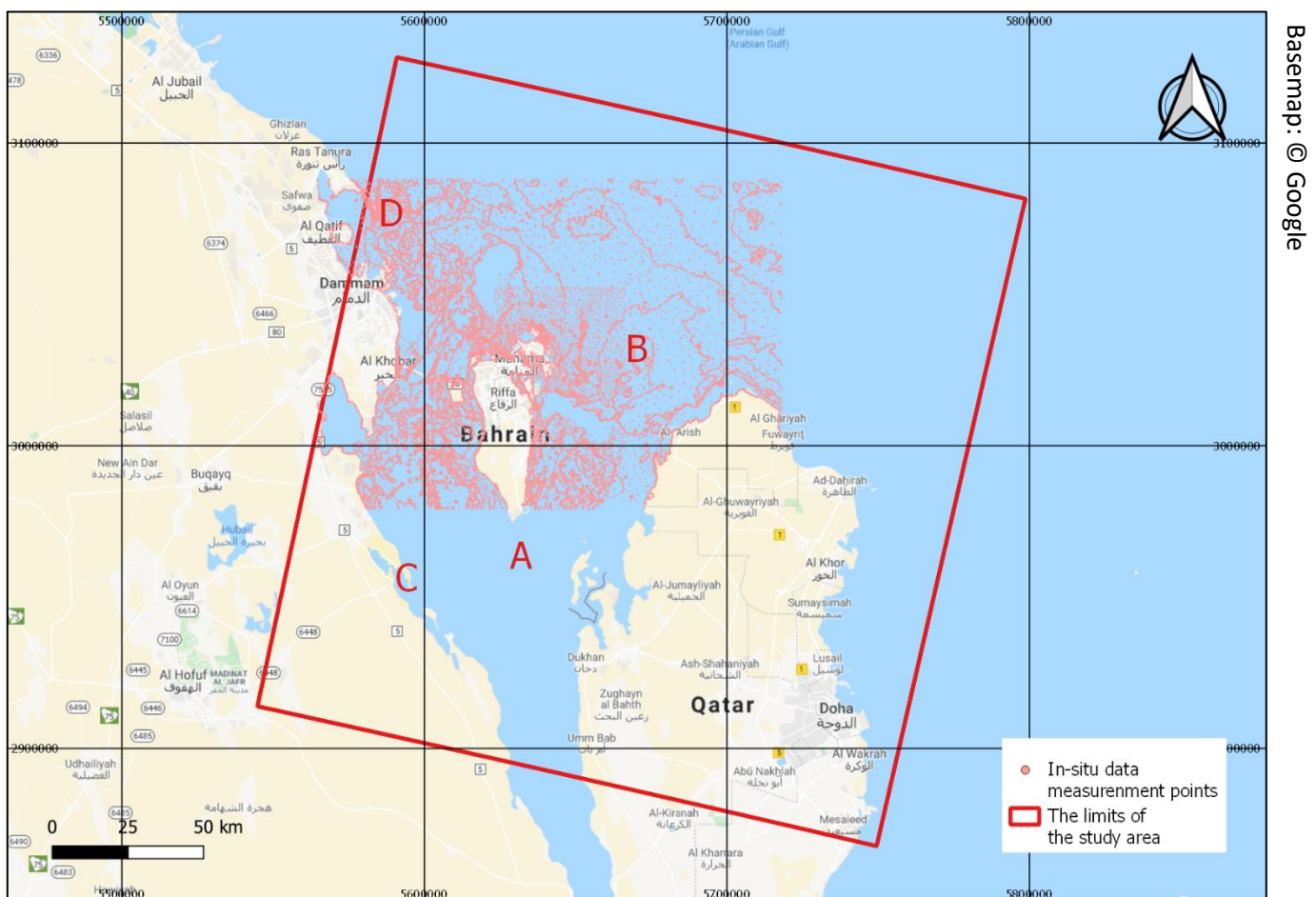


Figure 34 : An overview of the study area covering Bahrain and northern Qatar. This study area has 65% water coverage with a few islands and submerged structures. The pink points are the in-situ measurements that were available for the calibration and the red rectangle represents the limits of the Landsat 8 scene used here. The letters A-D are the locations of the figures 38-41, respectively.

The separation of pixels into water and land classes using Otsu's method was successful. The threshold value was found to be at 17,193 DN (Fig. 35).

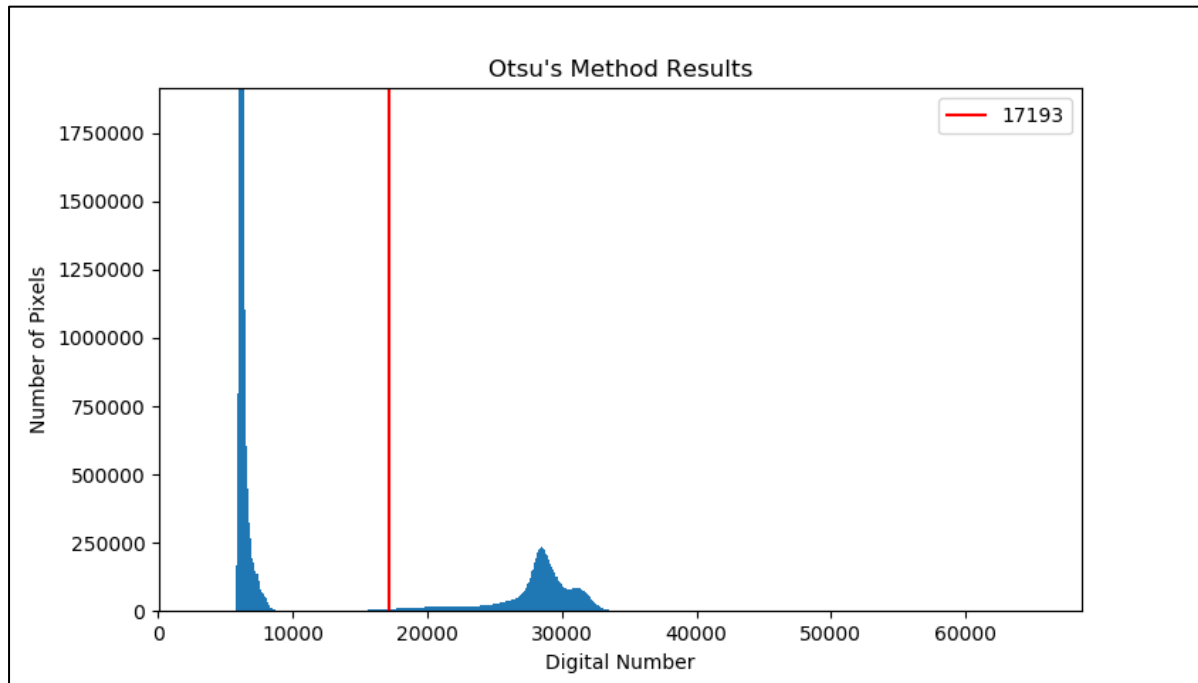


Figure 35 : The results of Otsu's method for thresholding implemented on the SWIR band near Qatar and Bahrain. This method was successful in splitting the pixels into the two separate classes of land and water with a thresholding value of 17,193 DN.

The scene which best fitted the in-situ dataset was taken on 09/09/2013. The linear regression had a maximum R^2 score of 0.859 at a depth of 11.1 m (Fig. 36). Similar R^2 scores are found up to depths of 15 m which was chosen as the depth of extinction with R^2 score of 0.821. Beyond the depth of extinction, the R^2 score drops, indicating that in these depths the linear model does not accurately correlate depths with the log-band ratio.

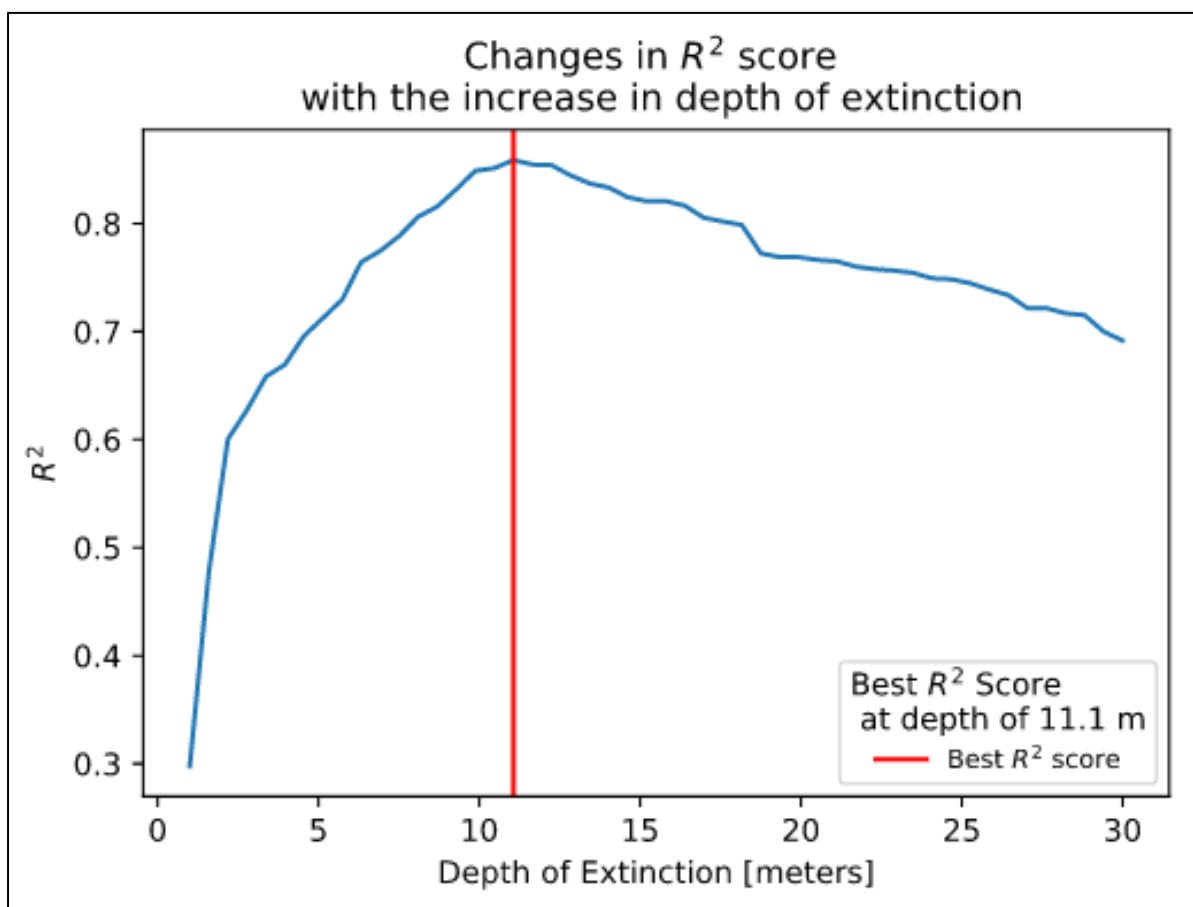


Figure36 : An analysis of the changes in R² score with the increase of the depth of extinction. the best R² was found at 11.1 m, while depths of up to 15 m could also be used with a similar R² score.

In Fig. 37 we can see the results of the linear regression, up to the depth of the best R² value and up to the depth of extinction. Out of the 33,000 in-situ data points available, roughly 31,000 (93%) data points were below the depth of extinction of 15 meters and suitable for the linear regression calculation. In depths greater than the depth of extinction the model loses its ability to predict the water depth as the graph flattens at the log-band ratio of 1.021, indicating that this value signifies the light returning from the body of water and not from the bottom.

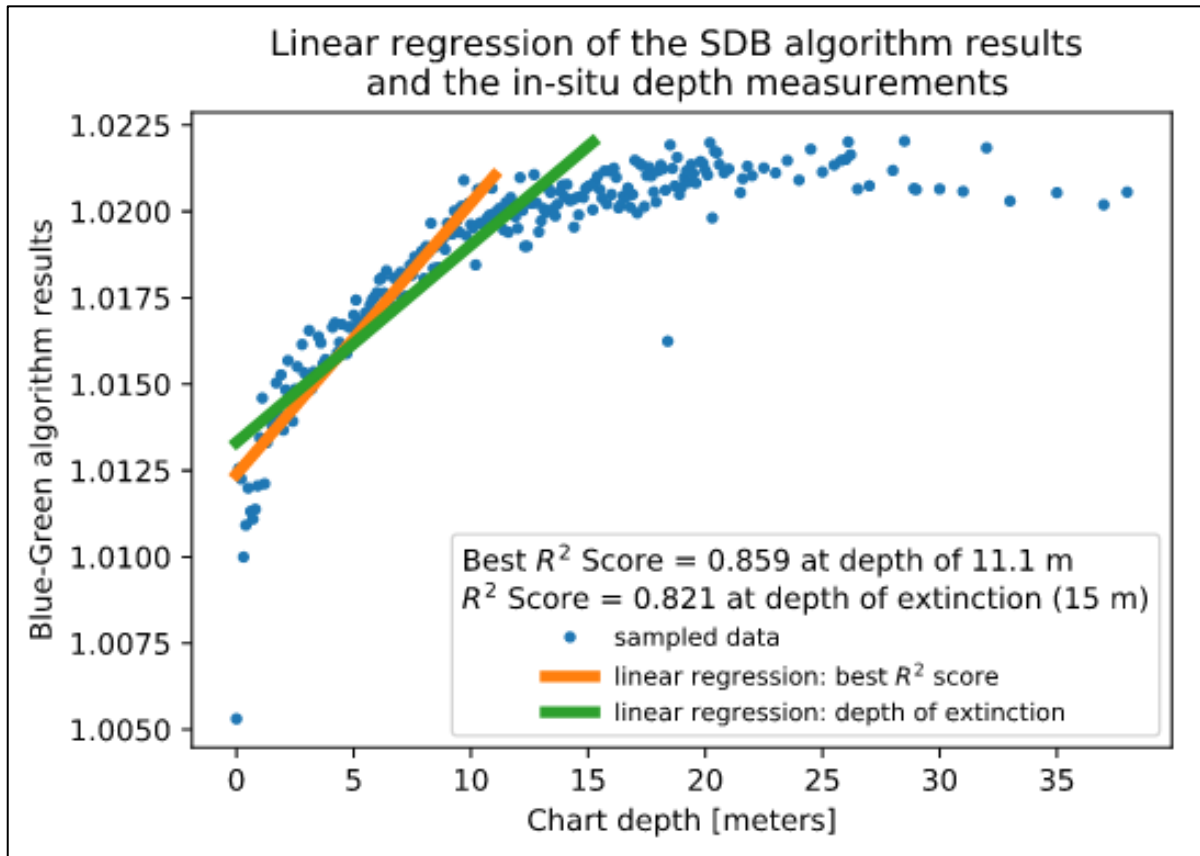


Figure37 : The linear regressions used in this study area, both up to the depth that has the highest R^2 score and up to the depth of extinction. At the Blue-Green band ratio of 1.021 the graph flattens, indicating light reflecting from the body of water and not the bottom.

In the following figures, 38-41, we can see the results of the SDB layer at the study area. The Raster was transformed into contours of 1 m steps for the visual interpretation of the results. We can see that the contours tend to describe correctly the shape of submerged structures, even those that are barely visible in a standard true color image (Fig. 38). The contours tend to follow the shorelines correctly but there seems to be a lot of noise in the deeper water, maybe due to turbulence or sediments. However, the contours in Fig. 41 were generated in an area which had over 5,000 in-situ measurement points and it is possible that they describe the bathymetry accurately.



Basemap: © ESRI

Figure38 : The SDB results around the various submerged structures south of Bahrain (location A in the overview map). These structures are barely visible to the naked eye, but the algorithm successfully identifies them.

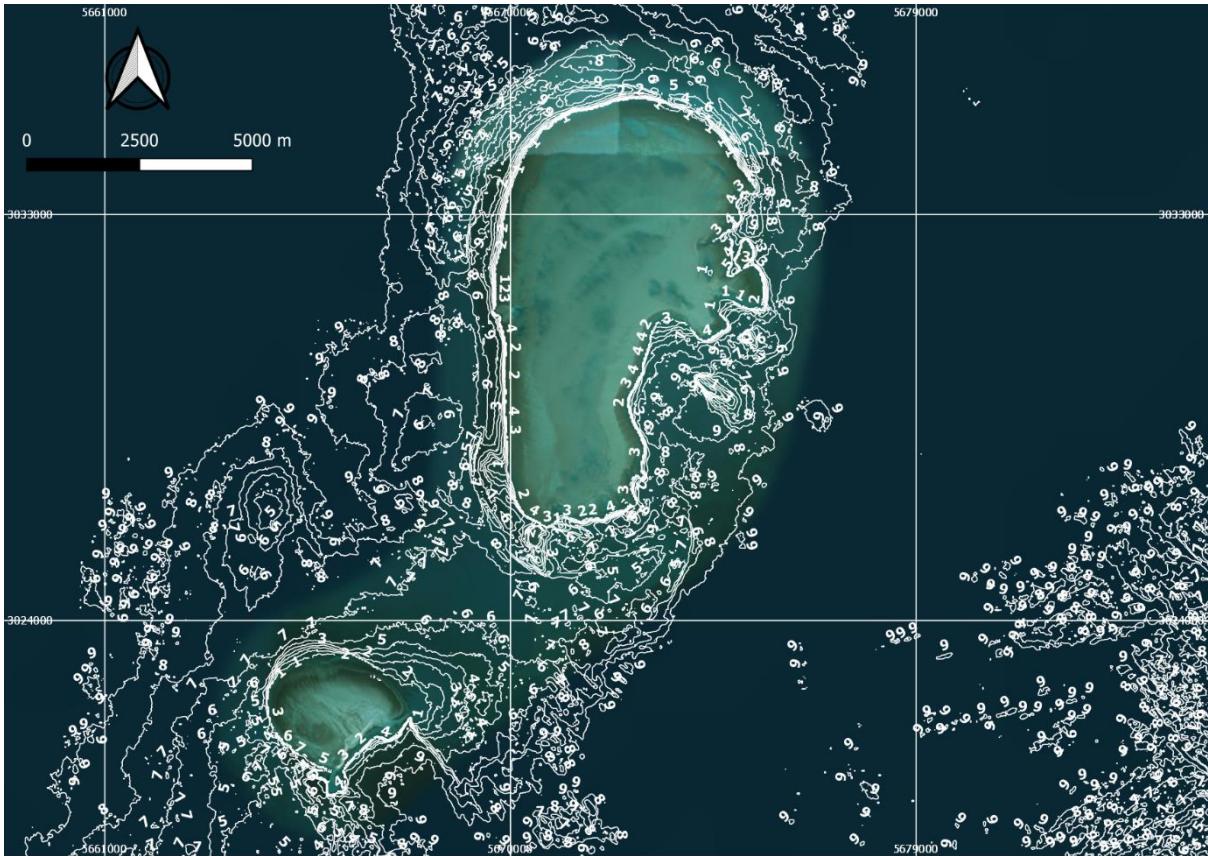


Figure39 : The SDB results at location B, between Qatar and Bahrain. Two large submerged structures were found by the SDB algorithm and the contours follow their outline. At the south-east corner of this figure we can see many irregular contours, indicating unclear water or atmosphere.

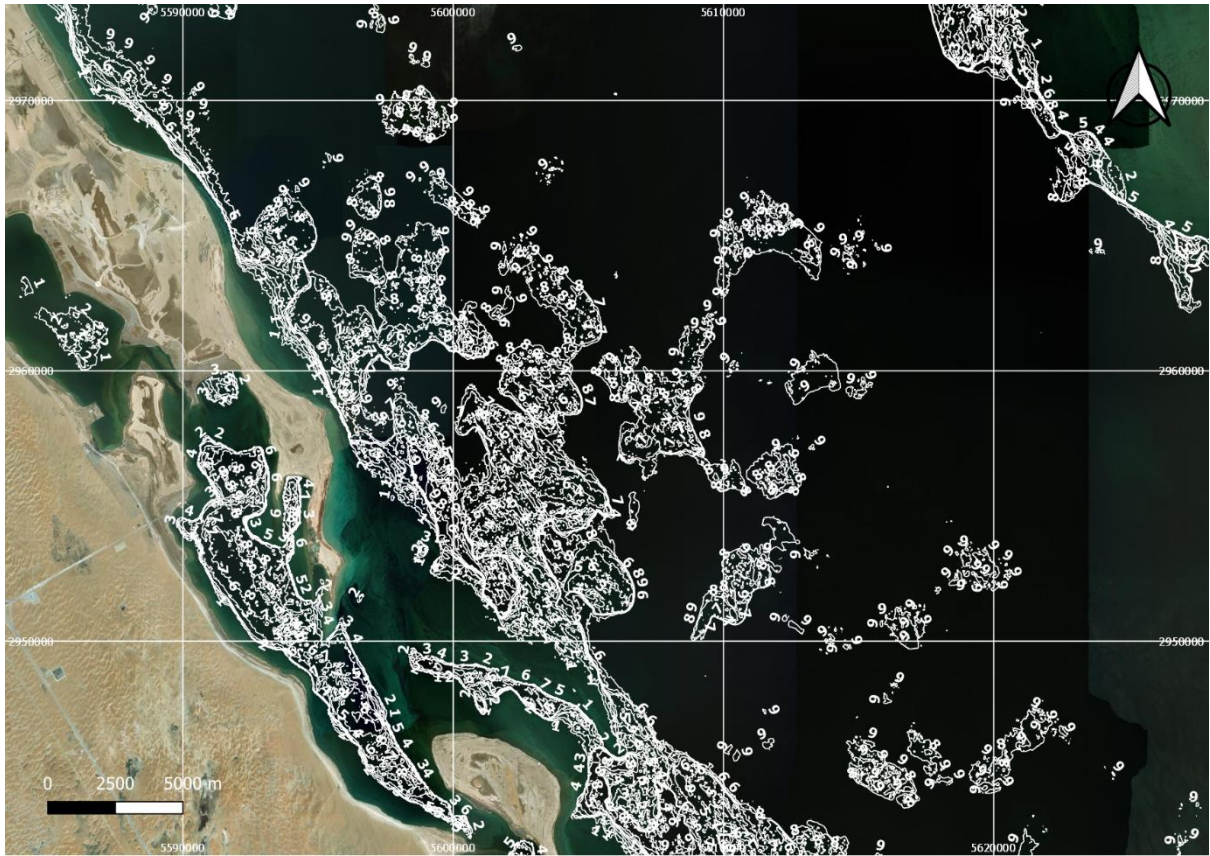


Figure40 : The SDB results at location C, offshore Saudi Arabia. The contours follow the shoreline and the inlets as well as describing some submerged structures that are not visible otherwise.



Figure41 : The SDB results at location D, near King Abdulaziz seaport. This area has a large density of in-situ data points, strengthening the accuracy of the algorithm.

Stage 2, part B: Calibrating by Tidal Data

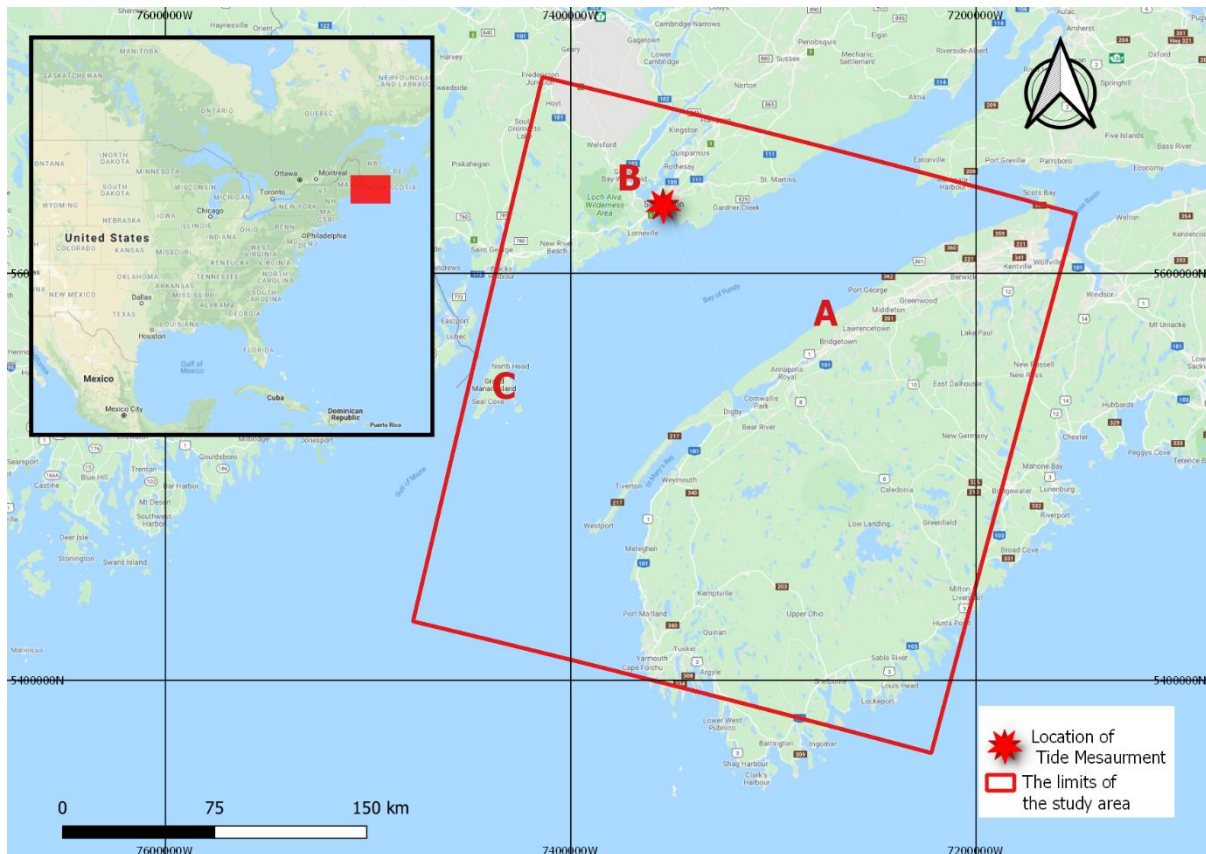
In this part of the study I tested a new method for calibrating the SDB in areas lacking in-situ data, relying on tidal data instead. I used the same SDB script as in Stage 2, part A for downloading the relevant spectral bands, separating land and water with Otsu's method for thresholding, image processing and calculating the log-band ratio. This process differs from part A in determining the best scene as it was pre-selected to fit a certain acquisition date and not automatically selected from the available Landsat 8 archive. The section of the script that followed the log-band ratio, i.e., the sampling and linear regression fitting was changed to a new work protocol.

This new method was tested on two study areas, at the bay of Fundy in eastern Canada and near Broome in western Australia (Figs. 42 and 50, respectively). These areas were selected as they have a large tidal amplitude and a reliable, governmental source for past tidal measurements.

The Bay of Fundy, Canada

This study area, covered by the Landsat 8 scene of path 9, row 29 (the WRS-2 coordinate system) is located at the bay of Fundy in eastern Canada (Fig. 42). In the port of Saint John is located the buoy by which the Canadian government regularly measures the tides in the bay. The tide data is published and made publicly available through the Fisheries and Oceans Canada website.

The tidal events that were used in this study were the low tide of 27/03/2019 at 14:49 (UTC), reaching a minimum of 1.4 m and the high tide of 02/08/2019 at 16:24 (UTC) reaching a maximum of 8.2 m. For each of these dates a corresponding Landsat 8 scene was selected that had an acquisition time close to those events – an hour before and after the high and low tide, respectively. Both of the scenes had less than 0.5% cloud coverage.



Basemap: © Google

Figure42 : The study area at the bay of Fundy, Canada. The red rectangle represents the boundaries of the Landsat 8 scene and the red star is the location of the buoy near Saint John that is used for tidal measurements. The letters A-C are the locations of the SDB result figures 47-49, respectively.

SDB algorithm calculation

Both scenes, representing high and low tide, went through image processing and land/water separation using Otsu's method for thresholding (Fig. 43). While we would expect that during high tides the number of water pixels will be higher than their low tide equivalence, there were 55% water coverage in low tide and 47% water coverage in high tide. This may be due to the seasonal changes as the low tide

image was acquired at the wet season while the high tide image was acquired at the summer.

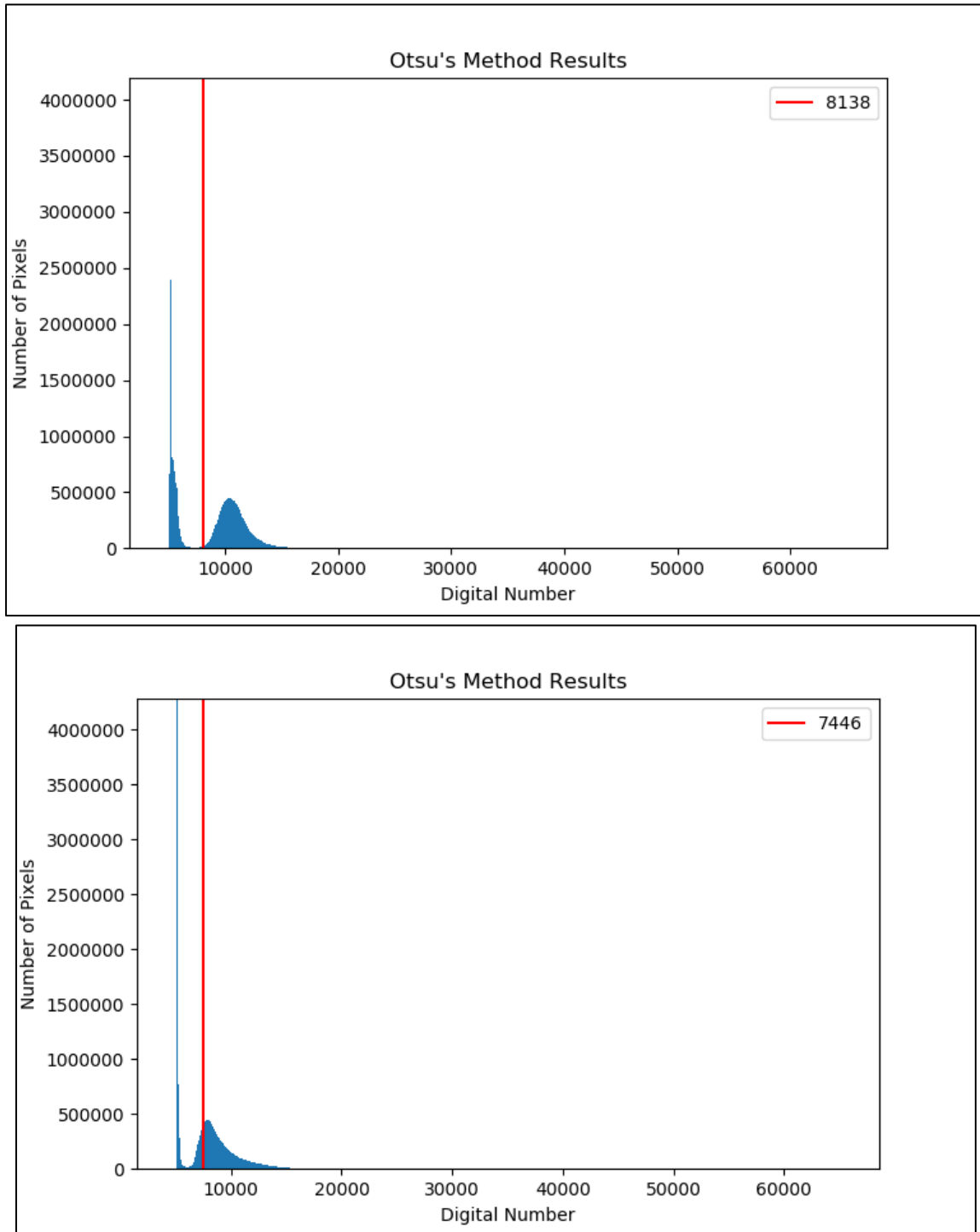
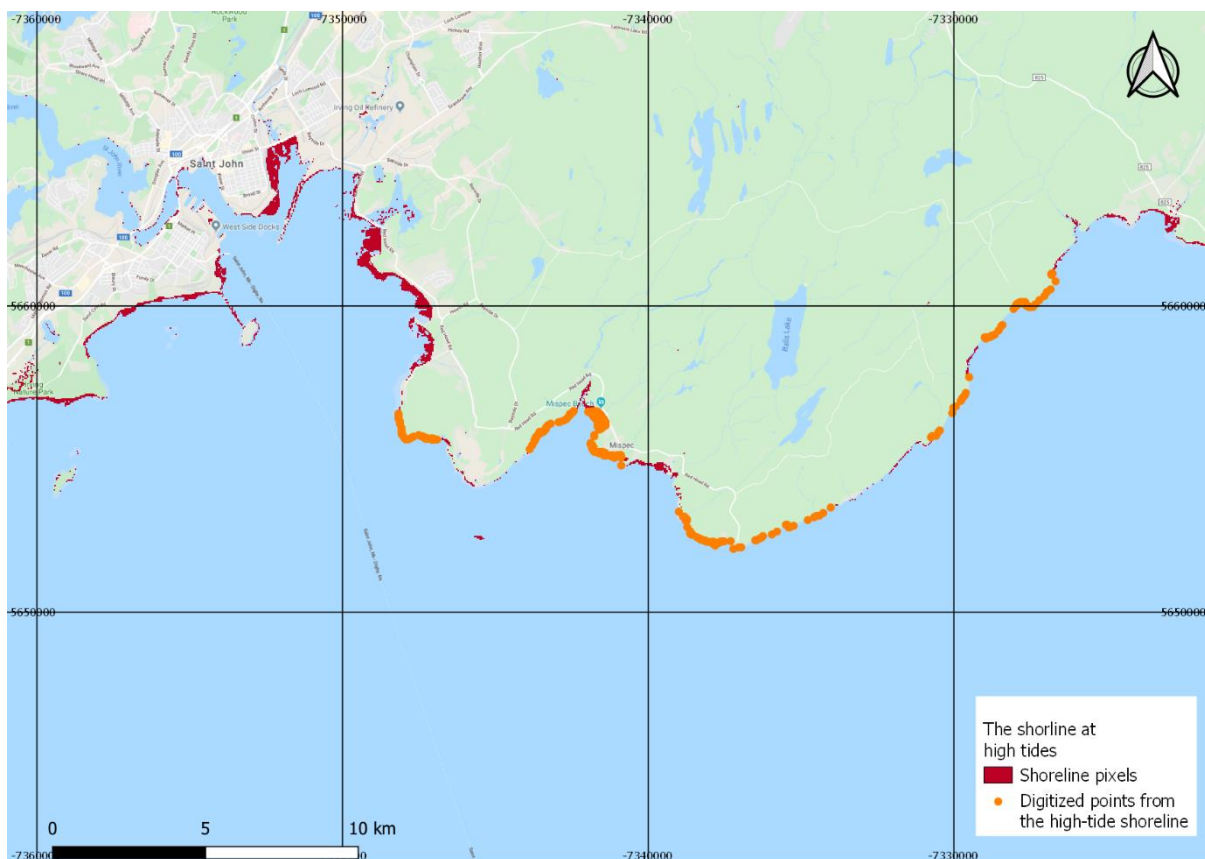


Figure43 : The results of Otsu's method for thresholding implemented on the SWIR bands at the bay of Fundy. The figure above is at high tide and the figure below is at low tide.

Gathering data points for calibration

The location of the buoy (Fig. 42) provides a fixed location with known depths, as at low tide the depth was 1.4 m and at high tide the depth was 8.2 m. Using the results of the quotient of the log-band, I subtracted the areas covered with water at low tide from their high tide equivalence, resulting in areas that represent the shoreline during high tide (Fig. 44). These areas were assumed to have a depth of 1 m. After selecting from these pixels the areas which seemed to best describe the shoreline, I sampled them and generated a table of their values.



Basemap: © Google

Figure44 : The shoreline at high tide. The red areas are dry during low tide and covered with water at high tide. I assumed that they had a depth of 1 m during high tide. Out of those areas I digitized some as datapoints for the calibration.

Calibration

By digitizing the points of the shoreline at high tide I generated a datapoint table of 2,900 points: A single point with the depth value of 8.2 m and the rest with a uniform depth of 1 m. These points were used for the linear regression whose parameters were the basis of the calibration. Since the depth points sampled at the shoreline had a large range of values (Fig. 45) the mean value of them (1.013) was chosen as the input. This may affect the outcome of the SDB and maybe different methods for reducing this range (choosing the pixels with higher occurrence, for example) could have better results.

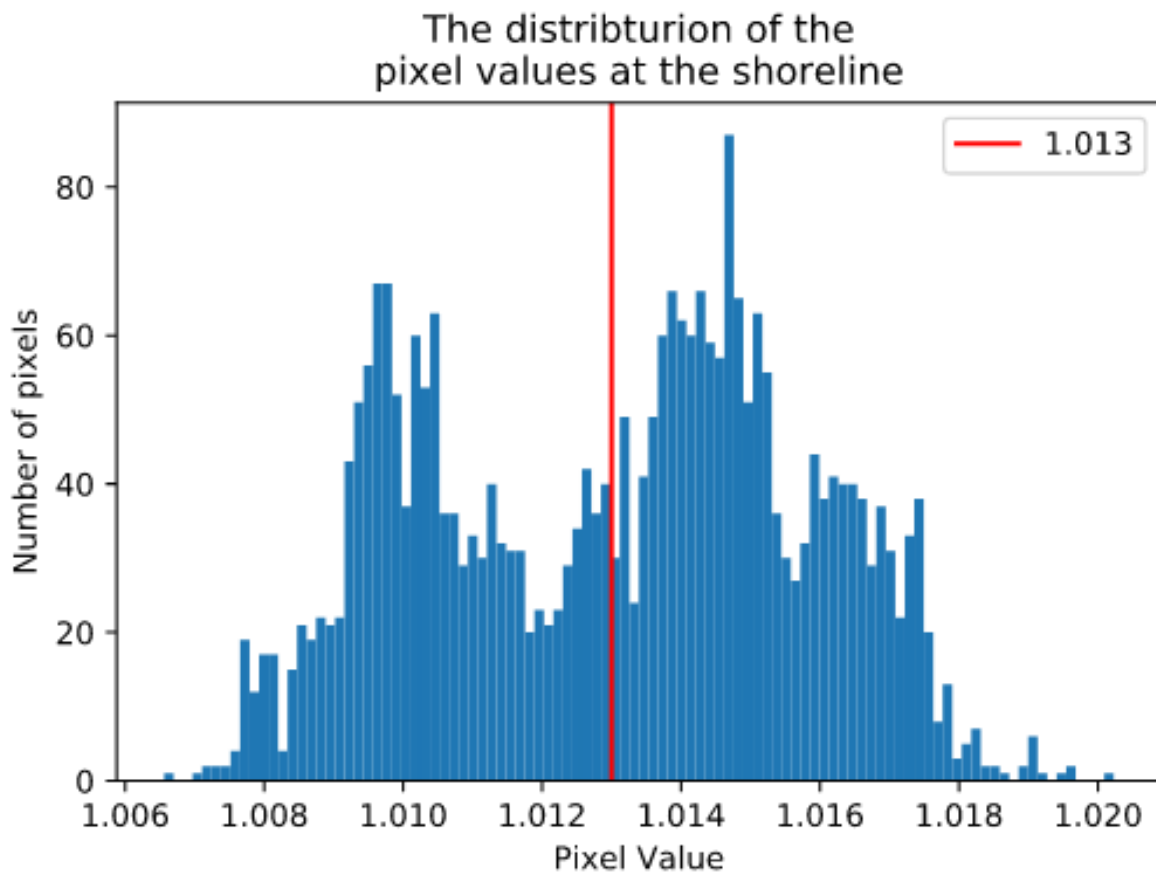


Figure45 : The distribution of the pixel values at the shoreline. The mean value was at 1.013.

The linear regression was applied to two points: one point at the buoy with depth of 8.2 m and the other at the mean value of the shoreline with depth of 1 m (Fig. 46). Since the linear regression was between two points, there was no advantage in trying different, more robust regression methods.

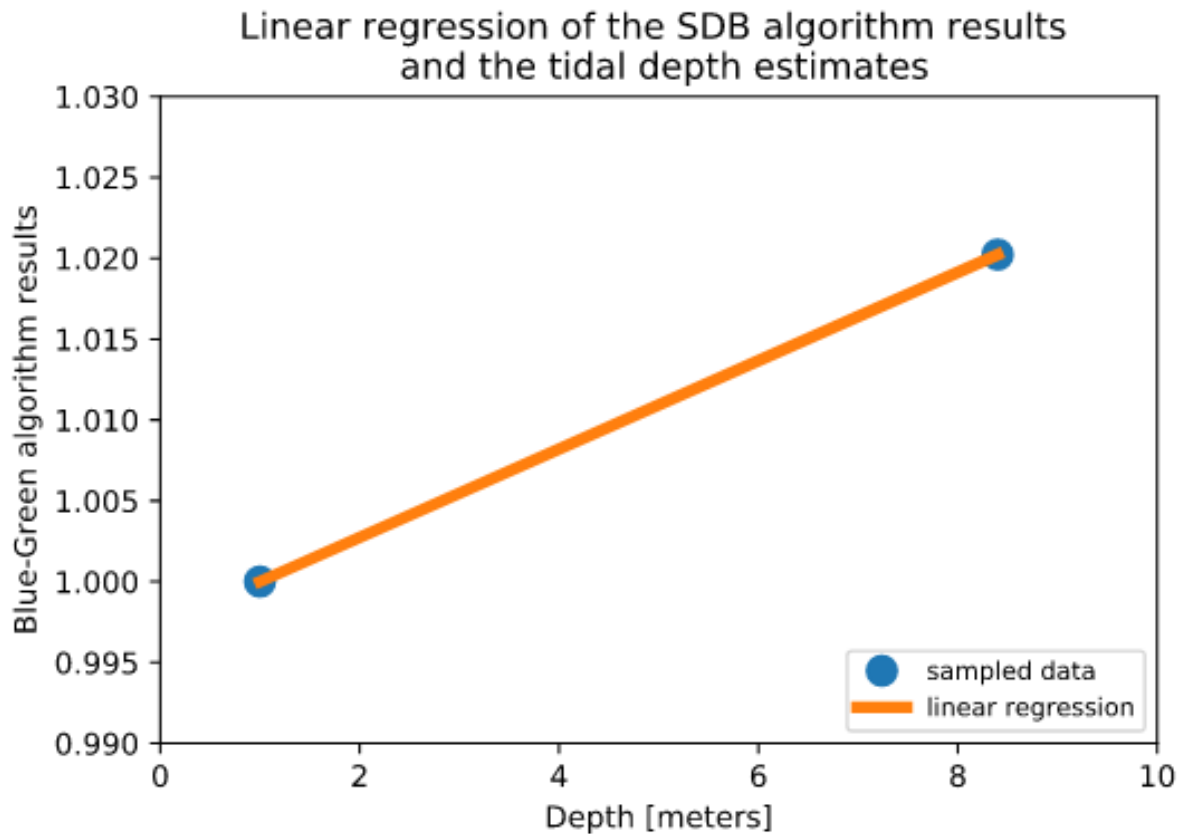


Figure46 : The results of the linear regression between the tidal depth estimations and the log-band ratio of the high tide imagery.

After I calculated the coefficients of this linear regression and applied them to the log-band ration array generated at the high tide, I subtracted from the resulting array the depth at the buoy of the low tide, thus receiving an array which represents the mean depths, i.e. the depths between high and low tide. This array was saved as the SDB GeoTIFF for the study area and transformed into contours.

SDB results

The SDB seems to describe well the shapes of the shorelines around the study area (Fig. 47). Inside the canal near Saint John (Fig 48), where the measurements buoy is located, the depths match the mean depth, as expected. The depths become deeper at the exit of the canal, although without having more data their accuracy cannot be determined. There are several contours in the deeper water which seems to be less accurate (Fig 49). They may be a result of unclear water or atmosphere as well as representing the limits of the linear regression used here.

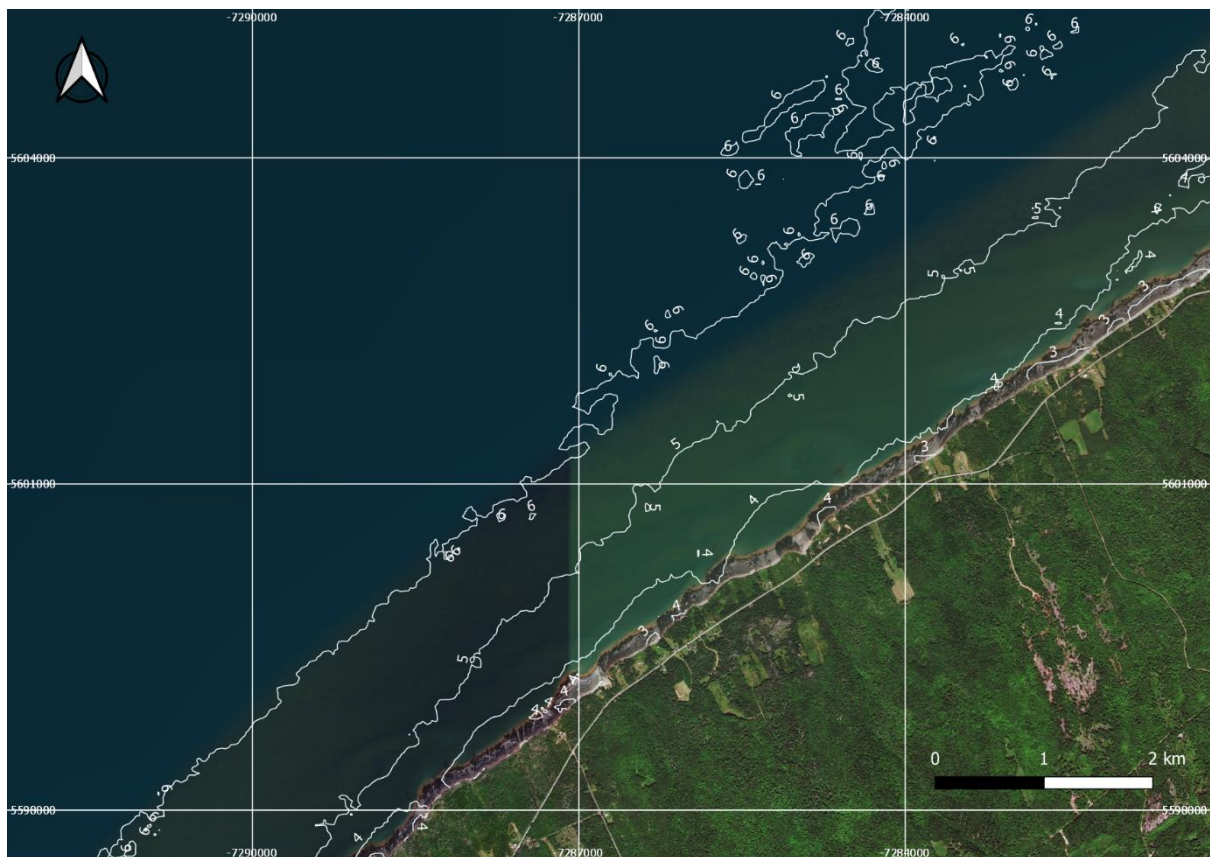


Figure47 : The results of the SDB at the south of the study area: the contours seem to correctly describe the shape of the shoreline.



Figure48 : The results of the SDB at Saint John, close to the buoy (appears as a red star). The depths around the buoy are close to 6 m – matching the measurements. The depths at the rest of the canal are mainly 5 m, returning to 6 m and deeper at its exit.

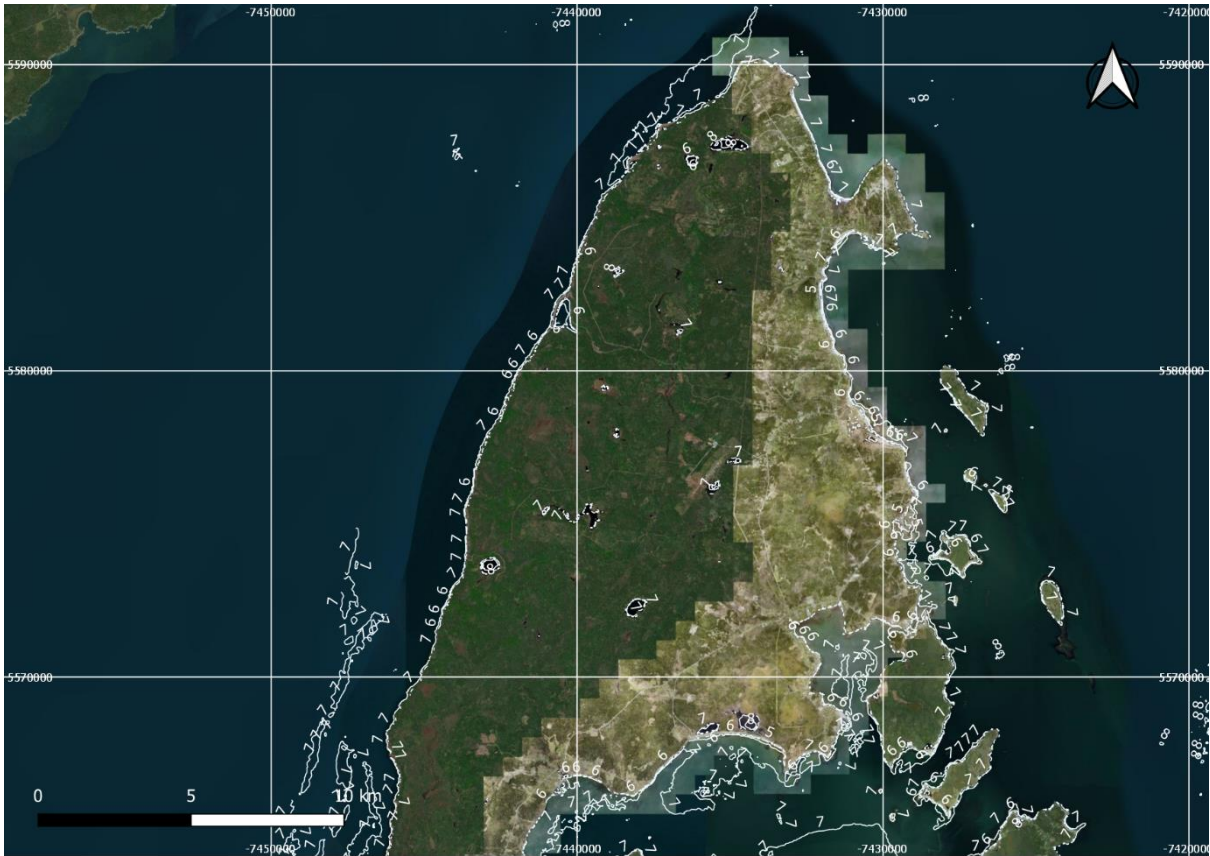


Figure49 : The results of the SDB at the west of the study area. While the contours follow well the shoreline, there are some contours in the deeper water that probably do not match the real depths. They may be the results of unclear water or the calibration data.

Broome, Australia

This study area, covered by the Landsat 8 scene of path 111, row 72 (the WRS-2 coordinate system) is located close to the city of Broome in western Australia. (Fig. 50). The buoy by which the Australian government regularly measures the tides in this area is placed near the Broome wharf. The tidal data is published and made publicly available through the Australian Bureau of Meteorology website.

The tidal events that were used in this study were the low tide of 03/04/2018 at 22:55 (UTC), reaching a minimum of 1.31 m and the high tide of 13/08/2019 at 01:36 (UTC) reaching a maximum of 7.52 m. For each of these dates a corresponding Landsat 8 scene was selected that had a close acquisition time. Both scenes had less than 0.1% cloud coverage.

Most of this study area is covered by deep water, meaning that the SDB here was be relevant mostly for the shorelines and the inlets, as well as for the Lacepede islands (Fig 56).

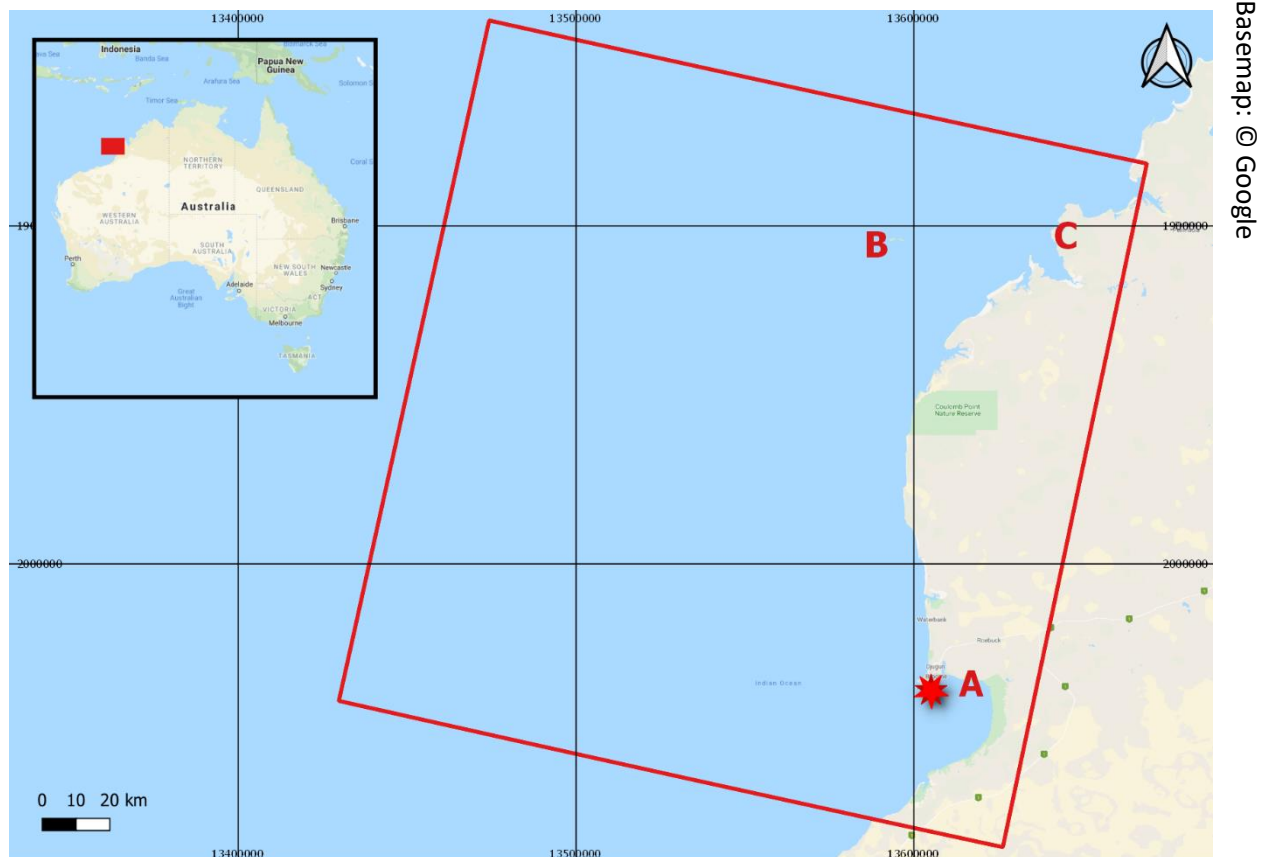


Figure 50 : The study area at the bay of Fundy, Canada. The red rectangle represents the boundaries of the Landsat 8 scene and the red star is the location of the buoy near Saint John that is used for tidal measurements. The letters A-C are the locations of the SDB result figures 55-57, respectively.

SDB algorithm calculation

Both scenes, high and low tide, went through image processing and land/water separation using Otsu's method for thresholding (Fig. 51). In both scenes the water takes about 84% of the total pixels, with 1% increase during high tide. This may be the result of the water covering more of the shore during high tide.

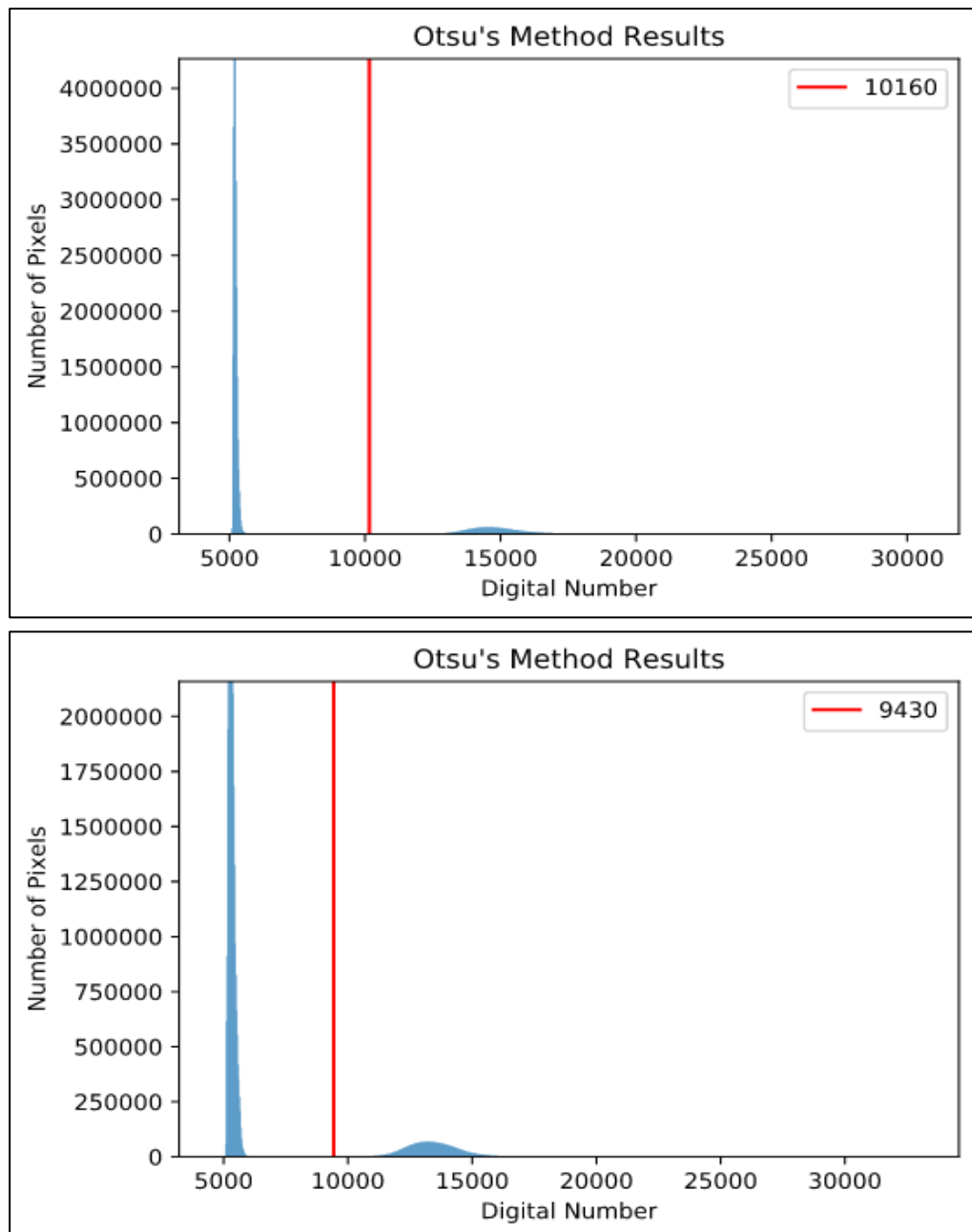
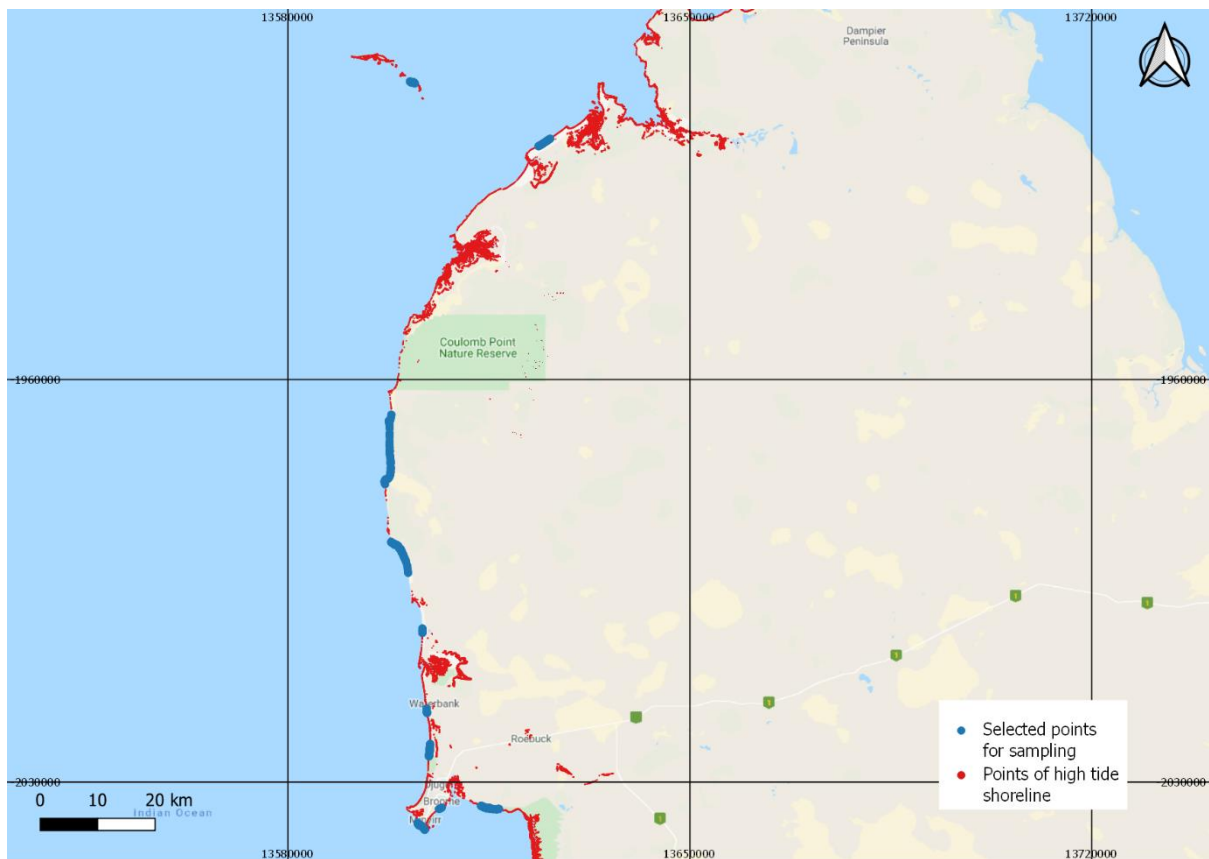


Figure 51 : The results of Otsu's method for thresholding implemented on the SWIR bands near Broome. The figure above is at high tide and the figure below is at low tide.

Gathering data points for calibration

The location of the buoy (Fig. 50) provides a fixed location with known depths, as at low tide the depth is 1.31 m and at high tide the depth is 7.52 m. Using the results of the quotient of the log-band, I subtracted the areas covered with water at low tide from their high tide equivalence, resulting in areas that represent the shoreline during high tide (Fig. 52). These areas were assumed to have a depth of 1 m. After selecting from these pixels the areas which seemed to best describe the shoreline, I sampled them and generated a table with their values.



Basemap: © Google

Figure52 : The shoreline at high tide. The red areas are dry during low tide and covered with water at high tide. I assumed that they had a depth of 1 m during high tide. Out of those areas I digitized some as datapoints for the calibration – marked as blue points.

Calibration

By digitizing the points of the shoreline at high tide I generated a datapoint table of 770 points: A single point with the depth value of 7.52 m and the rest with a uniform depth of 1 m. These points were used for the linear regression whose parameters were the basis of the calibration. Since the depth points sampled at the shoreline had a large range of values (Fig. 53) the mean value of them (1.002) was chosen as the input. This may affect the outcome of the SDB and maybe different methods for reducing this range (choosing the pixels with higher occurrence, for example) could have better results.

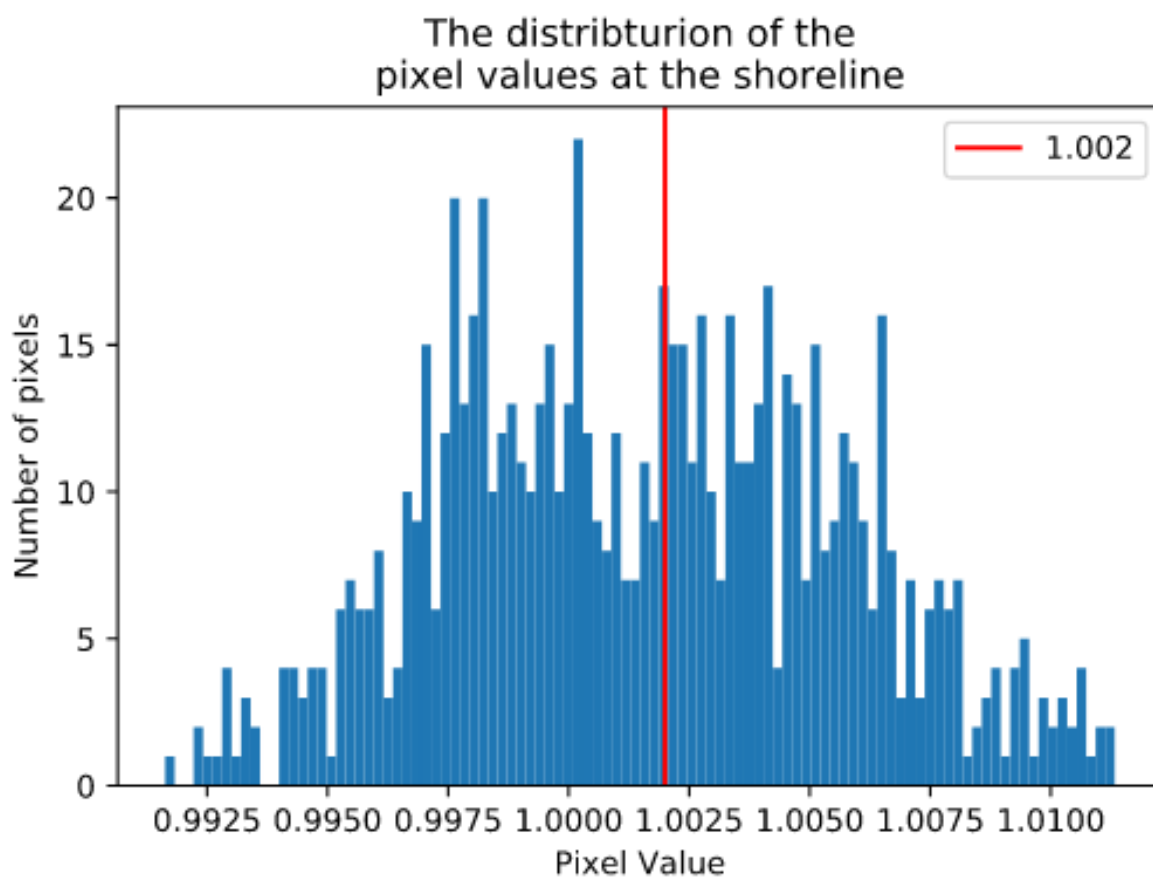


Figure53 : The distribution of the pixel values at the shoreline. The mean value was at 1.013.

The linear regression was applied to two points: one point at the buoy with depth of 7.52 m and the other at the mean value of the shoreline with depth of 1 m (Fig. 54). Since the linear regression was between two points, there was no advantage in trying different, more robust regression methods.

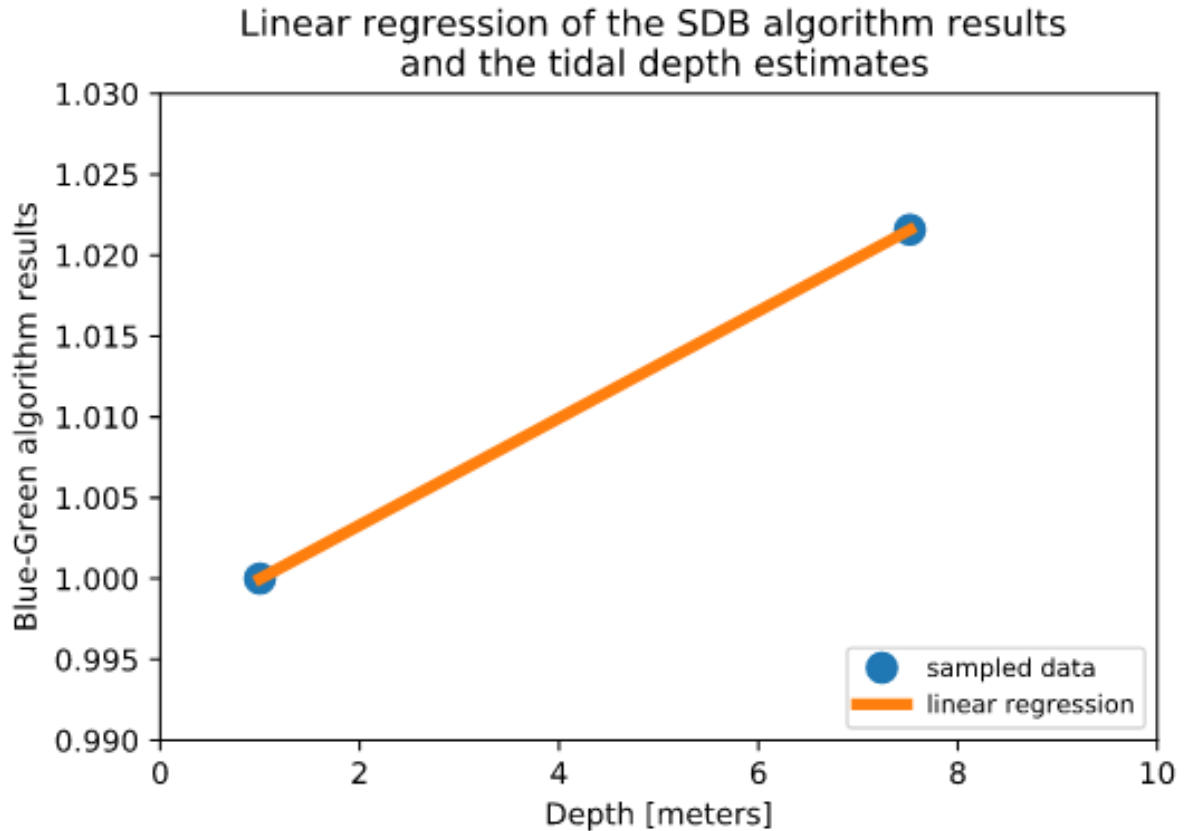


Figure54 : The results of the linear regression between the tidal depth estimations and the log-band ratio of the high tide imagery.

After I calculated the coefficients of this linear regression and applied them to the log-band ratio array generated at the high tide, I subtracted from the resulting array the depth at the buoy of the low tide, thus receiving an array which represents the mean depths, i.e. the depths between high and low tide. This array was saved as the SDB GeoTIFF for the study area and transformed into contours.

SDB results

The SDB seems to describe well the shapes of the shorelines around the study area (Fig. 55) Near Broome, close to the buoy where the measurements took place, the depths match the mean tidal depth, as expected. The depths become deeper at the open sea and the contours end there as we pass the depth of extinction. There are several contours in the deeper water which seems to be less accurate (Fig. 56), although the shape of the shorelines and the submerged structures around the Lacepede islands seem to have an accurate shape. The contours at Fig. 57 seem to be less accurate as the depth increases. This may be a result of unclear water or atmosphere as well as representing the limits of the linear regression used here.



Basemap: © ESRI

Figure55 : The results of the SDB near the measurements buoy (appears as a red star): the contours seems to correctly describe the shape of the shoreline.

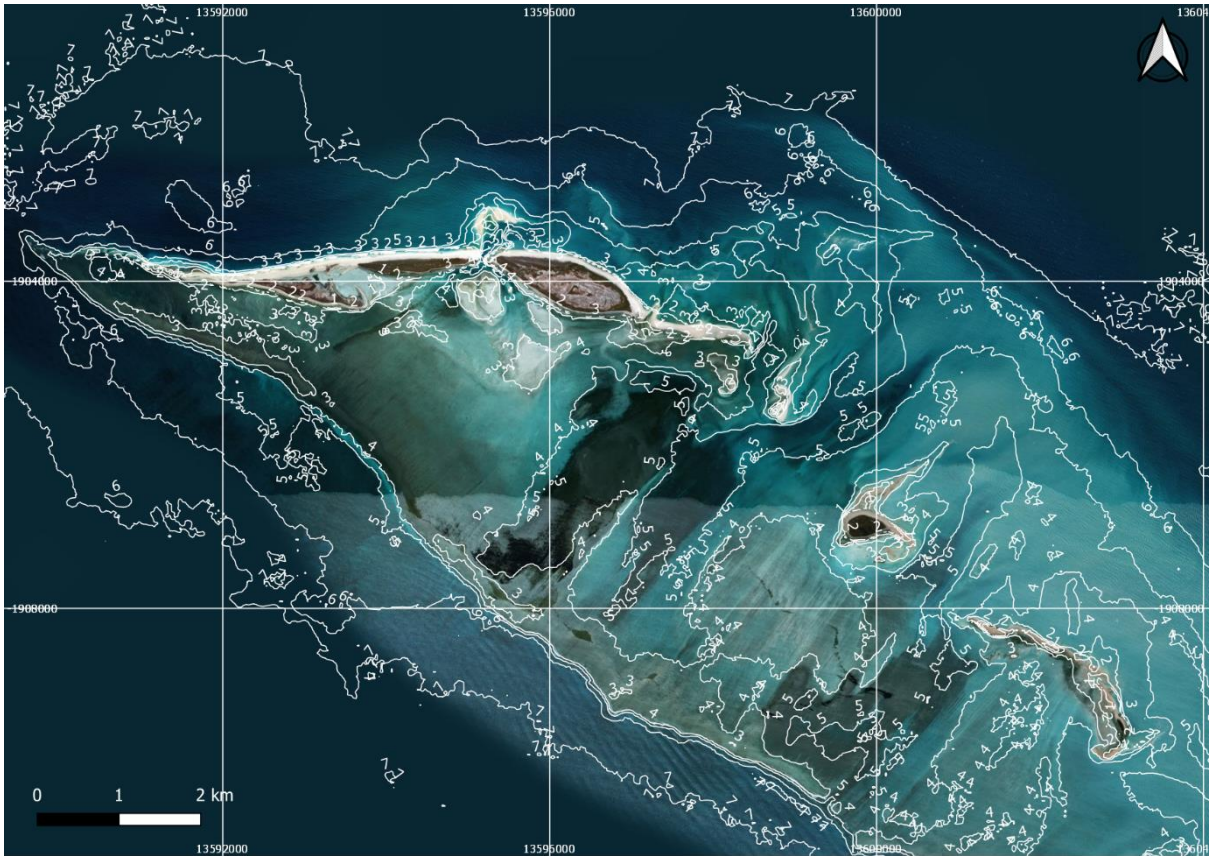
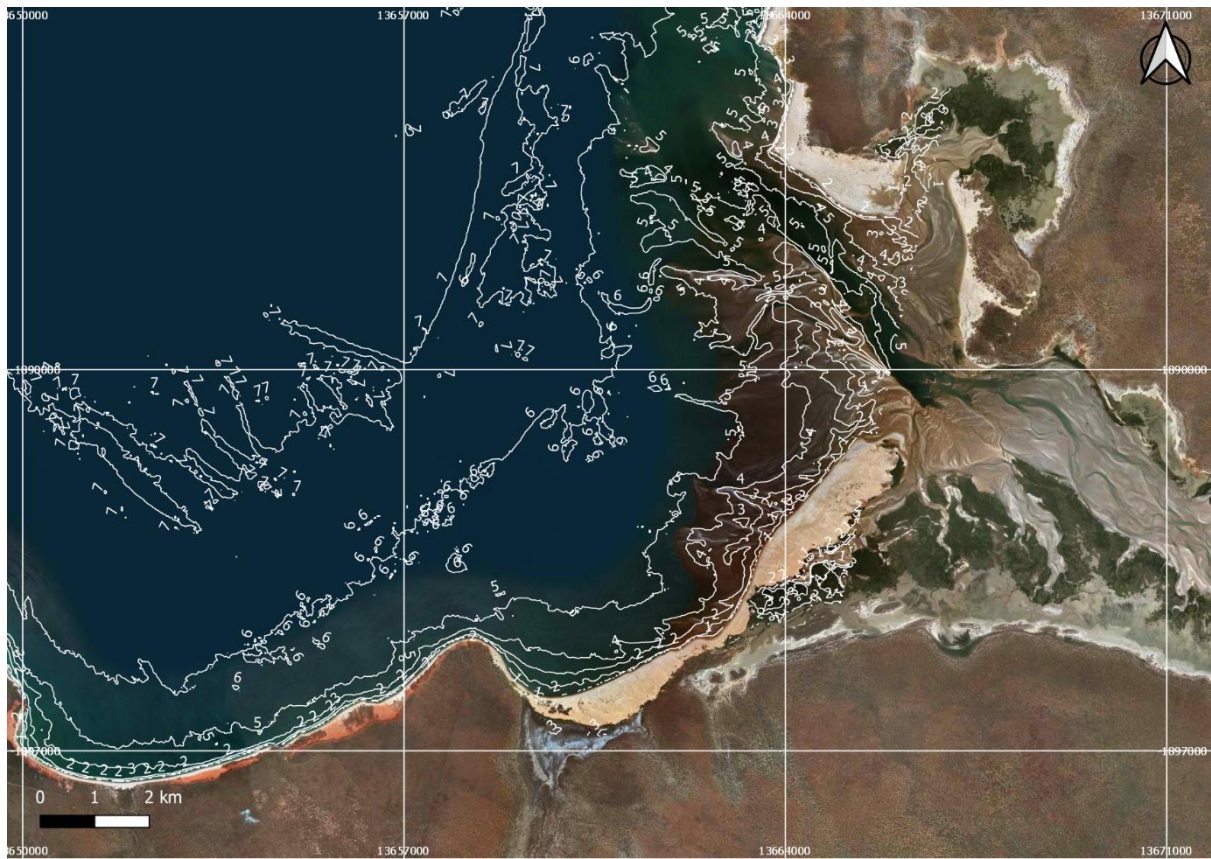


Figure56 : The results of the SDB close to the Lacedepede islands. We can see that the contours describe well the shape of the islands' shore as well as unseen structures at depths reaching to 7 m and beyond. Without further in-situ depth points we cannot assess the accuracy of the deeper contours.



Basemap: © ESRI

Figure57 : The results of the SDB at the north-east of the study area. While the contours follow well the shoreline at this inlet, there are some contours in the deeper water that probably do not match the real depths. They may be the results of unclear water or sediments.

Testing Different Fitting Methods

The fitting method most often used in the SDB literature is a simple linear regression that aims to minimize the residual sum of squares between the observations and the predictions. In SDB terms, it minimizes the sum of squares between the in-situ depth measurements and the log-band ratio of a specific scene. This method is sensitive to outliers in the data since it gives the same weight to every point. In cases where error in the data is expected, other linear regression methods may show better results.

I have tested two other linear regression methods on each of the four study areas with regards to the best scene that was selected during the SDB process (Fig. 58). Since the linear regression of the two study areas calibrated with tidal data had only two points, there was no need to test these methods in those areas as well.

The results of the different methods are summarized in table 3:

Study Area	OLS	Theil-Sen	Huber
Eilat	2.58	2.75	2.66
Dahlak	2.44	2.47	2.48
Bab el-Mandab	4.35	4.49	4.36
Qatar	2.99	3.09	2.99
Mean Error	3.09	3.2	3.12

Table 3: A comparison between different linear regression method in the four study areas. The results are the RMSE of each method regarding the entire dataset of points. The 'ordinary' linear regression (OLS) seems to have the best results overall.

It seems that in these four study areas there was no benefit of applying different linear regression methods as the RMSE does not show a clear preferred method. Furthermore, the 'simple' linear regression method, the OLS, achieved slightly better results overall. We need to consider that these tests were executed on scenes that were selected by the OLS method during the SDB script runs. It is possible that by applying a different regression method during the selection of the scenes, another scene would had been selected with lower RMSE in that specific method.

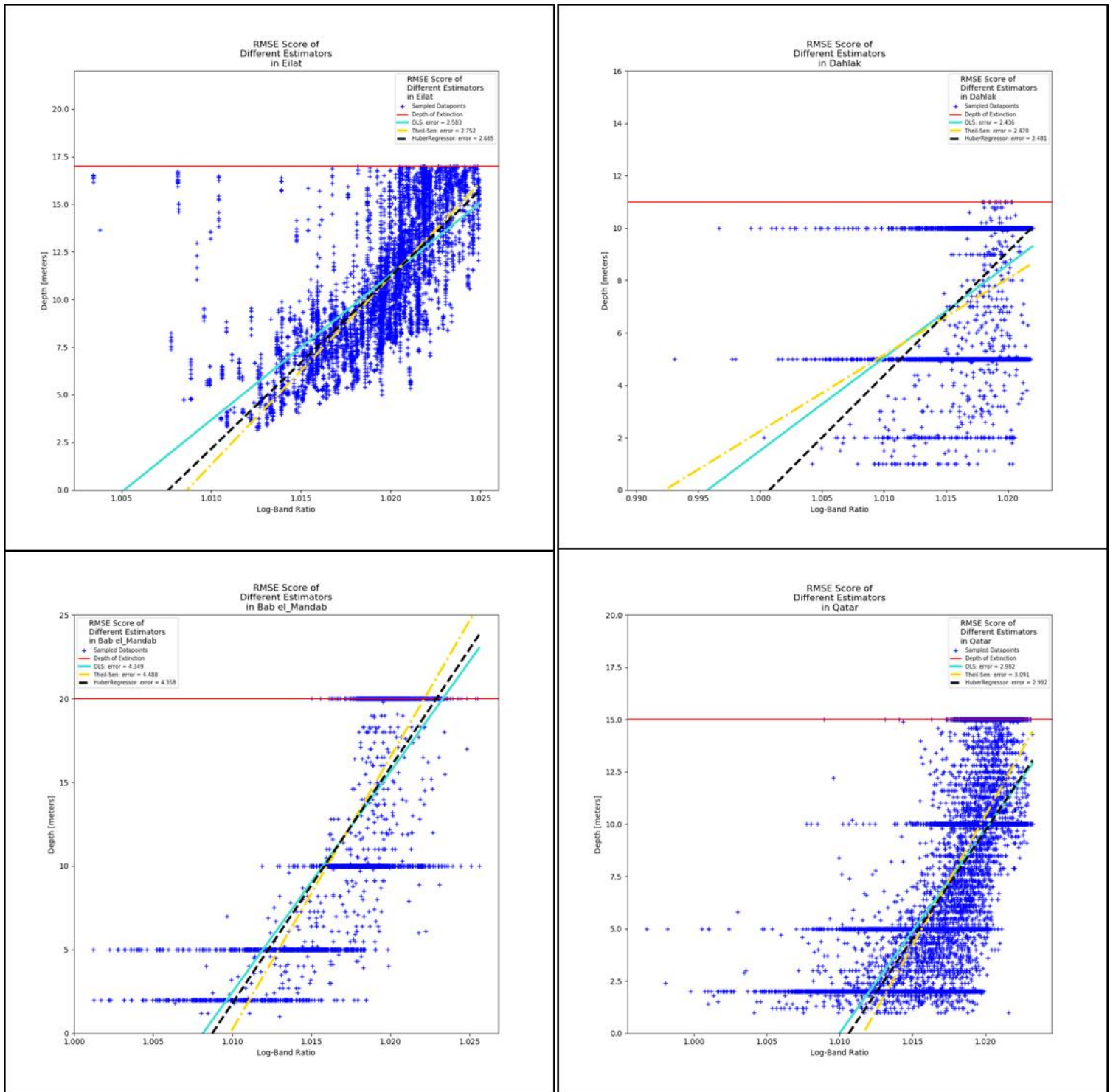


Figure58 : A comparison of the different linear regression methods in the four study areas. The error was estimated in RMSE to better understand the amount of error regarding the depth of extinction.

Future Studies

I believe that the SDB process that I have developed and used in this study may be further improved in future studies, specifically with regarding the following points:

1. While Otsu's method for thresholding had good results in separating the land and the water, there may be better methods for increasing its accuracy. This may influence the semi-wet pixels at the shorelines.
2. Landsat 8 was a good choice for this study. It has a good searchable archive and good spatial and temporal resolution. However, there are currently other publicly available satellites which could improve the accuracy of the SDB. Sentinel 2, for example, has better resolution (10 m per pixels compared to 30 m in Landsat 8) and offers bands in a similar wavelength, thus can be implemented in the SDB process.
3. While the automatic, multithreaded, downloading of the scenes by my script reduced the time consumption of the SDB process, it relies on local internet bandwidth and thus is limited. Future studies should prefer working directly in the cloud resources, without downloading any data. This will have a dramatic improvement on the overall performance.
4. In this study I tested several linear regression methods after selecting the best scene. These methods can be implemented as an integral part of the script. Moreover, recent studies (Cahalane et al., 2017) have used geographic weighted regression (Brunsdon et al., 1998) for the calibration, which could also be integrated into the SDB process.
5. The tidal-based calibration can be further developed by adding more data points in the study areas, comparing different high and low tide events and testing it in areas for which there are in-situ measurements points for the accuracy estimations.
6. The SDB algorithm could be improved by looking for correlation between other wavelengths and the depth. This should be tested with machine learning methods, mainly neural networks, on all the available bands in each scene.

Summary

Satellite derived bathymetry (SDB) had been implemented increasingly in recent years thanks to the raise in computational abilities and the large amounts of accessible imagery data. This tool offers the ability to map the shallow waters of earth in a relatively cheap and fast manner.

In this research I improved an SDB method by developing a scripted, automated process which uses publicly available cloud data and free, open sourced tools, to generate SDB on a large scale. I tested this process on four study areas and the results show a relatively high accuracy by comparing them to in-situ depth measurements.

The ability to rapidly map areas lacking in-situ data was also tested in this study as I developed a calibration method which relies on tidal amplitudes and comparison of differences of shorelines between high and low tide. This method shows promising results and it could be further developed to improve its accuracy.

Bibliography

1. Brunson, C., Fotheringham, S. & Charlton, M. Geographically Weighted Regression. *J. R. Stat. Soc. Ser. D (The Stat.* 47, 431–443 (1998).
2. Caballero, I. & Stumpf, R. P. Retrieval of nearshore bathymetry from Sentinel-2A and 2B satellites in South Florida coastal waters. *Estuar. Coast. Shelf Sci.* 226, 106277 (2019).
3. Cahalane, C., Hanafin, J. & Monteys, X. Improving satellite-derived bathymetry. *Hydro Int.* 21, 16–19 (2017).
4. Chénier, R., Faucher, M. A. & Ahola, R. Satellite-derived bathymetry for improving Canadian Hydrographic Service charts. *ISPRS Int. J. Geo-Information* 7, (2018).
5. da Costa-Luis, C. O. tqdm: A Fast, Extensible Progress Meter for Python and CLI. *J. Open Source Softw.* 4, 1277 (2019).
6. Dang, X., Peng, H., Wang, X. & Zhang, H. The Theil-Sen Estimators in a Multiple Linear Regression Model. Manuscript, (2009).
7. Dekker, A. G. et al. OCEANOGRAPHY: METHODS Intercomparison of shallow water bathymetry, hydro-optics, and benthos mapping techniques in Australian and Caribbean coastal. 396–425 (2011).
8. Department of the Interior, U.S. Geological Survey, LANDSAT 8 (L8) DATA USERS HANDBOOK, LSDS-1574 (2019)
9. Eakins, B.W. and G.F. Sharman. Hypsographic Curve of Earth's Surface from ETOPO1, NOAA National Geophysical Data Center, Boulder, CO, 2012
10. Fischler, M. A. & Bolles, R. C. Random sample consensus: a paradigm for model fitting with applications to image analysis and automated cartography. *Commun. ACM* 24, 381–395 (1981).
11. Fisheries and Oceans Canada, contains information licensed under the Open Government License – Canada. <http://www.dfo-mpo.gc.ca/index-eng.htm>
12. Hall, J. K. & Levenson, S. Compilation of a 100m bathymetric grid for the Arabian Plate; Red Sea, Arabian and Oman Seas and Persian Gulf. Poster presented at the US HYDRO 2017 Conference, The Hydrographic Society of America (THSOA), Galveston, TX, Mar 20-23, 2017. Also, at the GEBCO Seabed 2030 Conference in Busan, ROK, (Nov 2017).

13. Hicks, S. Understanding tides. National Oceanic and Atmospheric Administration (2006).
14. Huber, P. J. Robust Estimation of a Location Parameter. *Ann. Math. Stat.* 35, 73–101 (1964).
15. International Hydrographic Organization (IHO). S-57 Supplement No. 3— Supplementary Information for the Encoding of S-57 Edition 3.1 ENC Data. International Hydrographic Organization: Monaco (2014).
16. International Hydrographic Organization, Intergovernmental Oceanographic Commission, The IHO-IOC GEBCO Cook Book, IHO Publication B-11, Monaco, 429 pp – IOC Manuals and Guides 63, France (Dec. 2015).
17. J. D. Hunter, Matplotlib: A 2D Graphics Environment, *Computing in Science & Engineering*, vol. 9, no. 3, pp. 90-95 (2007).
18. Jégat, V., Pe’eri, S., Freire, R., Klemm, A. & Nyberg, J. Satellite-Derived Bathymetry: Performance and Production. *Canadian Hydrographic Conference*. 1–8 (2016).
19. Jones E, Oliphant E, Peterson P, et al. *SciPy: Open Source Scientific Tools for Python*, (2001).
20. Kabiri, K. Accuracy assessment of near-shore bathymetry information retrieved from Landsat-8 imagery. *Earth Sci. Informatics* 10, 235–245 (2017).
21. Lyzenga, D. R. Passive remote sensing techniques for mapping water depth and bottom features. *Appl. Opt.* 17, 379–383 (1978).
22. Mayer, L. et al. The Nippon Foundation—GEBCO Seabed 2030 Project: The Quest to See the World’s Oceans Completely Mapped by 2030. *Geosciences* 8, 63 (2018).
23. McKinney, Walter G. *Data Structures for Statistical Computing in Python*. (2010).
24. Millman, K. J. & Aivazis, M. Python for scientists and engineers. *Comput. Sci. Eng.* 13, 9–12 (2011).
25. Morel, A., Claustre, H. & Gentili, B. The most oligotrophic subtropical zones of the global ocean: Similarities and differences in terms of chlorophyll and yellow substance. *Biogeosciences* 7, 3139–3151 (2010).
26. Otsu, N. A Threshold Selection Method from Gray-Level Histograms. *IEEE Trans. Syst. Man. Cybern.* 9, 62–66 (1979).

27. Pe'eri, S., Parrish, C., Azuike, C., Alexander, L. & Armstrong, A. Satellite Remote Sensing as a Reconnaissance Tool for Assessing Nautical Chart Adequacy and Completeness. *Mar. Geod.* 37, 293–314 (2014).
28. Pedregosa, F. et al. Scikit-learn: Machine Learning in Python. *Psychol. Sci.* 25, 1682–1690 (2012).
29. Philpot, W. D. Bathymetric mapping with passive multispectral imagery. *Appl. Opt.* 28, 1569 (1989).
30. Stéfan van der Walt, Johannes L. Schönberger, Juan Nunez-Iglesias, François Boulogne, Joshua D. Warner, Neil Yager, Emmanuelle Gouillart, Tony Yu and the scikit-image contributors. scikit-image: Image processing in Python. *PeerJ* 2:e453 (2014)
31. Stumpf, R. P., Holderied, K. & Sinclair, M. Determination of water depth with high-resolution satellite imagery over variable bottom types. *Limnol. Oceanogr.* 48, 547–556 (2003).
32. The Bureau of Meteorology, Australian government.
<http://www.bom.gov.au/index.php>
33. Van Der Walt, S., Colbert, S. C. & Varoquaux, G. The NumPy array: A structure for efficient numerical computation. *Comput. Sci. Eng.* 13, 22–30 (2011).